A Numerical and Analytical Study of Detonation Diffraction

Thesis by

Marco Arienti

In Partial Fulfillment of the Requirements

for the Degree of

Doctor of Philosophy

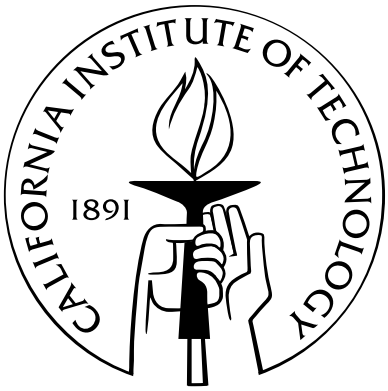

California Institute of Technology

Pasadena, California

2003

(Submitted January 24, 2003)

Acknowledgements

I would first like to thank my advisor, Joseph Shepherd, whose enthusiasm has been a constant source of inspiration in the long years leading to the preparation of this thesis. This work could be completed only thanks to his insight in all aspects of detonation theory, modeling and experiments.

My education at GALCIT has profited from several discussions with Eric Morano and Patrick Hung, who also provided part of the code I used in my computations. I am indebted to Michael Aivazis and Julian Cummings at the Center for Advanced Computing and Research at Caltech for their assistance in cross-platform compilation, as well as for their attempts to train me to a more rigorous programming discipline. By permitting an easy and unrestricted access to the computational resources of the Center, Michael offered the ideal environment for my research. Professor Manish Parashar at Rutgers University provided the framework for parallel simulations with his software package GrACE, and a kind assistance that was very much appreciated. I would also like to thank several other researchers at GALCIT for their useful insights in fluid mechanics in general and physics of detonations in particular – Eric Schultz, Joanna Austin, Eric Winterberger, Demos Kivotides, Ravi Samtaney and Cristopher Eckett. Suzy Dake's secretarial talents were appreciated as were the proofreading skills of Melinda Kirk. I also thank Professors Hans Hornung, Dan Meiron, Tim Colonius, and Ron Cohen, for taking the time to read my thesis and for serving on my examining committee.

Finally, and most importantly, I am grateful to my wife, Valeria, for her years of moral support and patience.

The work was supported by the Caltech ASAP Center for Simulation of Dynamic

Response of Materials, under the DOE Accelerated Strategic Computing Initiative.

Abstract

An investigation of detonation diffraction through an abrupt area change has been carried out via two-dimensional, parallel simulations. The existence of critical conditions for successful diffraction is closely related to the occurrence of localized re-initiation mechanisms, and is relevant to propulsion and safety concepts concerning detonation transmission. Our analysis is specialized to a reactive mixture with perfect gas equation of state and a single-step reaction in the Arrhenius form. The concept of shock decoupling from the reaction zone is the simplest idea used to explain the behavior of a diffracting detonation front. Lagrangian particles are injected into the flow in order to identify the dominant terms in the equation that describes the temperature rate of change of a fluid element, expressed in a shock-based reference system. Conveniently simplified, this equation provides an insight into the competition between the energy release rate and the expansion rate behind the diffracting front. We also examine the mechanism of spontaneous generation of transverse waves along the front. This mechanism is related to the sensitivity of the reaction rate to temperature, and it is investigated in the form of a parametric study for the activation energy. We study in detail three highly resolved cases of detonation diffraction that illustrate different types of behavior, super-, sub-, and near-critical diffraction. We review the applicability of existing shock dynamics models to the corner-turning problem. Numerical results from the parametric study are compared with predictions from these theories in the attempt to find a formula for shock decay in a quenching detonation. This estimate is then used in the simplified temperature rate of change equation to provide a relation between critical channel width and activation energy. We conclude this study by examining the spontaneous formation of transverse waves along the wavefront of

a successfully transmitted detonation. The problem is simplified to a planar CJ detonation moving in a channel over a small obstacle to investigate how acoustic waves propagate within the reaction zone. Depending on the reaction kinetics, we show that such waves may be amplified due to feedback between the chemical reaction and fluid motion. The amplification can lead to shock steepening and formation of transverse detonation waves.

Contents

List of Figures

List of Tables

Nomenclature

		SI Units[†]
Roman characters		
A	area function	
B	wave velocity in the surface kinematics wave equation	m/s
c	frozen sound speed	m/s
C_p	mixture specific heat at constant pressure	J/kg·K
C_v	mixture specific heat at constant volume	J/kg·K
D	detonation velocity	m/s
D_a	detonation velocity along the channel axis of symmetry	m/s
$\dot{D}_b$	initial blast decay rate	m/s^2
D_n	normal detonation velocity	m/s
D_w	detonation velocity along the corner wall	m/s
E_a	activation energy in Arrhenius reaction rate	J
e	specific internal energy	J/kg
E_t	total energy per unit volume	J/m^3
f	detonation overdrive	

[†]Dimensional variables are capped by ˜ in Chapter 3.

$\boldsymbol{F}_x$	convective flux vector in x direction	(various)
$\boldsymbol{F}_y$	convective flux vector in y direction	(various)
H	channel half-width	m
h	number of skipped grid point in the evaluation of curvature	
K	twice the amplification factor in one-dimensional wave equation	1/s
k	pre-exponential factor in model reaction rate	(various)
l	direction cosine of wave normal with respect to x coordinate	
M	leading shock strength	
m	characteristic angle in chapter 5	rad
m	direction cosine of wave normal with respect to y coordinate	
M_s	local flow Mach number with respect to the shock front	
n	exponent in Whitham's area function	
$N_{1/2}$	number of grid points per half-reaction zone length	
n_r	order of reaction	
P_M	Peak value of pressure amplitude	Pa
P	pressure	Pa
Q	heat of reaction	J/kg
r	blast radius	m
r_b	initial blast radius	m
R_g	specific gas constant of mixture	J/kg·K
$\mathcal{R}$	universal gas constant	J/mol·K

s	amplitude of acoustic disturbance	
$\boldsymbol{S}$	reaction source term vector	(various)
T_a	activation temperature of reaction	K
t_b	initial time in blast model	s
t	time	s
u	flow velocity in the laboratory frame	m/s
u_η	flow velocity in normal direction	m/s
u_ξ	flow velocity in transverse direction	m/s
u_x	flow velocity in x direction	m/s
u_y	flow velocity in y direction	m/s
$\boldsymbol{W}$	conservative solution vector	(various)
w	flow velocity in the shock frame	m/s
W	mean molar mass of mixture	kg/mol
W_k	molar mass of species k	kg/mol
w_η	flow velocity in normal direction in intrinsic coordinates	m/s
w_ξ	flow velocity in transverse direction in intrinsic coordinates	m/s
x	laboratory Cartesian coordinate	m
y	laboratory Cartesian coordinate	m
x_0	x coordinate of intrinsic system reference point	m
x_b	obstacle position	m
y_0	y coordinate of intrinsic system reference point	m

$\boldsymbol{y}$	vector of species mass fractions	
y_K	mass fraction of species K	
Z	reaction progress variable in one-step reaction	

Greek characters

α	angle of the disturbance trace with the undiffracted shock normal	rad
Δ	induction length	m
$\Delta_{1/2}$	ZND half-reaction length for CJ detonation	m
ϵ	height and width of obstacle	m
γ	ratio of mixture specific heats	
η	shock based (intrinsic) coordinates	m
κ	local front curvature	1/m
κ_a	front curvature along the axis of symmetry	1/m
κ_d	front curvature at the reflection of the first C^+ characteristic	1/m
κ_b	initial blast curvature	1/m
Λ	wavelength of acoustic disturbances	m
λ	detonation cell width	m
ν	coordinate in the normal direction with respect to the acoustic wavefront	m
ω	sonic parameter	$\mathrm{m}^2/\mathrm{s}^2$
ϕ	front normal angle with respect to the axis of reference	rad
φ	level set function	m
ρ	density	kg/m^3

$\dot{\sigma}$	total thermicity	1/s
σ_K	thermicity coefficient of species K	
θ	ray angle with respect to x	
θ_{CJ}	activation energy normalized by the CJ post-shock temperature	
ξ	shock based (intrinsic) coordinates	m
Ω_K	production rate of species K	1/s
ζ	activation energy normalized by $T_\parallel$	

Subscripts

K	species index
$\parallel$	plane of parallel propagation with respect to the detonation front

Accents

$\tilde{}$	dimensional quantity [see page 25]

Chapter 1

Introduction

1.1 Detonation wave structure

Detonations are supersonic combustion waves with a strong leading shock front. The shock wave ignites the reactive material and the exothermic stage of the reactions creates volume expansion that pushes the shock into fresh reactants.

Experiments in reactive mixtures reveal that detonation fronts tend to develop complicated three-dimensional time-dependent structures with interior transverse shock waves (see, for instance, Fickett and Davis 1979). A self-sustaining cellular structure, driven by chemical reactions, is often observed. The cell boundaries are unsteady, decaying transverse waves which propagate at approximately acoustic velocity. They are periodically restored by collision with waves moving in the opposite direction. The variations of pressure and velocity in this structure are sufficient to incise diamond-shaped patterns on sooted plates, see Fig. 1.1 from Kaneshige (1999).

To study this intricate flow field, the simplest, physically relevant mathematical model is provided by the reactive Euler equations of gasdynamics, expressing conservation of mass, momentum and energy for an inviscid flow. An additional set of equations describes the rate of change of the chemical species as observed by material particles in the flow. Transport effects and dissipative processes are neglected in this model.

To gain insight into the reaction zone structure, a detonation can be further idealized as a one-dimensional wave where a shock discontinuity, with no chemical

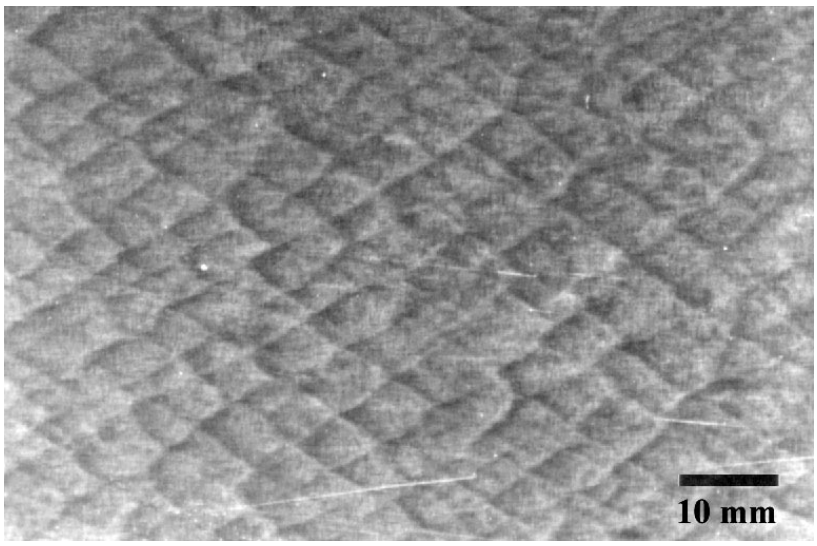

Figure 1.1: Sooted aluminum sheet. From Kaneshige (1999).

processes, is followed by a region with a finite rate of reaction. Under these conditions, the reactive Euler equations admit a steady solution in the coordinate system attached to the shock. This solution (the Zel'dovich-von Neumann-Doering, or ZND, wave) propagates at speed D which is a function of the boundary conditions at the end of the reaction zone.

Figure 1.2 shows a representative pressure and temperature profile for a ZND wave computed by Schultz (2000) with a program developed by Shepherd (1986). The program uses the Chemkin II chemical kinetics package and integrates the equations of mass, momentum, energy and species conservation through the reaction zone. (Kee et al. 1989). The species production rates of a stoichiometric C_3H_8–O_2 mixture at standard conditions are calculated with the Konnov (1998) detailed reaction mechanism.

In the diagram, pressure and temperature first rise discontinuously to the post-shock (von Neumann) state, and then encounter a region where the thermodynamic state is almost constant. In this induction zone, free radicals (such as OH) are formed with zero or negative energy release until conditions for the exothermic recombinations are reached. The induction length Δ depends on the post-shock conditions and the details of the chemical kinetics. The recombinations that follow are characterized

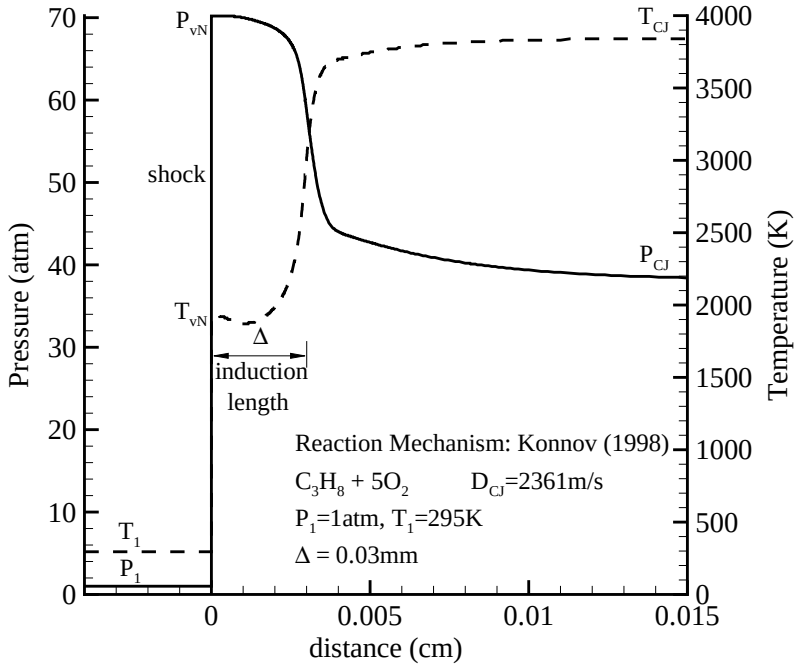

Figure 1.2: Temperature and pressure profile for a ZND wave as a function of the distance behind the shock.

by a rapid rise in temperature, a decrease in pressure, and the formation of the major products of reaction (see Figs 1.2 and 1.3). In this example profile, the sonic parameter $c^2 - (D-u)^2$ reaches a peak value at a distance Δ from the shock and then decreases (Fig. 1.4).

In a Chapman-Jouguet (CJ) wave, the recombination region ultimately passes through a sonic point where the local sound speed equals the particle speed in the reference frame of the shock. The corresponding speed of propagation, D_{CJ}, is the minimum speed allowed based on thermodynamic arguments (Fickett and Davis 1979). Overdriven detonations ($D > D_{CJ}$) are also possible when the particle speed $u > u_{CJ}$ at the end of the reaction zone.

In the next section, we examine how rarefaction waves can interact with the detonation structure and affect the coupling of the leading shock with the reaction zone.

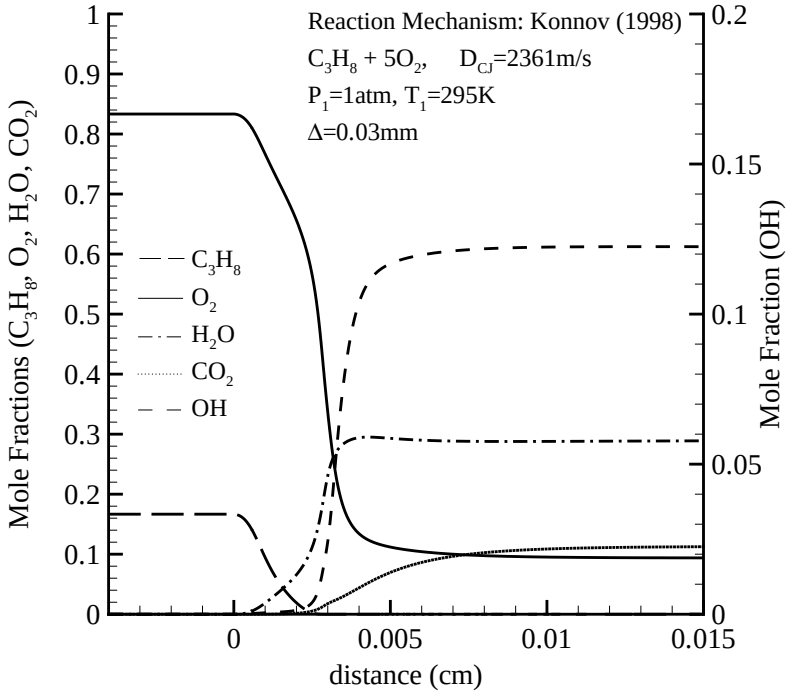

Figure 1.3: Mole fraction profile for a ZND wave.

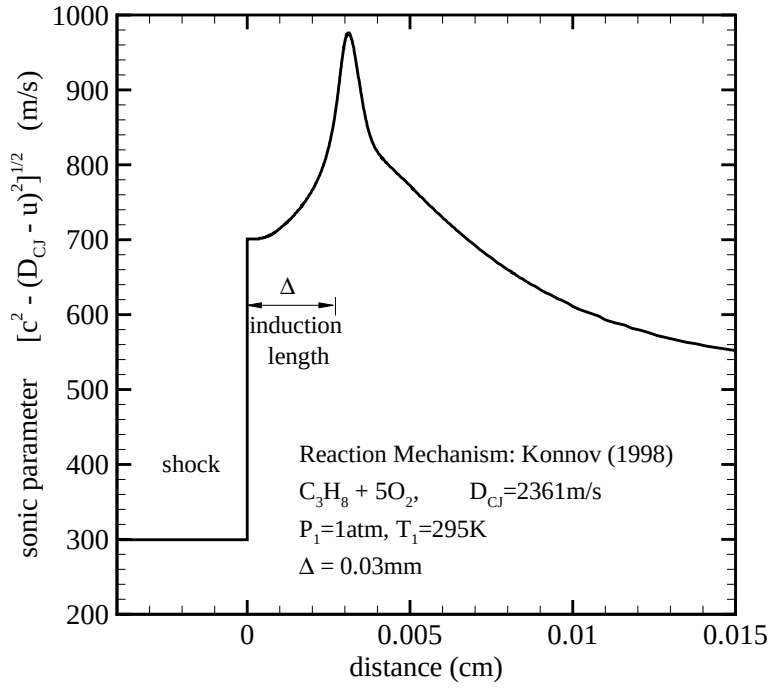

Figure 1.4: Sonic parameter for a ZND wave.

1.2 Detonation diffraction

Detonations diffracting from a planar to a cylindrical (or spherical) geometry through an abrupt area change experience expansion waves that propagate into the partially burnt reactants behind the wavefront.

One of the key features of the diffraction process is the propagation of the signal generated by the expansion waves emanating at the corner. The head of the disturbance intersects the undisturbed detonation, and the propagation speed v of this point can be evaluated with the help of a suitable extension of Skews' geometric construction for non-reacting diffracting shocks (Skews 1967). In Fig. 1.5, we see that the disturbance is propagating at the local sound speed c while being convected downstream at a speed u. The angle α between the disturbance trajectory and the normal of the undiffracted shock, at speed D, can be found with the formula

$$\tan\alpha = \frac{v}{D} = \frac{\sqrt{c^2 - (D-u)^2}}{D}.$$

In the non-reactive cases, the values u and c are determined from the undisturbed post-shock state. In the reactive case, the fact that a finite transverse signal speed is observed in corner-turning experiments with CJ detonations (for instance, Schultz 2000) indicates that these acoustic disturbances must propagate in the reaction zone, between the sonic plane (where $D_{CJ} = u_{CJ} + c_{CJ}$ by definition) and the leading shock.

The sensitivity of chemical reactions to post-shock conditions is the second key feature in detonation diffraction. Typical reaction rates are of the Arrhenius form. For a single-step reaction model of order n_r, this is

$$\Omega = k\,\rho^{n_r-1}\,(1-Z)\,\mathrm{e}^{-T_a/T},$$

where Z monitors the reaction progress (from 0 to 1), n_r is the reaction order, Ω is the reaction rate, T and ρ are the temperature and density of the flow field, and k is

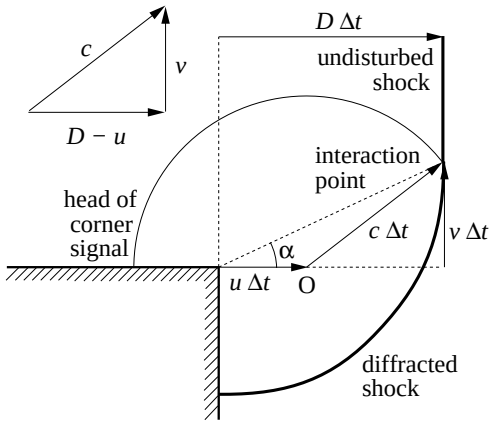

Figure 1.5: Schematic of a diffracting shock (Skews' construction).

a proportionality parameter setting the length scale of energy release. The sensitivity of the chemical kinetics is expressed in the nonlinear term by the parameter T_a, the activation temperature of the reaction.

At the shock, $Z = 0$ and T and ρ depend only on the undisturbed flow ahead, at state 0, and on the shock strength, $M = D/c_0$. For instance, in the limit of $M^2 \gg 1$, a shock in a perfect gas with specific heat ratio γ generates a jump in temperature and density

$$\frac{T_s}{T_0} = \frac{2\gamma\,(\gamma-1)}{(\gamma+1)^2}\,M^2 \qquad\qquad \frac{\rho_s}{\rho_0} = \frac{\gamma+1}{\gamma-1}.$$

Since the shock is weakened by the interaction with expansion waves from the corner, T_s can be significantly smaller along the diffracting front than in a ZND profile, and the reaction process can be quenched or substantially delayed. If the reaction does not take place, or else happens far behind the shock front, then the reduced amount of energy released into the flow results in a further decay of the detonation speed. As the shock strength diminishes, incoming reactants are less compressed, and this in turn increases the ignition delay. Depending on the sensitivity of the reactions to temperature and density changes and the strength of the rarefaction, the detonation will eventually either be re-established, or cease to propagate.

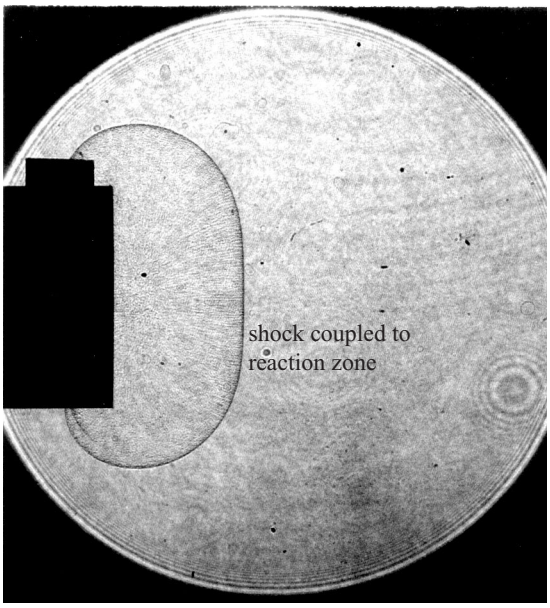

Figure 1.6: Laser shadowgraph of super-critical diffraction of 100 kPa $C_2H_2 + 1/2\,O_2$. From Schultz (2000).

1.2.1 Experimental observations

Whether a diffracting detonation will propagate successfully (super-critical diffraction, Fig. 1.6) or not (sub-critical diffraction, Fig. 1.7), is the result of several factors, namely, the composition of the reactive mixture, the thermodynamic state of the undisturbed reactants, the degree of detonation overdrive, and the geometric setting of the experiment. Of particular interest is finding the critical conditions that control the transition from super-critical to sub-critical, conditions identifying a near-critical state (Fig. 1.8). With all other conditions held constant, the tube diameter determines whether the diffraction is sub-critical or super-critical. The detonation fails for a tube diameter smaller than a critical value (Zel'dovich et al. 1956). There is an empirical correlation between critical diameter and detonation cell width, λ, with a proportionality factor varying between 10 and 30. This is discussed in Mitrofanov and Soloukhin 1965; Knystautas et al. 1982; Moen et al. 1982; Shepherd et al. 1986; Desbordes 1988. The survey by Guirao et al. (1987) for hydrogen-air mixtures indicates that detonation is re-established if the tube diameter is greater than $13\,\lambda$. For rectangular orifices with large aspect ratio, the detonation is re-established if

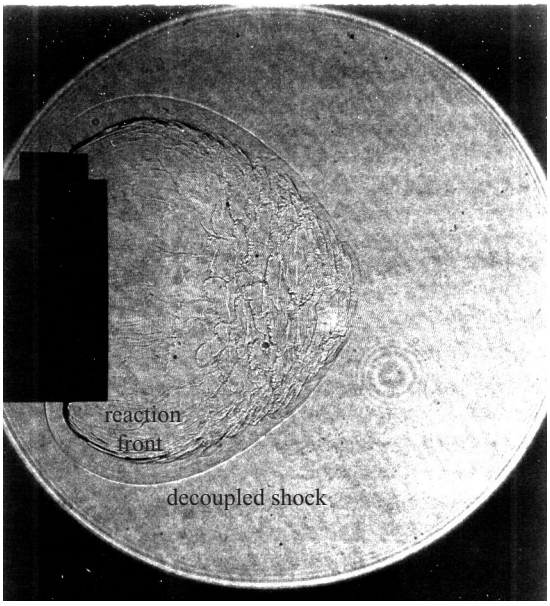

Figure 1.7: Laser shadowgraph of sub-critical diffraction of 70 kPa $H_2 + 1/2\,O_2$. From Schultz (2000).

the smallest side of the orifice is larger than $3\,\lambda$. A recent review of the available detonation diffraction literature can be found in Schultz (2000).

Despite the large amount of experimental data, a quantitative theory to predict the critical tube diameter is still lacking. Edwards et al. (1979) identify the capability to form new transverse wave collisions as the distinguishing feature of a successful diffraction. They suggest that a minimum number of transverse waves across the channel are needed to ensure that enough collisions will take place at the centerline, so that a central hot region survives to re-initiate the detonation. Two distinct modes of re-initiation are identified by Murray and Lee (1983): "spontaneous" in the bulk of the reactive mixture; and "by reflection," at the confining walls. The spontaneous formation of transverse waves is still not completely explained. Lee (1996) suggests that localized explosion centers, or "detonation bubbles," exist for highly temperature-sensitive mixtures, whereas the abrupt generation of transverse reaction fronts is the preferred re-ignition mechanism in less sensitive mixtures.

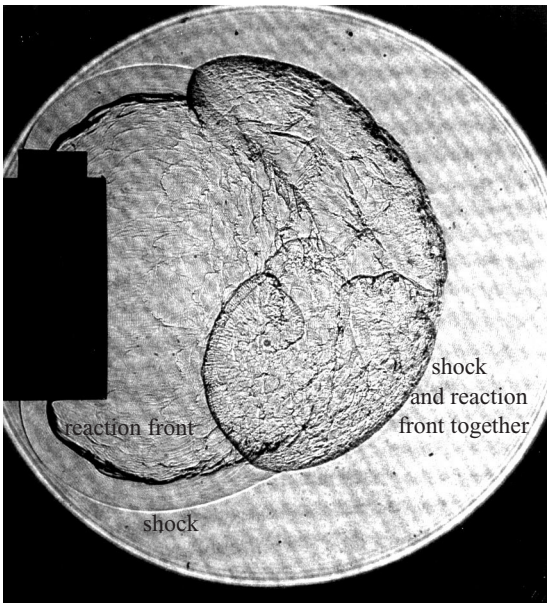

Figure 1.8: Laser shadowgraph of near-critical diffraction 100 kPa $H_2 + 1/2\,O_2$. From Schultz (2000).

1.2.2 Direct numerical simulations

Jones et al. (1990, 1991, 1995) and Oran et al. (1992, 1993) performed an extensive series of numerical simulations to reproduce, in two dimensions, the diffracting patterns in detonation transmission experiments by Liu et al. (1987, 1988). In these experiments, diffraction takes place at the interface between an upper and lower reactive layer. Simulations were based on solutions of time-dependent Euler equations via an explicit nonlinear finite difference technique (Flux-Corrected Transport, or FCT) applied on a uniform grid. The reactive mixture H_2–O_2–Ar (ratio 1:2:7, at atmospheric pressure) was implemented as a two-step mechanism, with a thermally neutral induction period followed by exothermic recombination. Jones et al. (1996, 2000) focused on the role played by detonation cellular structure in spontaneous re-ignition mechanisms. Reproducing spontaneous re-ignition via direct numerical simulations requires sufficient grid resolution to faithfully represent the dynamics of transverse waves. See Sharpe (2001) for a description of the effects of low grid refinement on detonation cellular structure simulations. Jones et al. perturbed an initially planar detonation to form detonation cells (approximately 70 grid points wide) in the upper explosive

layer. These cells weakened as soon as they expanded into the lower layer, while new transverse waves formed spontaneously along the shock front, moved toward the rarefaction zone, and ignited unburnt shocked reactants. If an insufficient number of detonation cells (3 or less) was initially contained in the upper layer, the detonation did not propagate into the lower layer. Li and Kailasanath (2000) observed a successful detonation transmission from a smaller to a larger channel in a stoichiometric ethylene-oxygen mixture when 8 detonation cells were present in the smaller channel. The transmission was unsuccessful in a stoichiometric ethylene-air mixture with only 4 cells.

Pantow et al. (1996) used a two-step MacCormack scheme with FCT to study detonation diffraction of H_2–O_2 mixtures diluted by different amounts of argon or nitrogen. The chemical kinetics were implemented as a two-step parameter model and computations were performed on a time-dependent adaptive grid (no data on grid resolution are reported, but we estimate that at least 45 grid points per detonation cell width were used). As well as illustrating re-ignition after Mach reflection at the confining walls, these simulations show newly formed transverse waves in regions where the detonation front begins to fail.

Simulations with single-step Arrhenius kinetics by Williams et al. (1996) indicate that the generation and interaction of transverse waves are even more intricate in three dimensions. While the grid resolution is quite coarse (only 8 grid points in the reference half-reaction length), Williams' results show the existence of perpendicular modes which generate vorticity fields more complex than in two dimensions. Vorticity seems to provide a strong coupling mechanism between the perpendicular modes, and is possibly a trigger mechanism for the production of new transverse waves.

1.3 Thesis outline

In the problem we investigate, detonation diffraction takes place around a sharp corner, interior angle of 90°. An instance of this situation is encountered when a detonation tube or channel opens into a larger volume. The problem has a plane of

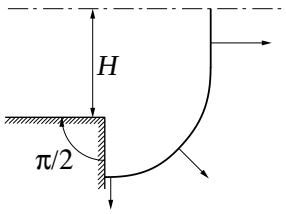

Figure 1.9: Detonation diffraction around a corner. $-\cdot-\cdot$ denotes the plane of symmetry of the channel, H the channel half-width.

symmetry, and in Fig. 1.9 we show only the lower half-space of the domain. We will refer to the intersection of the plane of symmetry with the x-y plane as the axis of symmetry of the channel. If we assume an unbounded volume, then the only geometric parameter of the problem is the exit diameter of the tube. In two dimensions, the reference length is the channel half-width, H. Dimensional analysis for the single-step reaction model in the Arrhenius form leads to the following dependence for the critical channel half-width,

$$\frac{H_c}{\Delta_{1/2}} = g\left(\frac{Q}{R_g T_0}, \gamma_p, \gamma_r, f, \frac{T_a}{T_0}, n\right), \tag{1.1}$$

where Q is the heat of reaction, γ_r and γ_p are the reactant and product specific heat ratios, and $f = D/D_{CJ}$ is the overdrive of the detonation in the channel. The reaction characteristic length $\Delta_{1/2}$ is defined as the distance, in the reference CJ wave, between the shock ($Z = 0$) and the point where $Z = 1/2$. Our study is further specialized by setting $f = 1$, $\gamma_p = \gamma_r$, and $n_r = 2$.

The concept of shock decoupling from the reaction zone is the simplest idea used to explain the behavior of a diffracting detonation front. Chapter 2 is devoted to the extension to an arbitrary wavefront of the equation framework used in the study of direct initiation of spherically symmetric detonations (Eckett et al. 2000). The numerical implementation of the equations of fluid motion, and the algorithms used for flow diagnostics, are described in Chapter 3.

In Chapter 4, we examine three cases of detonation diffraction that illustrate different types of behavior, super-, sub-, and near-critical diffraction. Lagrangian particles are injected into the flow in order to identify the dominant terms in the equation that

describes the temperature rate of change of a fluid element. Conveniently simplified, this equation provides the starting point for a critical diffraction model. We examine the mechanism of spontaneous generation of transverse waves due to reflection of the unsteady rarefaction front. This mechanism is related to the sensitivity of the reaction rate to temperature, and it is investigated in the form of a parametric study for the activation energy.

In Chapter 5, we review the applicability of existing shock dynamics models to the corner-turning problem. Numerical results from the parametric study are compared with predictions from these theories. The objective is to find a formula for shock decay at the centerline when the detonation front is close to local failure. This formula is then used in the simplified temperature rate of change equation to give a relation between critical diameter and activation energy.

Chapter 6 is devoted to the study of a result that emerged from the computation of fully coupled diffracting detonations: the spontaneous formation of transverse waves along the wavefront. We consider planar CJ detonations, with $n_r = 1$ and $n_r = 2$, moving in a channel over a small obstacle, to study how acoustic waves propagate within the reaction zone. Depending on the reaction kinetics, we show that such waves may be amplified due to feedback between the chemical reaction and fluid motion (Strehlow and Fernandes 1965). The amplification can lead to shock steepening and formation of transverse detonation waves.

The last chapter contains an overview of our conclusions.

Chapter 2

Governing equations

2.1 Reactive Euler equations

Ignoring viscosity, heat transfer, diffusion, radiation and body forces, the governing equations for a compressible reacting flow are the reactive Euler equations (see, for instance, Fickett and Davis 1979). In a fixed Cartesian reference frame, the two-dimensional, reactive Euler equations are given by

$$\frac{\mathrm{D}\rho}{\mathrm{D}t} + \rho\frac{\partial u_x}{\partial x} + \rho\frac{\partial u_y}{\partial y} = 0, \tag{2.1a}$$

$$\frac{\mathrm{D}u_x}{\mathrm{D}t} + \frac{1}{\rho}\frac{\partial P}{\partial x} = 0, \tag{2.1b}$$

$$\frac{\mathrm{D}u_y}{\mathrm{D}t} + \frac{1}{\rho}\frac{\partial P}{\partial y} = 0, \tag{2.1c}$$

$$\frac{\mathrm{D}e}{\mathrm{D}t} - \frac{P}{\rho^2}\frac{\mathrm{D}\rho}{\mathrm{D}t} = 0, \tag{2.1d}$$

$$\frac{\mathrm{D}y_K}{\mathrm{D}t} = \Omega_K, \tag{2.1e}$$

where u_x, u_y, ρ, P and e are the velocity in the x and y coordinate directions, density, pressure, and specific internal energy. The variable t is the time, y_K is the mass fraction of species K, and Ω_K is the production rate of species K (given by a kinetic rate law). The index K varies between 1 and N, the total number of species. The operator $\mathrm{D}/\mathrm{D}t$ denotes the time derivative along a particle path, i.e., the Lagrangian

derivative of a variable

$$\frac{\mathrm{D}}{\mathrm{D}t} = \frac{\partial}{\partial t} + u_x \frac{\partial}{\partial x} + u_y \frac{\partial}{\partial y}. \tag{2.2}$$

If we take the e to be a function of P, ρ, and the mass fraction array $\mathbf{y} = \{y_K,\ K = 1, \ldots, N\}$, then

$$\frac{\mathrm{D}e}{\mathrm{D}t} = \left.\frac{\partial e}{\partial P}\right|_{\rho,\,\mathbf{y}} \frac{\mathrm{D}P}{\mathrm{D}t} + \left.\frac{\partial e}{\partial v}\right|_{P,\,\mathbf{y}} \frac{\mathrm{D}v}{\mathrm{D}t} + \sum_K \left.\frac{\partial e}{\partial y_K}\right|_{P,\,\rho,\,y_{J\neq K}} \frac{\mathrm{D}y_K}{\mathrm{D}t}. \tag{2.3}$$

From this expression and Equation (2.1d), we obtain the adiabatic change equation,

$$\frac{\mathrm{D}P}{\mathrm{D}t} = c^2 \frac{\mathrm{D}\rho}{\mathrm{D}t} + \rho c^2 \sum_K \sigma_K \Omega_K. \tag{2.4}$$

In Equation (2.4), c is the constant composition, or frozen, sound speed,

$$c^2 = \frac{P + \left.\dfrac{\partial e}{\partial v}\right|_{P,\,\mathbf{y}}}{\rho^2 \left.\dfrac{\partial e}{\partial P}\right|_{\rho,\,\mathbf{y}}}, \tag{2.5}$$

and σ_K is the thermicity coefficient of species K,

$$\sigma_K = \frac{1}{\rho c^2} \left.\frac{\partial P}{\partial y_K}\right|_{e,\,\rho,\,y_{J\neq K}} = -\frac{1}{\rho c^2} \frac{\left.\dfrac{\partial e}{\partial y_K}\right|_{P,\,\rho,\,y_{J\neq K}}}{\left.\dfrac{\partial e}{\partial P}\right|_{\rho,\,\mathbf{y}}}. \tag{2.6}$$

In this work, we will find it useful to replace the energy equation (2.1d) with the adiabatic change equation. The sum of the thermicity coefficients σ_K in Equation (2.4) expresses the total pressure change due to chemical reaction at constant volume. This last term is called the thermicity product $\dot{\sigma}$,

$$\dot{\sigma} = \sum_K \sigma_K \Omega_K. \tag{2.7}$$

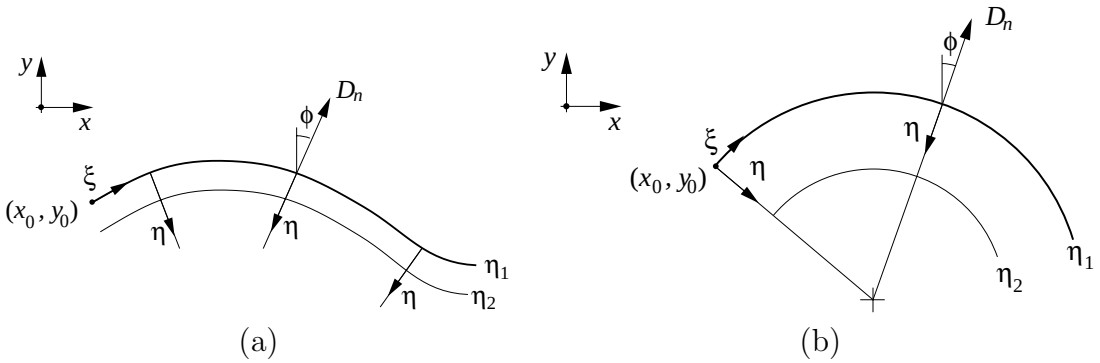

Figure 2.1: Intrinsic coordinates ξ and η for an arbitrary front, (a), and specialized to a cylindrical front, *(b)*.

2.2 Reactive Euler equations in intrinsic coordinates

The analysis of the reactive Euler equations can be carried out by using intrinsic, shock-based coordinates as independent variables. While more cumbersome than the Cartesian description of the previous section, this approach allows for a direct comparison with the system of equations that can be derived for cylindrical symmetry. In this way, the effect of shock front curvature can be more easily examined. As we will show, the formulation in intrinsic coordinates simplifies noticeably along an axis of symmetry of the flow. In this case, only one additional term, due to the transverse flow divergence behind the leading shock, is formed in comparison to the cylindrical case (Eckett et al. 2000).

In intrinsic coordinates (Fig. 2.1), the variable ξ measures the arc length of the leading shock from a reference point (x_0, y_0). Along the shock, the second coordinate η is constant and is equal to zero. Lines of constant η are the loci of points with the same distance from the shock. The angle ϕ, formed by the normal to the front with respect to a reference axis, is a dependent variable, $\phi\,(\xi, t)$. The two-dimensional curvature of the front, κ, is by definition $\kappa = (\partial\phi/\partial\xi)_{\eta,\,t}$. D_n is the detonation velocity normal to the front.

As an example of an intrinsic coordinate system, Fig. 2.1 (b) shows the particular case of a cylindrical front with radius $R\,(t)$. In this simple situation, the relation between ξ and η and the cylindrical coordinates (r and ϕ) is given by $\xi = \phi\, R$ and

$\eta = R - r$, and we find the trivial result $\kappa = 1/R$.

Conservation of mass, momentum and total energy can be written in intrinsic coordinates as (Bdzil and Aslam 2000),

$$\mathcal{L}(\rho) + [(D_n - u_\eta)\,\rho]_{,\eta} + \rho\,\frac{u_\eta\kappa + u_{\xi,\xi}}{1-\eta\,\kappa} = 0, \tag{2.8a}$$

$$\mathcal{L}(u_\eta) + (D_n - u_\eta)\,u_{\eta,\eta} = \frac{P_{,\eta}}{\rho} - \frac{u_\xi\,(D_{n,\xi} - u_\xi\kappa)}{1-\eta\,\kappa}, \tag{2.8b}$$

$$\mathcal{L}(u_\xi) + (D_n - u_\eta)\,u_{\xi,\eta} = -\frac{P_{,\xi} + \rho u_\eta\,(u_\xi\kappa - D_{n,\xi})}{\rho\,(1-\eta\,\kappa)}, \tag{2.8c}$$

$$\mathcal{L}(e) + (D_n - u_\eta)\,e_{,\eta} = \frac{P}{\rho^2}[\mathcal{L}(\rho) + (D_n - u_\eta)\,\rho_\eta], \tag{2.8d}$$

where we use the notation $,\xi$ and $,\eta$ to indicate a partial derivative with respect to ξ and η, in this order. The operator

$$\mathcal{L} = \left.\frac{\partial}{\partial t}\right|_{\xi,\,\eta} + \left(B + \frac{u_\xi - \eta D_{n,\xi}}{1-\eta\,\kappa}\right)\left.\frac{\partial}{\partial \xi}\right|_{t,\,\eta}, \tag{2.9}$$

and u_η, u_ξ are the particle velocity components in the shock normal and transverse direction. Where intrinsic coordinates can be used, the set (2.8) is completely equivalent to the set (2.1)(a) to (d). Note, however, that the partial time derivatives in the Cartesian and intrinsic system differ,

$$\left.\frac{\partial}{\partial t}\right|_{\xi,\eta} \neq \left.\frac{\partial}{\partial t}\right|_{x,y}, \tag{2.10}$$

since the intrinsic reference system is time varying.

In Equation (2.9), B is the wave velocity in the surface kinematics equation (Bdzil and Stewart 1989)

$$\phi_{,t} + B\,\phi_{,\xi} = -D_{n,\xi}. \tag{2.11}$$

B expresses the rate of change in arc length with respect to a fixed axis of reference as measured by an observer that is always moving in the shock normal direction. It

can be expressed as a function of curvature and normal shock velocity,

$$B = \int_0^{\xi} \phi_{,\xi}\, D_n\, d\xi + B_0\,(t)\,. \tag{2.12}$$

The term $B_0\,(t)$ accounts for a finite angle between the shock normal and the axis of reference. By inspection of the equations above, the Lagrangian derivative of a variable is expressed as

$$\mathrm{D}/\mathrm{D}t = \mathcal{L} + (D_n - u_\eta)\ \partial/\partial\eta. \tag{2.13}$$

2.3 The Lagrangian derivative of temperature

The simplest concept of detonation failure is a decoupling of the reaction zone from the shock front, or equivalently, the failure of particles to rapidly undergo reaction after they cross the shock. Since most of the reaction rate laws are strongly temperature dependent, we now focus our attention to the Lagrangian derivative of temperature, $\mathrm{D}T/\mathrm{D}t$. To do so, we need to close the set of reactive Euler equations with a thermal equation of state. For simplicity, we consider a mixture of perfect gases

$$P = \rho\, R_g\, T, \tag{2.14}$$

where R_g is the mixture gas constant

$$R_g = \frac{\mathcal{R}}{W} = \mathcal{R} \sum \frac{y_K}{W_K}. \tag{2.15}$$

$\mathcal{R}$ is the universal gas constant, W the mixture molar mass and W_K is the molar mass of species K. The frozen sound speed is

$$c = \left(\frac{\gamma\, P}{\rho}\right)^{1/2}, \tag{2.16}$$

where γ is the ratio of mixture specific heats.

To analyze the relative importance of the wavefront local flow features, it is convenient to express $\mathrm{D}T/\mathrm{D}t$ in the intrinsic coordinate system described in the previous section. By taking the Lagrangian derivative of Equation (2.14), and using the adiabatic change equation (2.4) together with the mass and momentum equations in (2.8), we find the temperature reaction zone structure equation

$$\left(1-\frac{w_\eta^2}{c^2}\right) C_p \frac{\mathrm{D}T}{\mathrm{D}t} = \tag{2.17}$$

$$\begin{aligned}
&= \frac{1}{\gamma-1}\left(c^2-\gamma\, w_\eta^2\right)\,\dot{\sigma} && \text{heat release}\\
&+ w_\eta^2\,\frac{\kappa\,(D_n-w_\eta)}{1-\eta\,\kappa} && \text{curvature}\\
&+ w_\eta\,(D_n-w_\eta)_{,t}+\frac{P_{,t}}{\rho} && \text{unsteadiness}\\
&+ w_\eta^2\,\frac{w_{\xi,\xi}}{1-\eta\,\kappa} && \text{divergence}\\
&- w_\eta \frac{w_\xi^2\,\kappa}{1-\eta\,\kappa} && \text{centripetal}\\
&+ \frac{w_\xi}{1-\eta\,\kappa}\,(-w_\eta w_{\eta,\xi}+\frac{P_{,\xi}}{\rho}) && \text{N1}\\
&+ B\,(w_\eta\,(D_n-w_\eta)_{,\xi}+\frac{P_{,\xi}}{\rho}) && \text{N2}\\
&- \frac{\eta D_{n,\xi}}{1-\eta\,\kappa}\,(w_\eta\,(D_n-w_\eta)_{,\xi}+\frac{P_{,\xi}}{\rho}) && \text{N3}\\
&+ w_\xi\,w_\eta\,\frac{2\,D_{n,\xi}}{1-\eta\,\kappa} && \text{N4}
\end{aligned}$$

with $w_\eta = D_n - u_\eta$ and $w_\xi = u_\xi$. C_p is the mixture specific heat at constant pressure, $C_p = R_g\,\gamma/(\gamma-1)$. The left-hand side of Equation (2.17) has the dimension of energy density per unit time. The right-hand side has terms depending from the thermicity product, shock curvature, partial time derivatives of the flow, transverse divergence $w_{\xi,\xi}$, and also a term that has the appearance of work associated with centripetal motion. The remaining terms in (2.17) are more difficult to interpret, and are simply labeled N1 to N4.

The terms containing a partial time derivative in the intrinsic reference frame have been grouped together, and for the remainder of this work they will be referred

to as "unsteady terms" or "unsteadiness" for the fluid particle. For a decelerating wave such as in a detonation diffraction, the unsteady terms are negative. Thus, the reaction may quench if the wave is decelerating too rapidly. When the wavefront is convex-upstream, the curvature term is positive, and so it cannot possibly quench the reaction without the additional presence of unsteadiness.

If the axis of reference is also an axis of symmetry for the flow field, several terms disappear at $\xi = 0$. The transverse derivatives vanish, with the exception of $w_{\xi,\xi}$, and we obtain

$$\begin{aligned}
\left(1 - \frac{w_\eta^2}{c^2}\right) C_p \frac{\mathrm{D}T}{\mathrm{D}t} =& \frac{1}{\gamma - 1}\left(c^2 - \gamma\, w_\eta^2\right)\, \dot{\sigma} && \text{heat release} \\
&+ w_\eta^2\, \frac{\kappa_s\,(D_s - w_\eta)}{1 - \eta\,\kappa_s} && \text{curvature} \\
&+ w_\eta\, (D_s - w_\eta)_{,t} + \frac{P_{,t}}{\rho} && \text{unsteadiness} \\
&+ w_\eta^2\, \frac{w_{\xi,\xi}}{1 - \eta\,\kappa_s} && \text{divergence}
\end{aligned} \tag{2.18}$$

In Equation (2.18), $\kappa_s\,(t)$ and $D_s\,(t)$ are the front curvature and shock speed evaluated on the axis of symmetry. The result is the same found for a cylindrically symmetric flow with the addition of a transverse divergence term. This term is always positive since w_ξ is antisymmetric and no mass flux is allowed at the axis of symmetry.

The relative size and behavior of the terms in the temperature reaction zone structure equation will be examined numerically by following the path of massless particles injected into the flow. We will refer to these particles as Lagrangian. While this procedure can be applied to a general flow, the analysis can be restricted to regions where the shock is normal and the flow is parallel to the reference axis, so that Equation (2.18) can be used. Such regions are the channel axis of symmetry and the corner wall, i.e., the two boundary regions of a diffracting wavefront. The goal is to identify the dominant balance in a Lagrangian particle close to ignition failure and to find any simplifying assumption regarding the behavior of terms in (2.18).

We close this section by noting that an alternative formulation of the unsteadiness is obtained by rearranging momentum and mass conservation equations to give, under

conditions of symmetry,

$$w_\eta \left(D_s - w_\eta\right)_{,t} + \frac{P_{,t}}{\rho} = \frac{1}{\rho}\left(\frac{\mathrm{D}P}{\mathrm{D}t} - w^2 \frac{\mathrm{D}\rho}{\mathrm{D}t}\right) + w_\eta^2 \frac{\kappa_s \left(D_s - w_\eta\right)}{1 - \eta\,\kappa_s} + w_\eta^2 \frac{w_{\xi,\xi}}{1 - \eta\,\kappa_s}. \quad (2.19)$$

This formula is useful in the numerical evaluation of the unsteady terms of Equation (2.18), since it provides an alternative to computing directly the partial time derivative.

2.4 Quasi-steady, quasi-one-dimensional reaction zone

The reaction zone structure equations (2.8) can be simplified to a set of ordinary differential equations under the assumption that (1) the reference reaction zone length, Δ, is small with respect to the radius of curvature,

$$\kappa\,\Delta \ll 1; \quad (2.20)$$

and, (2) the characteristic timescale for the change in the shock speed is much longer than the passage time of fluid elements through the reaction zone

$$\tau = \Delta / w_\eta \ll D_n / \left(\mathrm{d}D_n/\mathrm{d}t\right). \quad (2.21)$$

The resulting equations are the conservation laws of quasi-one-dimensional reactive gas-dynamics with area change, and they admit steady-state solutions in the reference frame of the leading shock (Fickett and Davis 1979). These solutions are of particular interest in the study of the divergent reactive flow that is connected with a detonation diffracting through an abrupt area change.

When the area change is identically zero, and therefore the leading shock is planar, the quasi-steady reaction zone equations describe the standard ZND model. When the curvature is small, the transverse component of velocity, w_ξ, is zero to the leading order in curvature (Yao and Stewart 1996). By ignoring the derivative in ξ and the product $\eta\,\kappa$, the system in (2.8) takes a much simpler form as (Bdzil and Stewart

1989)

$$\frac{\mathrm{d}}{\mathrm{d}\eta}\left(\rho\, w_\eta\right) = -\rho\,\kappa\left(D_n - w_\eta\right) \tag{2.22a}$$

$$\rho\, w_\eta \frac{\mathrm{d}w_\eta}{\mathrm{d}\eta} + \frac{\mathrm{d}P}{\mathrm{d}\eta} = 0 \tag{2.22b}$$

$$\frac{\mathrm{d}}{\mathrm{d}\eta}\left(e + \frac{P}{\rho} + \frac{w_\eta^2}{2}\right) = 0. \tag{2.22c}$$

The species rate of change is

$$w_\eta \frac{\mathrm{d}y_K}{\mathrm{d}\eta} = \Omega_K \qquad (K = 1, \ldots, N)\,. \tag{2.23}$$

The relation between the area change and curvature is (Klein et al. 1995)

$$\frac{1}{A}\frac{\mathrm{d}A}{\mathrm{d}\eta} = \kappa\left(\frac{D_n}{w_\eta} - 1\right). \tag{2.24}$$

The three equations in (2.22) can be expressed in a more convenient form by using the adiabatic change equation (2.4), to obtain

$$\frac{\mathrm{d}P}{\mathrm{d}\eta} = -\rho w_\eta \frac{\dot\sigma - \left(D_n - w_\eta\right)\kappa}{1 - M_s^2} \tag{2.25a}$$

$$\frac{\mathrm{d}\rho}{\mathrm{d}\eta} = -\frac{\rho}{w_\eta}\frac{\dot\sigma - \left(D_n - w_\eta\right)\kappa\, M_s^2}{1 - M_s^2} \tag{2.25b}$$

$$\frac{\mathrm{d}w_\eta}{\mathrm{d}\eta} = \frac{\dot\sigma - \left(D_n - w_\eta\right)\kappa}{1 - M_s^2}, \tag{2.25c}$$

where M_s is the local flow Mach number, $M_s = w_\eta/c$, with respect to the shock front.

As in the temperature equation (2.17), the parameter $1 - M_s^2$ can be made to appear as a multiplying factor on the left-hand side of Equations 2.25, indicating a potential singularity. In fact, since in the propagating detonation the flow is subsonic immediately after the shock, the sonic parameter can pass through zero inside the reaction zone. Inspection of the structure equations indicates that the only way in which this can occur in a non-singular solution is for the numerator $\dot\sigma - \left(D_n - w_\eta\right)\kappa$

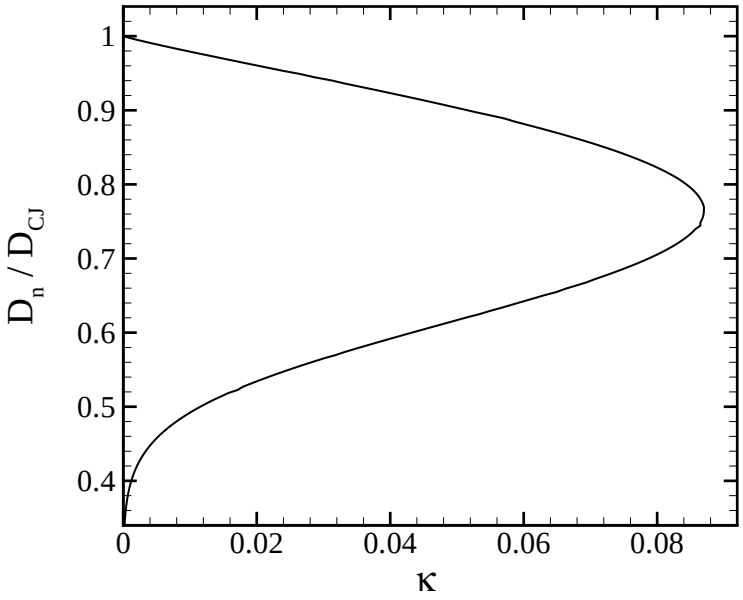

Figure 2.2: Example of $D_n\,(\kappa)$ relation for single-step reaction mechanism, $T_a = 4.15$ times the post-shock temperature. The curvature is normalized by the reference half-reaction length.

to vanish as $1 - M_s^2$ at a finite distance from the shock.

In the typical case of an overall exothermic reaction, the thermicity product $\dot{\sigma}$ is positive, and the existence of a sonic point indicates that the curvature must also be positive. Thus, a diverging flow tends to decelerate the initially subsonic flow behind the shock, while exothermic reactions tend to accelerate it. As a result, solutions to Equations (2.25) are non-singular only for certain values D_n and κ.

The case of a steady, slightly curved detonation can be treated as a generalized eigenvalue problem where only a particular value of shock curvature κ corresponds to a non-singular solution for a given normal shock velocity D_n. The relation between D_n and κ can be found by solving a two-point boundary problem with a regularity condition at the sonic point (Klein et al. 1995). For each pair D_n and κ, this method requires numerical integration of Equations (2.25), with the starting point provided by the post-shock (or von Neumann) state. Equivalently, the problem can be solved by a shooting method, where numerical integration starts from a generalized Chapman-

Jouguet (CJ) point and proceeds to the von Neumann point (Yao and Stewart 1995). The resulting $D_n(\kappa)$ relation typically exhibits a maximum value of curvature, κ_M, separating an upper and lower branch of a backwards C-curve, see Fig. 2.2. Stewart and Yao (1998) show that, very close to the ambient sound speed, another portion of the $D_n(\kappa)$ curve can be found, corresponding to a forward C shape, so that the overall diagram has the form of a Z-curve.

It should be noted that, even when $\kappa = 0$, computations with realistic reaction mechanisms provide an eigenvalue solution $D_n(0)$ that is different from the usual Chapman-Jouguet velocity, D_{CJ}. This latter value, derived from jump conditions, is in fact slightly lower than $D_n(0)$, and equal to it only when all the reactions are exothermic and irreversible (Klein et al. 1995). Particularly, if the thermicity is slightly negative at the end of the reaction zone, then a sonic point occurs where $\dot{\sigma} = 0$ before the reaction is completed.

For small but finite curvature, the thermicity is almost zero immediately behind the shock. Since the flow there is nearly isentropic, the velocity initially decreases in the diverging stream tube, while pressure, temperature and density increase. Further downstream, as the chemical energy is released into the flow, velocity, temperature and Mach number increase, while pressure decreases. The sonic point is reached at a finite distance from the shock, where the thermicity is still positive. Downstream of the sonic point, the solution can be either supersonic or subsonic, and the flow is similar to an expanding or, respectively, compressing isentropic flow in a diverging nozzle. As the wavefront becomes more curved, the location of the sonic point moves upstream, toward the shock. If a maximum curvature exists, then the reaction zone becomes completely subsonic for $\kappa \geq \kappa_M$. The initial subsonic portion of the flow field depends only on the post-shock state and remains qualitatively similar to the solution obtained when $\kappa < \kappa_M$.

2.5 The reaction mechanism

Before ending this chapter, we need to specialize the reaction model to the form that will be used in this work. The reaction model is a one-step irreversible reaction, $\mathrm{A} \rightarrow \mathrm{B}$, where the upstream fluid is undiluted species A. The reactant and product are taken to be perfect gases (constant specific heat) and to have the same specific heat ratio γ. Thus, the specific internal energies of species A and B are

$$e_{\mathrm{A}} = C_v T, \qquad e_{\mathrm{B}} = C_v T - Q,$$

where Q is the heat of reaction and C_v is the gas specific heat at constant volume. The progress variable Z is defined as the mass fraction of product B, $Z = y_{\mathrm{B}} = 1 - y_{\mathrm{A}}$ and the thermicity is

$$\dot{\sigma} = (\gamma - 1)\,\frac{Q}{c^2}\,\frac{\mathrm{D}Z}{\mathrm{D}t}. \tag{2.26}$$

The rate of reaction is expressed in Arrhenius form as

$$\frac{\mathrm{D}Z}{\mathrm{D}t} = k\,\rho\,(1 - Z)\,\mathrm{e}^{-E_a/R_g\,T}, \tag{2.27}$$

where the reaction order is $n_r = 2$ and E_a is the activation energy, $E_a = T_a\,R_g$. The proportionality factor, k, defines the spatial scale of the reaction zone.

Chapter 3

Numerical implementation

In this chapter, we discuss how the reactive Euler equations are discretized and solved on a parallel computer. We also show how we extract and post-process information from the numerical simulation to obtain shock and particle histories. The chapter is closed by the description of the initial and boundary conditions of the problem.

3.1 Variable normalization

Variables are non-dimensionalized by taking the uniform conditions upstream of the shock (with subscript 0) as a reference. For convenience, in this chapter dimensional variables are capped by a tilde. We have

$$\tilde{u}_{ref} \equiv (\tilde{R}_g \tilde{T}_0)^{1/2}, \quad u \equiv \frac{\tilde{u}}{\tilde{u}_{ref}}, \quad \rho \equiv \frac{\tilde{\rho}}{\tilde{\rho}_0}, \quad P \equiv \frac{\tilde{P}}{\tilde{P}_0}, \tag{3.1}$$
$$T \equiv \frac{\tilde{T}}{\tilde{T}_0}, \quad e \equiv \frac{\tilde{e}}{\tilde{R}_g \tilde{T}_0}, \quad E_a \equiv \frac{\tilde{E}_a}{\tilde{R}_g \tilde{T}_0}.$$

Length is normalized so that $\Delta_{1/2} = 1$. The time to travel the distance $\Delta_{1/2}$ at the reference particle velocity u_{ref} is also scaled to unity,

$$x \equiv \frac{\tilde{x}}{\tilde{\Delta}_{1/2}}, \quad y \equiv \frac{\tilde{y}}{\tilde{\Delta}_{1/2}}, \quad \tilde{t}_{ref} \equiv \frac{\tilde{\Delta}_{1/2}}{\tilde{u}_{ref}}, \quad t \equiv \frac{\tilde{t}}{\tilde{t}_{ref}}, \quad k \equiv \tilde{k}\,\tilde{t}_{ref}. \tag{3.2}$$

The non-dimensional equations of state become

$$P = \rho\, T, \tag{3.3a}$$

$$e = \frac{1}{\gamma - 1} T - Z\, Q, \tag{3.3b}$$

where $Q \equiv \tilde{Q}/\tilde{R}_g\, \tilde{T}_0$.

3.2 Numerical integration

The reactive Euler equations for a two-dimensional fixed reference frame and in non-dimensional conservative form, are

$$\frac{\partial \boldsymbol{W}}{\partial t} + \frac{\partial \boldsymbol{F}_x}{\partial x} + \frac{\partial \boldsymbol{F}_y}{\partial y} = \boldsymbol{S}, \tag{3.4a}$$

where

$$\boldsymbol{W} = \begin{pmatrix} \rho \\ \rho u_x \\ \rho u_y \\ E_t \\ \rho Z \end{pmatrix}, \quad \boldsymbol{F}_x = \begin{pmatrix} \rho u_x \\ \rho u_x^2 + P \\ \rho u_x u_y \\ (E_t + P) u_x \\ \rho u_x Z \end{pmatrix}, \quad \boldsymbol{F}_y = \begin{pmatrix} \rho u_y \\ \rho u_x u_y \\ \rho u_y^2 + P \\ (E_t + P) u_y \\ \rho u_y Z \end{pmatrix}, \tag{3.4b}$$

and

$$\boldsymbol{S} = \begin{pmatrix} 0 & 0 & 0 & 0 & k\rho(1 - Z)\mathrm{e}^{-E_a/T} \end{pmatrix}^T. \tag{3.4c}$$

$\boldsymbol{W}$ is the conservative solution vector, $\boldsymbol{F}_x$ and $\boldsymbol{F}_y$ are the convective fluxes in the Cartesian directions, $\boldsymbol{S}$ is the reaction source term, and $E_t = \rho(e + u_x^2/2 + u_y^2/2)$ is the total energy per unit volume. Numerical integration of Equation (3.4) is performed using operator splitting,

$$\boldsymbol{W}^{n+1} = \mathcal{L}_S\, \mathcal{L}_{FG} \boldsymbol{W}^n, \tag{3.5}$$

where the superscript indicates the number of timesteps. In one dimension, the convective operator, $\mathcal{L}_{FG}$, can be expressed for a uniform grid in a cell-based, finite-difference form, as

$$\boldsymbol{W}_i^{n+1} = \boldsymbol{W}_i^n - \frac{\Delta t}{\Delta x}\left(\boldsymbol{F}_{i+1/2}^n - \boldsymbol{F}_{i-1/2}^n\right), \tag{3.6}$$

where Δt is the timestep and Δx is the cell size. The subscript indicates the spatial cell number. $\boldsymbol{F}_{i+1/2}^n$ is the numerical flux at the interface between cells i and $i+1$, computed in the form of a conservative upwinding flux by using Roe's approximate solution of the Riemann problem (Roe 1986). Glaister's (1988) implementation for a general equation of state is adopted, with an extension for multi-species gases in chemical non-equilibrium. Second-order spatial accuracy is obtained via min–mod flux limiting, and the scheme is made entropy-satisfying with Harten's (1983) entropy fix. A detailed description of this implementation is found in Eckett (2001), together with verification results for one-dimensional detonation simulations with detailed chemistry mechanisms. The scheme is extended to more than one dimension via standard dimension-by-dimension integration. It is marched forward in time with the forward Euler integration scheme, which is first-order accurate.

The reaction source operator $\mathcal{L}_S$ involves the integration of the equation,

$$\frac{\mathrm{d}\boldsymbol{W}}{\mathrm{d}t} = \boldsymbol{S}, \tag{3.7}$$

which reduces to

$$\frac{\mathrm{d}Z}{\mathrm{d}t} = k\,\rho\,(1-Z)\mathrm{e}^{-E_a/T}, \tag{3.8}$$

with ρ, u and e constant. If the temperature were constant for this step, Equation (3.8) could be integrated exactly. Instead, integration is performed by a nominally second-order time-accurate predictor–corrector scheme. Equation (3.8) is first integrated for a half-timestep, with the temperature held constant. This gives an estimate for the average mass fraction in the timestep, $Z^{n+1/2}$. The temperature $T^{n+1/2}$ is then computed from the caloric equation of state (3.3b), noting that e is fixed for this step.

Finally, (3.8) is integrated for the whole timestep, using the average temperature $T^{n+1/2}$.

3.2.1 Parallel implementation

The flow solver described in the previous section is used to march the solution in time over a rectangular Cartesian grid. Boundary conditions are implemented at the sides of the patch by priming a bordering layer of guard cells with the appropriate values. The width of a layer of guard cells depends only on the flow solver stencil; it is 2 for the solver described above. As long as the grid sides are updated at each timestep, the integration of a patch can proceed independently from the neighboring patches.

Following this idea, a speed-up of the program execution time is obtained by partitioning the computational domain into smaller rectangular grids, and by assigning different groups of partitions (sub-domains) to different CPUs of a multi-processor computer. Partial superposition of grids is provided by the guard cells, so that each guard cell must lie on a computational cell of a neighboring patch, or border the outer boundary of the domain.

The Grid Hierarchy Adaptive Computational Engine library, GrACE, operates on these partitions by providing programming abstractions via a set of high-level parallel subroutines (Parashar et al. 1997; Parashar and Browne 2000). These functions hide the inner workings of the concurrent implementation to the rest of the application. The level of granularity of the parallel computation corresponds to the size of the grid partitions, and the basic parallel communication consists in populating the guard cells of a sub-domain by copying the values of the corresponding computational cells from a neighboring sub-domain.

The operations allowed by GrACE include creation and partitioning of the grid, generation and dynamic storage of grid data, and communication among grid partitions. Processors exchange information via the Message Passing Interface (MPI) protocol (refer, for instance, to Snir et al. 1996). In our calculations, patches are computed at the beginning of the simulation as a uniform partition of the computa-

tional domain, and then distributed over the available processors.

3.3 Shock and flow gradient tracking

Detonation speed and front curvature are reconstructed in a post-processing step from shock-tracking data collected during the simulation. Shock tracking is performed at each timestep after integrating the flow field. The tracking algorithm consists of a sequence of sweeps of the current solution in the x and y coordinate directions. For each sweep, we search the position of the first peak of density that emerges from the undisturbed flow. As the detonation front diffracts from a channel at the top left corner, the search is performed by scanning each computational patch from right to left and from bottom to top.

The shock location is taken as the position of the flex point in the numerical representation of the shock. The flex is defined as the midpoint between the peak value of density (the local von Neumann point) and the undisturbed value. Its position is estimated as a linear interpolation between the two grid points that bracket this value.

In the post-processing step, quantities such as the normal detonation velocity, D_n, and the local curvature, κ, are evaluated through finite-difference approximations for spatial and temporal derivatives of the shock position time history. When high-order derivatives are involved, this procedure requires particular care in controlling the error associated with the estimated shock position. Errors in the shock position are due to the use of linear interpolation in the shock profile and to high-frequency oscillations of the von Neumann state that occur when the wavefront crosses the interface between computational cells. A naive implementation of a finite-difference scheme could even diverge under grid refinement. This subject is treated in more detail in Appendix A.

Another problem in the treatment of shock position data points is the appearance of high-frequency oscillations in the finite-difference time derivative. The amplitude of these oscillations tends to grow as the shock position is sampled more frequently during the simulation. This artifact can be eliminated almost completely by numerical

convolution, i.e., by combining a kernel list with successive sublists of a list of data.

The convolution of a kernel K_r with a list $\{u_s\}$ has the general form

$$\sum_r K_r \, u_{s-r}. \tag{3.9}$$

For the results presented in this work, the kernel

$$K_r = \frac{1}{\sqrt{2\,\pi}} \exp\left(-r^2/\sigma_{K_r}^2\right) \qquad\qquad r = -n_{K_r} \ldots n_{K_r} \tag{3.10}$$

is used, with $\sigma_{K_r} = 10$ and $n_{K_r} = 20$. The result of the convolution operation has to be scaled by a factor $\sum_r K_r$ and padded with n_{K_r} zeros at the beginning and at the end of the list. We used the implementation of numerical convolution available in the commercial program "Mathematica" (version 4.0.2.0).

A similar technique is used to track the propagation of disturbances along the undisturbed front. The algorithm starts by locating the peak density along the axis of symmetry of the channel. Once this position is identified, the first grid point on the left (in the reaction zone) is taken as the starting point for a downward search of the computational grid. At each grid point of the scanning sequence, the y gradient of density is evaluated by a standard centered-difference formula and compared with a threshold value. As long as the detonation is planar, the transverse gradient value stays within numerical truncation error. The threshold values must be several orders of magnitude larger than the numerical truncation error, and yet small enough to identify slight fluctuations in the flow. With this setting, the downward scanning is arrested at the first grid point whose transverse gradient is larger than the threshold value. The position of this point is then recorded as the current position of the head disturbance immediately behind the shock, and saved in a data file.

3.4 Lagrangian particles

Lagrangian derivatives are evaluated by following the motion of fluid elements and recording the flow variables as a function of time. This is equivalent to injecting massless particles into the flow at specific locations. Since such particles would precisely follow the fluid motion, we refer to these as "Lagrangian particles." Flow field variables and the gradients of pressure and particle velocities in Cartesian directions are evaluated at each timestep in the numerical simulation at the four grid points surrounding a particle. They are then interpolated in space to the particle location by standard bilinear interpolation. The results are stored in a separate file for each particle and post-processed at the end of the simulation.

The Lagrangian derivatives in Equation (2.17) or Equation (2.19) are directly computed by finite-difference operations on the particle data stream. However, partial time derivatives (in the intrinsic reference frame) have to be estimated indirectly from the relation

$$\partial/\partial t|_{\xi,\eta} = D/Dt - w_\eta\,\partial/\partial\eta - w_\xi\,\partial/\partial\xi, \tag{3.11}$$

with the spatial gradients in η and ξ obtained by coordinate transformation from the stored gradients in x and y. When applied to situations where the partial time derivative is small compared to D/Dt (a limit case is a ZND detonation where $\partial/\partial t|_{\xi,\eta}$ is identically zero), the formula above is prone to cancellation errors. Since the partial time derivatives are combined in Equation (2.17) as

$$w_\eta\,(D_n - w_\eta)_{,t} + \frac{P_{,t}}{\rho},$$

an alternative solution is to evaluate this entire term directly from Equation (2.19). Figure 3.1 indicates that the two results can differ quite substantially.

Each term of the temperature equation (2.17) or (2.18) is estimated independently, so that an immediate check on the consistency of our particle data analysis is obtained by evaluating the difference between the left- and the right-hand sides of the equation as a function of time. We found that the use of Equation (3.11) tends to lead to a

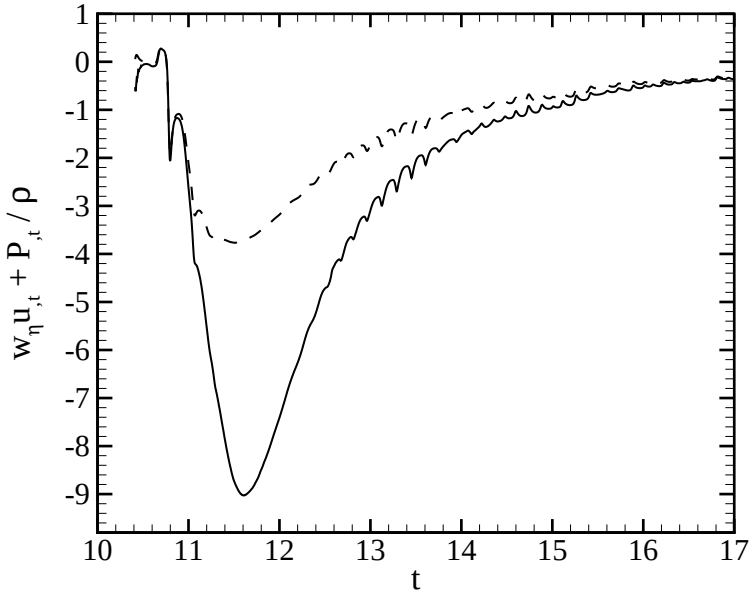

Figure 3.1: Comparison of unsteady term evaluations. Solid line: Equation (2.19). Dashed line: Equation (3.11).

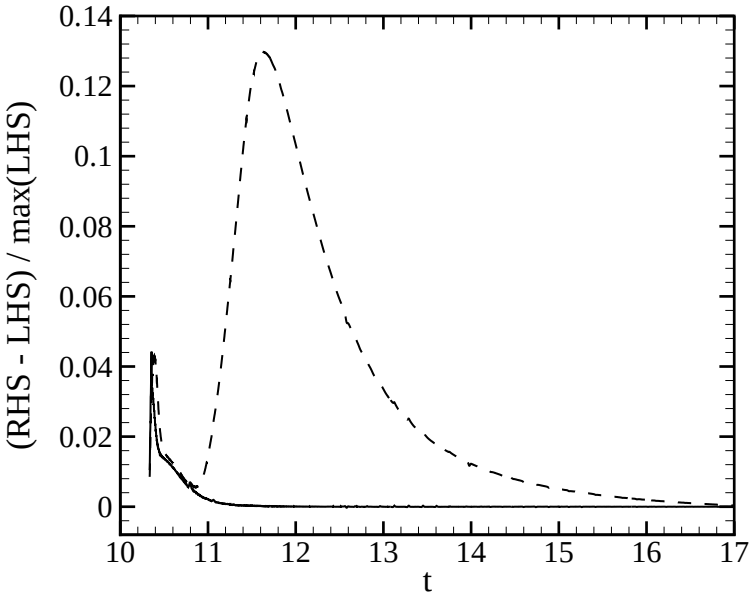

Figure 3.2: Comparison of the residual (left-hand side of Equation (2.18) minus right-hand side). Solid line: unsteady term computed via Equation (2.19). Dashed line: unsteady term computed via Equation (3.11).

larger residual than Equation (2.19). A typical result is plotted in Fig. 3.2, where the peak error mirrors the underestimate of the peak value of the unsteady group in Fig. 3.1. Figure 3.2 also shows that in both cases a large spike is found on the left of the plot at a point corresponding to the passage of the leading shock. The spike indicates that the spreading of the numerical shock over a few grid cells can strongly affect the evaluation of a Lagrangian derivative. Indeed, we found that our analysis cannot be consistently performed "inside the shock," and it has to be started after reading the first peak value in a particle's pressure data.

3.4.1 Lagrangian particles integration

The particles are assigned a position at an initial time and then convected by the flow field. Integration of the particle trajectory is performed with a Predictor-Corrector method in the form of an Adams-Bashforth predictor (P) followed by an Adams-Moulton corrector (C). Only one PC iteration is performed. The overall scheme is of the PECE type, where step E indicates the update of the derivative part from the last computed value (in *Numerical Recipes* 1992, pp. 747–751). Step P is computed before advancing the Euler equations by a timestep, and step C is computed after.

In a parallel calculation, particles need to be tracked as they are transported from one processor sub-domain to the next. To this end, a master-slave strategy is implemented (see, for instance, Wilkinson and Allen 1999). Only processor zero (the master) has the updated information concerning all particle positions. This information is sent to all the other processors (slaves) at the beginning of an integration step and collected by the master at the end of the integration. Each processor (including the master) integrates a particle for a timestep if and only if that particle currently belongs to the processor's sub-domain. After integration, the processor accesses the output file of that particle and dumps the new position, together with the interpolated flow field variables and gradients.

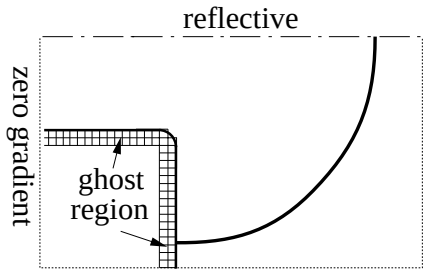

Figure 3.3: Boundary conditions.

3.5 Computational setup

3.5.1 Boundary conditions

In the numerical simulations, the corner is located at the bottom left of a rectangular Cartesian computational domain (Fig. 3.3). The flow is symmetric with respect to the top boundary, so reflective boundary conditions are used there. The flow at the inlet, initially at CJ conditions, becomes subsonic when the rarefaction signal from the corner moves upstream. For ease of implementation, a zero gradient condition is implemented there. To preserve for a sufficiently long time the corner expansion from perturbations coming from the left boundary, the inlet channel is $0.9\,H$ long. The implementation of the right and bottom boundaries is not relevant, since the simulation is terminated before the detonation front exits the domain.

To remove the singularity introduced in a Euler (inviscid) flow around a sharp vertex, the boundary is approximated by polygonal segments as a rounded corner, with radius of curvature r_c. The effect of a finite value r_c on the detonation velocity at the wall is examined in Appendix B at decreasing radii of curvature. It is found that when r_c is of order one or smaller, the finite curvature affects the flow field only to a distance of a few multiples of r_c from the corner.

Since a few computational cells are cut by the rounded corner, a special treatment is needed in order to use the simple patch integrator described in Section 3.2. The corner boundary is implemented by using the ghost-fluid coupling scheme described in Arienti et al. (2002). This technique, designed to handle fluid-solid interactions, is specialized here to model an arbitrary rigid boundary embedded in a Cartesian grid.

A requirement of the ghost-fluid algorithm is the construction of a level set function φ providing every grid point with the signed distance from the embedded boundary. Since in this application the boundary is rigid, the level set is computed only once at the beginning of the simulation. The zero value of the distance function represents the embedded boundary. Negative values conventionally correspond to the fluid region, where the flow field is computed. In the positive level set field, a tiny strip of cells (called *ghost cells*) is used to compute numerical fluxes in cells close to the boundary.

As with the guard cells described in the previous section, the ghost cells need to be updated before every convective step. They border an arbitrarily irregular embedded boundary, and are populated by extrapolation from the neighboring fluid cells. The prescription for updating the ghost cells is that the embedded boundary is an impermeable wall. An additional condition for an Euler flow is that the boundary is an inviscid wall, i.e., the flow slips along the wall. One way to approximate these two prescriptions is to advect density, internal energy, and the Cartesian components of velocity following the gradient of the level set, from the fluid to the ghost region,

$$I_\tau + \mathbf{n} \cdot \nabla I = 0, \tag{3.12}$$

where I is the advected scalar, $\mathbf{n} = \nabla\varphi / |\nabla\varphi|$, and τ is a pseudo-variable of integration. The boundary condition in Equation (3.12) is provided by the scalar values in the fluid cells that are closest to the boundary. After the advection step, the state of a ghost cell (G) is formulated in terms of the advected quantities (E),

$$\begin{pmatrix} \rho_G \\ \mathbf{V}_G \\ e_G \end{pmatrix} = \begin{pmatrix} \rho_E \\ (-\mathbf{V}_E \cdot \mathbf{n})\ \mathbf{n} + (\mathbf{V}_E \cdot \mathbf{t})\ \mathbf{t} \\ e_E \end{pmatrix}. \tag{3.13}$$

This implementation of a reflective boundary is accurate to first order in the grid resolution (Arienti et al. 2002). When the boundary is moving, an additional term, the local normal velocity vector of the wall, needs to be taken into account.

In the simulations that are presented in Chapter 4, the corner boundary is described by a sequence of 2048 points. Of these points, 128 are used to approximate the arc of circle of radius $r_c = 1$. The distance function is computed at each grid point by searching for the shortest distance in the list of segments that compose the boundary. The sign of the distance function is found by ray-intersection, a popular approach for determining whether a point lies inside or outside of a surface (a process known as point-classification, Hoffmann 1989). When implemented in this way, the construction of the level set is cumbersome, since one needs to examine all the grid points and all the boundary points. This is tolerable in applications with rigid boundaries and no regridding, where the level set is computed only once.

3.5.2 Initial conditions

The initial solution is a planar ZND wave (see Section 2.4), traveling from left to right in the inlet channel bounded by the corner upper wall, the axis of symmetry, and the left boundary of the computational domain. The ZND profile is computed by numerical quadrature of the set of equations (2.25) in the case of a single-step reaction model. It is found more convenient to integrate the reaction zone structure equations in the progress variable Z, through the differential relation

$$\frac{\mathrm{d}Z}{\mathrm{d}\eta} = \frac{\Omega}{w_\eta}, \tag{3.14}$$

where the chemical rate Ω is specified by the right-hand side of Equation (3.8).

The value of specific heat estimated from the experiments with acetylene described by Edwards et al. (1979) is $\gamma = 1.22$. The reference state ahead of the shock is given by $\tilde{P}_0 = 23,998$ Pa and $\tilde{T}_0 = 298$ K. With these data, the program STANJAN (Reynolds 1986) finds a Chapman-Jouguet detonation speed $\tilde{D}_{CJ} = 2346.1$ m/s, corresponding to the Mach number 7.422, and gas constant $\tilde{R}_g = 274.4$ J/Kg/K. Once D_{CJ} is known, the heat release Q is computed as the solution of

$$D_{CJ}/\sqrt{\gamma} = \sqrt{\mathcal{H}+1} + \sqrt{\mathcal{H}} \tag{3.15}$$

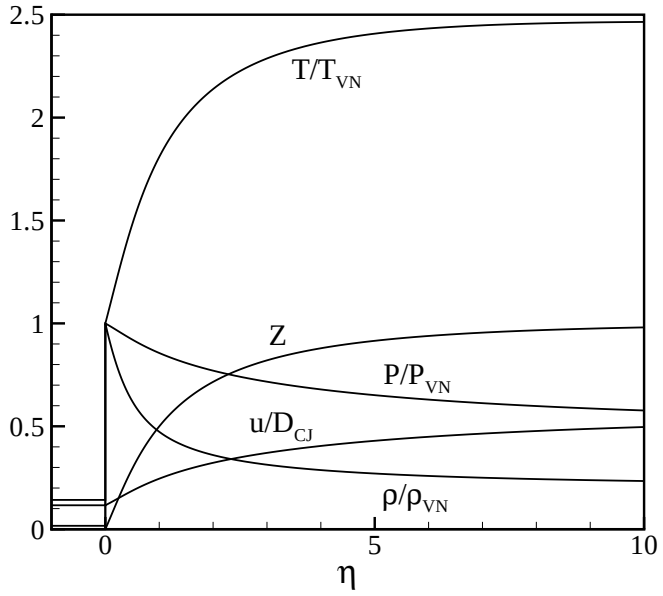

Figure 3.4: Pressure, density, temperature, progress variable and particle velocity as a function of the distance from the shock η in a ZND profile computed for a single-step reaction model with zero activation energy. The particle velocity is divided by the Chapman-Jouguet detonation speed D_{CJ}, whereas all the other variables are normalized by the corresponding post-shock (von Neumann) values.

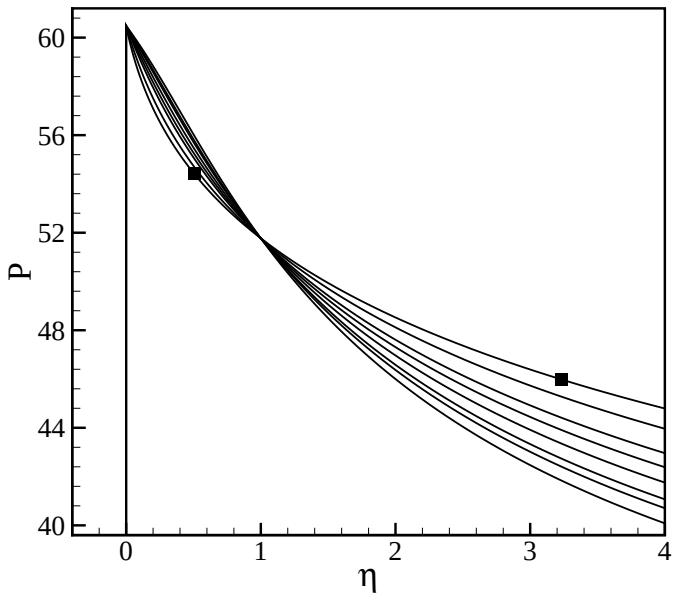

Figure 3.5: ZND pressure profiles versus distance from the shock. The curves are computed from the values of θ_{CJ} and k listed in Table 3.1. The line passing through the square symbols corresponds to zero activation energy.

θ_{CJ}:	0.	1.	2.	2.5	3.	3.5	3.75	4.15
k :	0.2013	0.3931	0.7757	1.077	1.551	2.204	2.632	3.509

Table 3.1: Non-dimensionalized activation energy and proportionality factor.

in the unknown $\mathcal{H}$

$$\mathcal{H} = \frac{(\gamma - 1)(\gamma + 1) Q}{2\gamma}, \tag{3.16}$$

see Thompson (1988). With the normalized speed $D_{CJ} = 8.204$, we find $Q = 65.81$.

Numerical integration of the quasi-steady, one-dimensional Euler equations is performed by an adaptive solver using a non-stiff Adams and a stiff Gear Method, as implemented in "Mathematica" (version 4.0.2.0). A computed ZND profile with a moderately high activation energy E_a is displayed in Fig. 3.4.

In the next chapter, we present the results of a parametric study where the geometry of the channel (namely the half-width H of the inlet channel) is kept fixed while varying the activation energy, scaled by the CJ post-shock temperature, T_{vN},

$$\theta_{CJ} = \frac{E_a}{T_{vN}}.$$

Changing θ_{CJ} modifies the rate of energy release in the ZND profile and the sensitivity of the reaction rate to variations in the thermodynamic state. To consistently compare different profiles computed for different values of θ_{CJ}, the proportionality parameter k in the reaction rate formula (3.8) must also be changed. In Table 3.1, we list θ_{CJ} and the respective values of k that provide a constant value $\Delta_{1/2} = 1$. Figure 3.5 displays the corresponding ZND profiles of pressure. These profiles cross each other a first time at $\eta = 1$ and a second time at the sonic locus. For a depletion law of order one, Equation (3.8), this point is at an infinite distance from the shock and it is not visible in Fig. 3.5. Once the ZND solution is computed, it is interpolated on the inlet channel to generate a right-facing planar wave, whose normal is parallel to the x axis. No initial perturbations are introduced, so that the wave remains planar until it reaches the corner, where it starts to diffract.

Chapter 4

Activation energy studies

Activation energy E_a is the key parameter determining the dynamics of any combustion system described by a one-step Arrhenius rate model. Large values of the activation energy result in a chemical reaction rate that is very sensitive to changes in the thermodynamic state. Small values of activation energy result in a chemical reaction rate that is almost independent from changes in the thermodynamic state. As a consequence, the diffraction behavior of detonations modeled with an Arrhenius rate law can vary widely depending on the magnitude of the activation energy. In the present study, a range of values has been examined in order to map out the possible types of diffraction behavior that can occur with a fixed ratio of reaction zone length to channel height.

Two types of studies were carried out. First, a set of coarse-resolution simulations were performed for 8 values of reduced activation energy

$$\theta_{CJ} = \frac{E_a}{T_s} \tag{4.1}$$

between 0 and 4.15. Second, a set of high-resolution simulations were carried out for three selected cases with reduced activation energies of 1, 3.5, and 4.15. All of these simulations were performed with an initially planar ZND wave traveling at the CJ speed before diffracting around the corner. Normal mode stability analysis (Lee and Stewart 1990) indicates that the neutral stability curve for one-dimensional CJ detonations asymptotes to a constant value $\theta_{CJ} \cong 4.74$ for sufficiently large Mach numbers

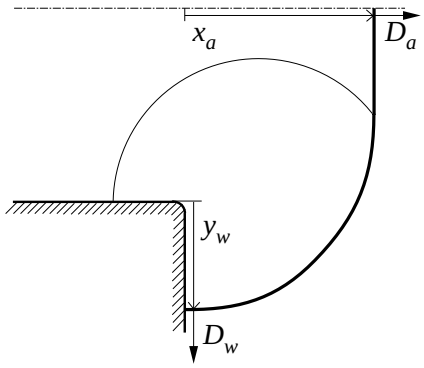

Figure 4.1: Distance from the corner, measured along the channel axis of symmetry, x_a, and along the corner wall, y_w.

($M_{CJ} > 6$). Our simulations lie entirely within the range of one-dimensional hydrodynamic stability, allowing the study of purely gasdynamic quenching mechanisms in detonation diffraction.

Computations were carried out over a sufficiently long time to determine the ultimate fate of the detonation wave. The half-width H of the channel in these simulations was fixed at 36.67 reaction half-lengths. The kinetic constant k was selected as a function of θ_{CJ} to maintain $\Delta_{1/2}$ constant, see Table 3.1.

The results of this study are conveniently summarized by plotting the history of the detonation velocity on the axis of symmetry, D_a, and at the wall, D_w, as shown in Fig. 4.1. The coarse-resolution studies were carried out with 16 grid points per half-reaction zone length, $N_{1/2} = 16$. This resolution level was convenient since it enabled a complete simulation (on a 4824 by 3752 grid) to be performed in less than 36 wall-clock hours on 48 processors (Pentium III, 1 GHz with 1 GB of RAM) of the ASAP Linux cluster in the Center for Advanced Computing Research (CACR) at Caltech.

4.1 Coarse-resolution studies

The history of axial and wall velocities is presented in Figs 4.2 and 4.3 as a function of position x_a or y_w as shown in Fig. 4.1. The shock speed on the axis remains constant until the first expansion wave reaches the axis at about 90 half-reaction lengths from

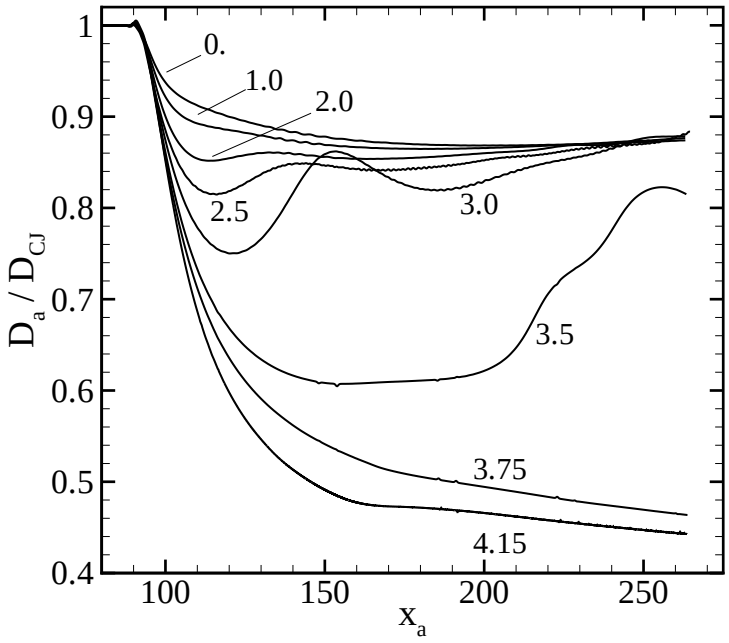

Figure 4.2: Detonation velocity at the axis, D_a, as a function of the distance measured from the vertex, x_a. The labels are values of the non-dimensional activation energy θ_{CJ}, varying from 0 to 4.15.

the corner vertex location. The expansion initially causes the shock speed to decay in all cases, but the long-time behavior is different depending on the values of reduced activation energy. The shock speed at the wall drops instantly since the flow around the corner immediately affects the shock front. The very low pressures in the region of the corner cause the shock to initially propagate at much lower velocities along the wall than along the axis. Overall, in this initial phase of corner diffraction, the behavior of diffracting detonations is very similar to that observed with non-reacting shock waves.

For longer times, two extreme types of behavior can be noted for low activation energy and high activation energy. These behaviors resemble the super-critical (low activation energy) and sub-critical (high activation energy) diffraction cases observed in experimental studies of diffraction from tubes. In addition, the cases of intermediate activation energy appear to be similar to the critical case of diffraction from tubes. However, it is important to keep in mind two key differences between exper-

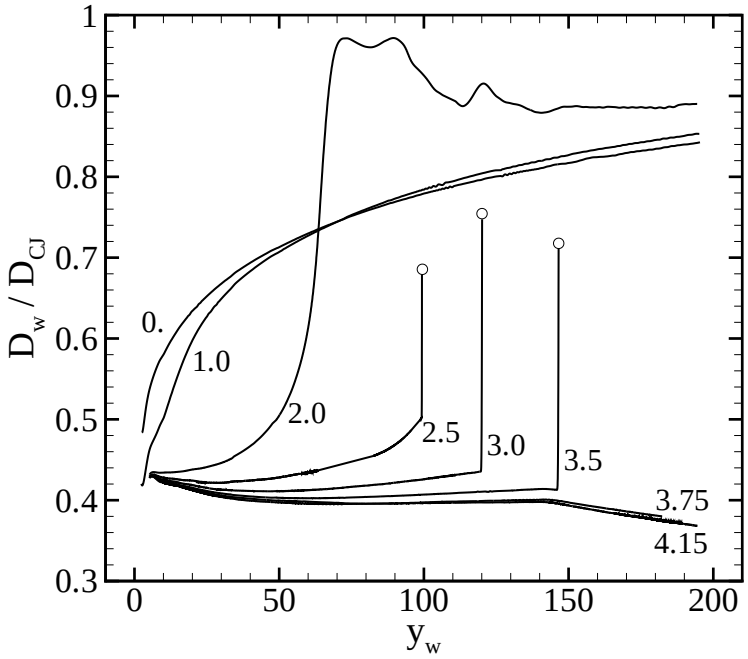

Figure 4.3: Detonation velocity at the corner wall, D_w, as a function of the distance from the vertex, y_w. The labels are values of the normalized activation energy θ_{CJ}, varying from 0 to 4.15.

iments and the present simulations. First, the effective activation energy is between 4 and 7 for most fuel-oxidizer combinations (Schultz 2000). Second, there are always transverse waves present on the detonation prior to reaching the corner. So the correspondence between experiment and present simulations is necessarily inexact. More realistic computations are needed in future studies to examine the influence of these two factors.

4.1.1 Low activation energy

For $0 \leq \theta_{CJ} \leq 1$, the reaction rate is essentially independent from the thermodynamic state, so that the reaction zone length is unaffected by the shock velocity. Since the reaction rate is nearly constant, the detonation will always accelerate after diffraction, reaching the CJ velocity far from the corner. This is similar to the case of supercritical diffraction that is observed in diffraction experiments (discussed in Chapter 1) where the tube is larger than the critical size needed for successful detonation

transmission.

Upon examination of Figs 4.2 and 4.3, a simple picture of the low activation energy case emerges. The detonation velocity initially decreases due to the expansion waves created by the flow around the corner, yet, after the initial decay, the wave accelerates and eventually approaches the CJ velocity at a large distance from the corner. The velocity on the axis of symmetry drops slowly to about 88% of the CJ velocity and then begins to recover after propagating to 200 half-reaction lengths along the axis (Fig. 4.2). The velocity on the wall drops immediately to 40% of the CJ value and recovers to about 80% of CJ by the time the shock has propagated 200 half-reaction lengths along the wall (Fig. 4.3). The magnitude of the drop in the shock velocity and the rate of acceleration are associated with the competition between the gasdynamic expansion created by corner flow and the energy release immediately behind the shock. For this situation, the rate of change of the shock velocity can be shown to be directly related to the magnitude of the velocity gradient behind the shock through the shock-change equation (Fickett and Davis 1979, p. 101).

4.1.2 High activation energy

For $3.75 \leq \theta_{CJ} \leq 4.15$, the reaction rate is strongly dependent on the thermodynamic state so that the reaction zone length increases rapidly when the shock speed decreases. This causes the reaction zone to decouple from the shock wave, and the reaction rate to essentially drop to zero, after a short distance from the corner vertex. The detonation fails completely and the resulting flow is essentially a non-reactive shock wave. This is similar to the case of sub-critical diffraction that is observed in diffraction experiments (discussed in Chapter 1) where the tube is smaller than the critical size needed for successful detonation transmission.

Examining Figs 4.2 and 4.3, we find that there is also a simple pattern of behavior for this case. The wave velocity on both the axis and the wall decrease continuously and reach very low values, less than 50% of the CJ value at 200-250 half-reaction lengths from the corner vertex. The dynamics of the wave propagation are essentially

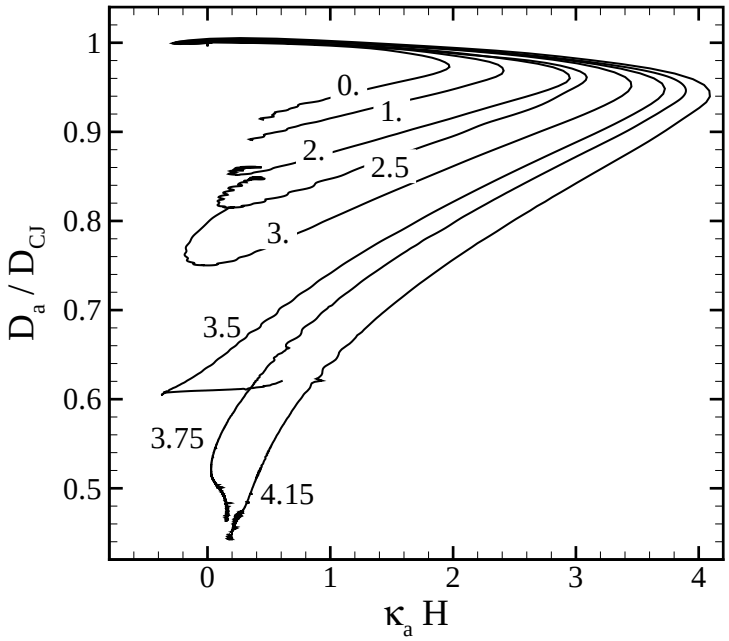

Figure 4.4: Detonation velocity - curvature ($D_n - \kappa$) diagram at the axis of symmetry of the channel. The labels are values of the normalized activation energy θ_{CJ}, varying from 0 to 4.15.

those of a non-reactive shock and the approximate method of Whitham (1974) can be used to find the evolution of the front.

4.1.3 Intermediate activation energy

For $2.5 \leq \theta_{CJ} \leq 3.5$, the reaction rate is moderately dependent on the thermodynamic state. The reaction zone length increases as the shock decays, but the accelerating effects of energy release are sufficient to cause the reaction zone length to ultimately decrease in an abrupt fashion. This gives the appearance of a re-ignition event near the wall (Fig. 4.3) that propagates back to the axis. This is similar to the case of critical diffraction that is observed in diffraction experiments (discussed in Chapter 1) where the tube is comparable to the critical size needed for successful detonation transmission.

The axial and wall velocities show an initial decay to a velocity higher than that observed in the high activation energy cases, followed by an acceleration back to

velocities similar to the low activation energy cases. The acceleration is abrupt at the wall, but more gradual on the axis. This is related to the mechanism of transition, discussed in more detail below.

Another way to analyze the flow near the axis is to plot wave speed vs. curvature (Fig. 4.4). As discussed in Section 2.4, a unique $D_n(\kappa)$ relationship should result if the flow is quasi-steady in nature. Although the curves of Fig. 4.4 appear similar to the plot in Fig. 2.2, their numerical values can be very different than in the corresponding $D_n(\kappa)$ curves. These differences are examined in Section 5.2.

4.2 High-resolution studies

Following the results of the coarse-resolution studies, more detailed simulations were performed for selected cases at high resolution. The need for highly resolved computations is crucial in the study of detonation diffraction. When the reaction zone is underresolved, direct numerical simulations tend to overestimate the wave-front curvature (Menikoff et al. 1996), and poor predictions of detonation wave structure can be expected (Sharpe 2001). Results from a convergence study with varying $N_{1/2}$ are presented in Appendix C. The following three simulations were computed with $N_{1/2} = 22.5$ on a 6570 x 5858 grid for $\theta_{CJ} = 1$ and 3.5, and on a 6750 x 5100 grid for the sub-critical case. In all the examples, the length of the computational domain is $300\,\Delta_{1/2}$. A non-dimensionalized time-step of $1.144 \cdot 10^{-3}$, corresponding to an average CFL number of 0.5 or smaller, is used in all calculations. Given a final time between 40 and 60 for the detonation front to reach the bottom of the computational domain, a typical simulation needs at least $40,000$ iterations to reach completion. This requirement translates into an execution time of at least 6 days on 48 processors (42 for the sub-critical case).

4.2.1 Case $\theta_{CJ} = 1$

A sequence of numerical schlieren images is displayed in Fig. 4.5. Schlieren visualization amounts to displaying the magnitude of the density gradient as a gray-scale.

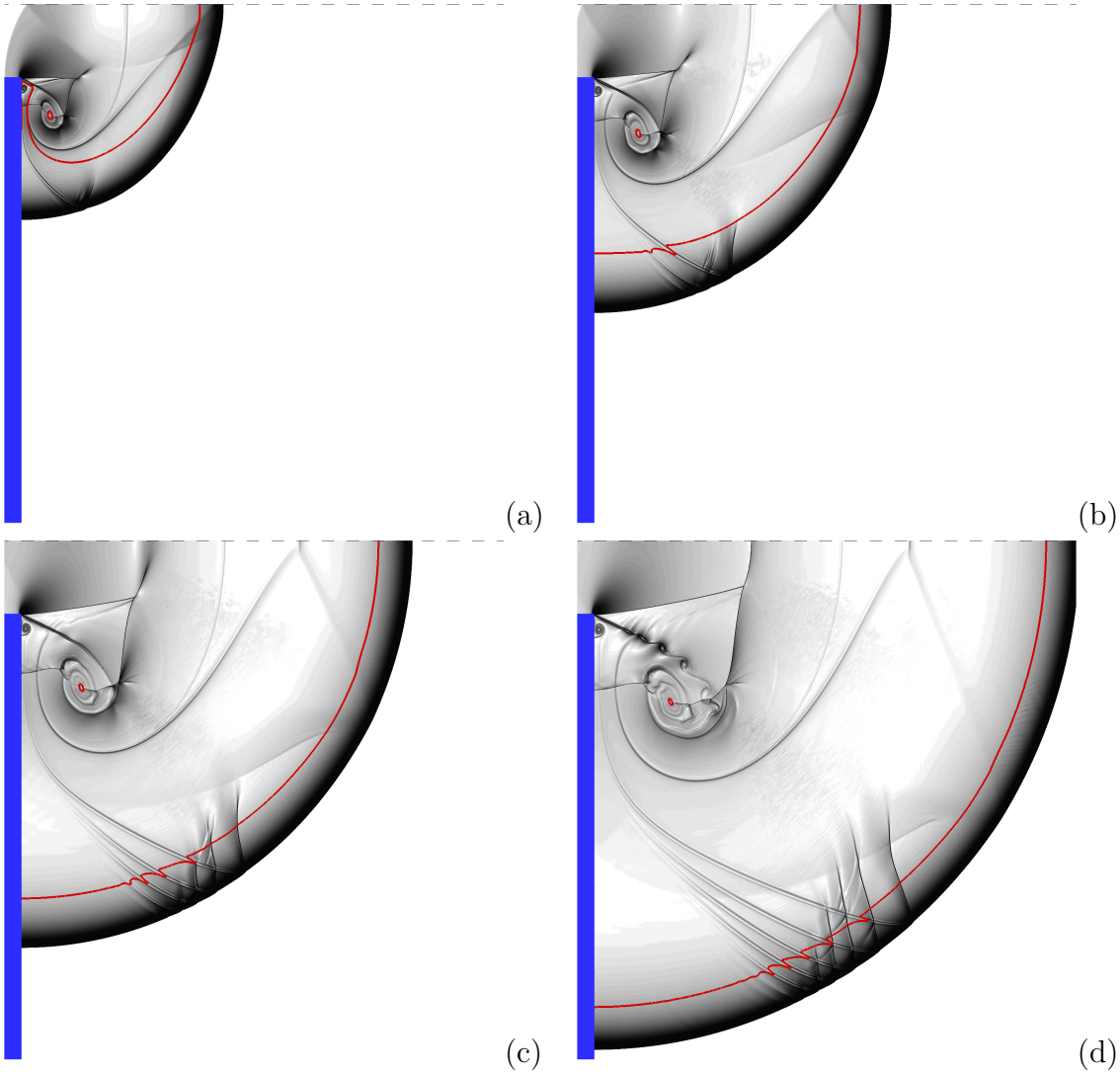

Figure 4.5: Numerical schlieren images for the case $\theta_{CJ} = 1$. (a) $t = 13.83$; (b) $t = 21.15$; (c) $t = 28.47$; (d) $t = 35.79$.

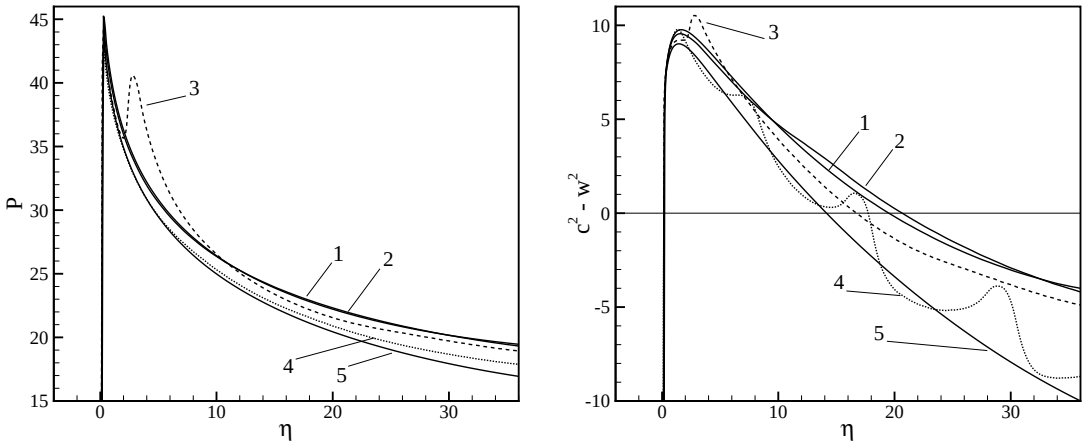

(a) (b)

Figure 4.6: Pressure profile (a) and sonic parameter (b) for 5 data sets extracted at $t = 35.79$. Slice 1 and 5 are extracted along the axis of symmetry and the corner wall, respectively. The remaining data are taken in the shock normal direction and are evenly spaced along the detonation front.

A nonlinear mapping, or gray-scale shading function, is used so that density gradients varying through several orders of magnitude are still visible. In this work, the gray-scale shading function is

$$\nu = 0.8 \exp\left(-\mu \frac{|\nabla\rho|}{|\nabla\rho|_{max}}\right) \tag{4.2}$$

with μ a strictly positive amplification parameter. The gray-scale ranges from black for $\nu = 0$ to white for $\nu = 1$. Larger values of μ give darker images and accentuate weak features of the flow. To provide a consistent gray-scale reference, frames in a sequence of schlieren images, such as the one in Fig. 4.5, have the same amplification and normalization factors.

In addition to the density gradient, Fig. 4.5 also displays the locus of points where the products mass fraction is equal to 0.95. This contour is displayed as a red line. The corner, on the left-hand side of each plot, is shown as a rectangular shape with a small (not visible to the eye) rounded vertex of radius $r_c = 1$. In each frame, only the last portion of the inlet channel (one fifth of the total length $0.9\,H$) is shown.

As mentioned in the previous section, a value $\theta_{CJ} = 1$ corresponds to a reaction

rate model that is insensitive to shock velocity changes. Figure 4.6 (a) is a plot of pressure for 5 "slices" of the computational domain at time $t = 35.79$. Slice 1 and 5 are extracted along the axis of symmetry and the corner wall, respectively. The remaining data are taken in the shock normal direction and are evenly spaced along the detonation front. In all the slices, the post-shock pressure is almost exactly 75% of the von Neumann value, corresponding to a detonation velocity $0.86 D_{CJ} = 7.010$. This estimate is consistent with the diagram in Fig. 4.2. The profiles of the sonic parameter $c^2 - w^2$ in frame (b) are computed by assuming the shock is normal. Then $w = 7.010 - u$ is the relative velocity, with $u = (u_x^2 + u_y^2)^{1/2}$. A sonic point is observed for all profiles at a distance varying between 14 and 21 $\Delta_{1/2}$ from the shock. No decoupling of the shock from the reaction zone occurs, since the 50% reaction completion is reached at a distance of about $1.5\,\Delta_{1/2}$. Overall, the profiles in the two frames show the same behavior as a function of the coordinate η, with the exceptions of slice 3 (dashed line) and slice 4 (dotted line) both passing through a system of transverse shocks. Transverse shocks, visible in Fig. 4.5 (d), will be discussed in the second half of this section. Similar profiles are also observed for the other flow variables, not displayed here, indicating that there are no residual effects of the transverse gradient due to the corner rarefaction. By the shock-change equation (Fickett and Davis 1979, p. 101), we conclude that the front is propagating as an almost cylindrical detonation.

In the remaining part of this section, we examine the most relevant features of this super-critical diffraction in detail. Figure 4.7 is a close up of the frame at time $t = 28.47$, showing the vortex structure near the corner. To clarify the picture, we display a plot of contours of $u^2/c^2 - 1$, where u is the magnitude of the local flow field velocity in the laboratory frame and c the local sound speed. The contours have values ranging from -1 to 8, with spacing equal to 0.25. Dashed lines correspond to $u \leq c$ and solid lines to $u > c$, so that every dashed contour that is adjacent to a solid contour represents a sonic line in the laboratory frame.

At the center of the vortex V, we recognize a portion of partially reacted material surrounded by the 0.95 reaction locus. Once formed at the corner, this partially burnt

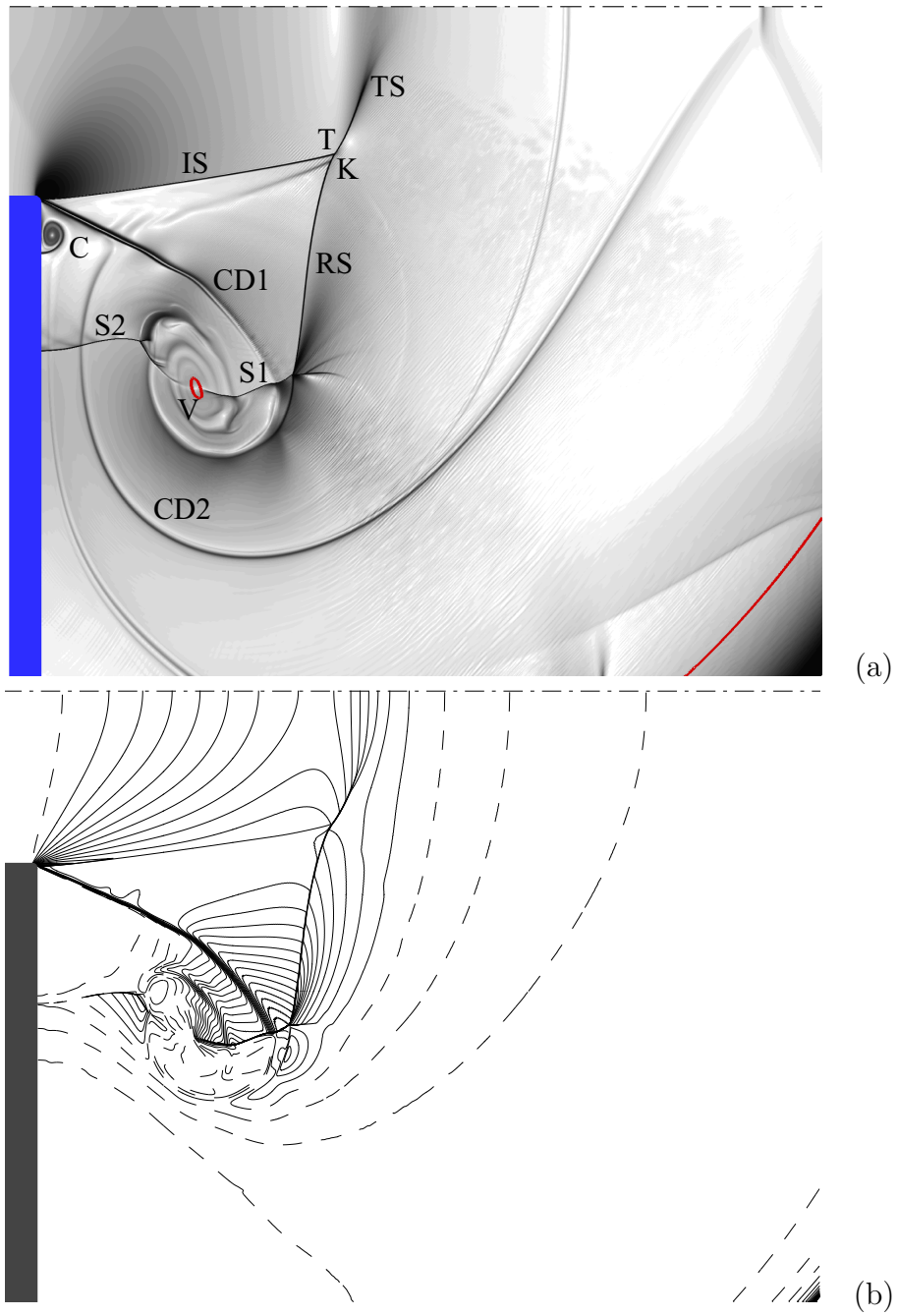

Figure 4.7: Numerical schlieren image, (a), and contours of $u^2/c^2 - 1$, (b). The red line is the 0.95 reaction locus. In (b), the contours have values ranging from -1 to 8, with spacing equal to 0.25. Dashed lines correspond to $u \leq c$ and solid lines to $u > c$. Every dashed contour that is adjacent to a solid contour represents a sonic line in the laboratory frame. The plots are a close up of the frame at $t = 28.47$ in Fig. 4.5, computed for $\theta_{CJ} = 1$.

core is slowly convected downstream by the flow field. As the vortex rotates clockwise, it wraps around it a contact discontinuity (CD1) produced by the acceleration of the flow at the corner. The discontinuity separates flow at low speed, creeping along the vertical wall, from flow at higher speed coming from the channel inlet. A second contact surface (CD2) surrounds the vortex and reaches the axis of symmetry. CD2 separates the fluid that has been processed by the undisturbed shock from the fluid that has been set into motion by the diffracted shock.

Examining the channel inlet shows that, at time $t = 28.47$, the head of the corner expansion has already moved upstream inside the channel, and that the incoming flow is subsonic. This flow expands at the corner, passes through a sonic line (Fig. 4.7 (b)) and becomes supersonic. It is then slowed down by a system of shock waves converging to a triple point, T. In Fig. 4.7 (a), we recognize a weak incident shock (IS), from the corner to the triple point; a stronger reflected shock (RS), reaching the slip discontinuity CD1; and a transmitted shock (TS), terminated by a system of compression waves that extend to the axis of symmetry. At a later time these compression waves have coalesced into a well-defined shock, perpendicular to the axis. The contact discontinuity, separating the fluid processed by RS and TS, is so weak that it is visible only as a kink in the contour lines on the right of RS in frame (b). In frame (a) we distinguish more clearly a kink (K), at a short distance from T, due to a small compression wave that is formed in the early phases of the corner turning process. This wave becomes progressively weaker at later times.

At the termination of the reflected shock, close to CD1, a complex system of shocks and contacts can be discerned. The shock (S1) originates from this area and almost reaches the vortex center. A second shock (S2) extends from the core to the corner wall. Both shocks reduce the flow velocity, which passes from supersonic to subsonic, see frame (b). In the recirculation region between S2 and the contact discontinuity, a small counter-vortex (C) can be identified. The flow processed by RS and TS becomes subsonic at a certain distance from the shock, and this region of locally subsonic flow extends past the 0.95 reaction locus in frame (a) to the main reaction zone. We see that the flow once again becomes supersonic in the laboratory frame near the leading

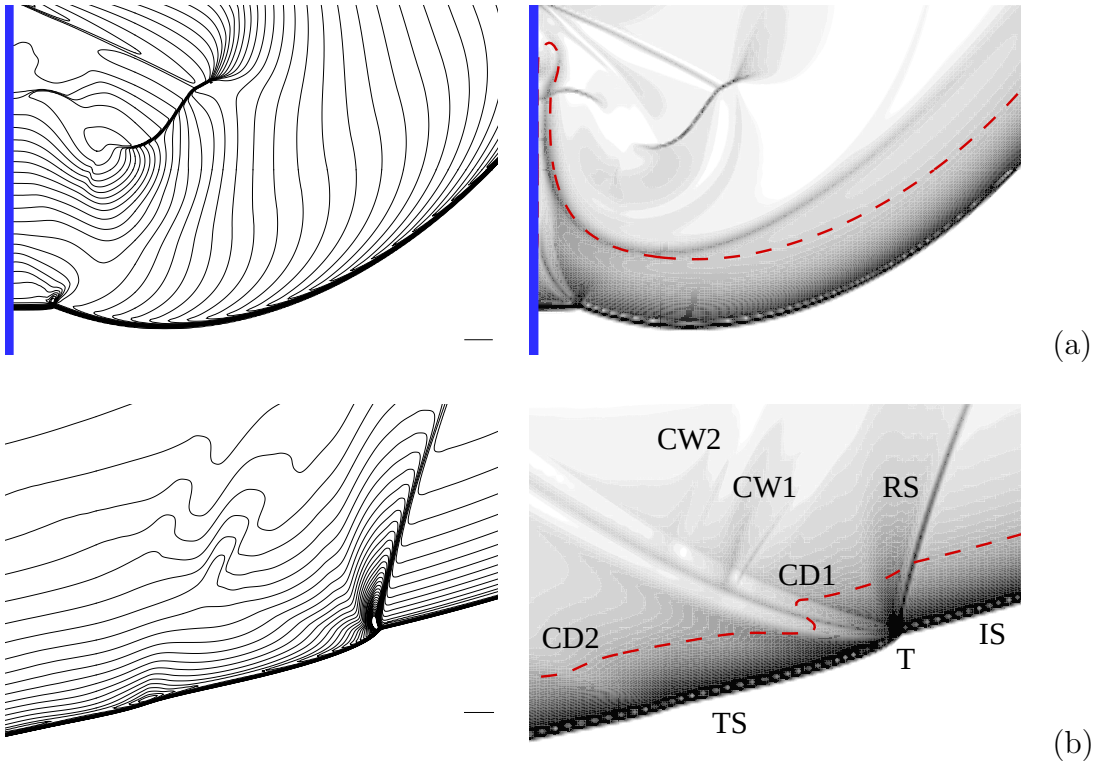

Figure 4.8: Contours of pressure (left), and numerical schlieren images of density (right) at time $t = 8.5$ (a), and $t = 13.83$ (b), computed for $\theta_{CJ} = 1$. The pressure increment of the contours is 0.8334 up to a cutoff value of 50 times the ambient pressure. The reference segment (bottom right corner of the contour plots) measures $\Delta_{1/2}$.

front, in the bottom right corner of frame (b).

Most of the features we have described can also be observed in experiments of shock diffraction in non-reactive mixtures (see Shardin's shadowgraphs at $M_0 = 2.4$ in *An Album of Fluid Motion* plate 243, assembled by Milton van Dyke, Parabolic Press, 1982). This complex system, once formed, grows in a self-similar fashion until instabilities eventually grow along the contact discontinuity (after time $t = 35.79$ in Fig. 4.5).

We now examine the detonation front, where Fig. 4.5 reveals the formation of a train of shock waves, extending through the reaction zone and transverse to the main front. Figure 4.8 is composed of schlieren images and contour plots of pressure. The pressure increment of the contours is 0.8334 up to a cutoff value of 50 times the ambient pressure. The reference segment (bottom right corner of the contour plots)

measures $\Delta_{1/2}$. The dashed line in the schlieren images is the locus of 50% reaction completion. This line provides an indication of the actual half-reaction length of the wavefront compared with the reference CJ length. The plot scale is the same in both frames.

In the initial phase of corner turning, the foot of the shock lags behind the undisturbed front so that the front near the wall is distinctly curved and not normal to the wall. This overexpansion has been observed in detonation front diffracting around a corner with interior angle 75° or smaller in H_2–O_2 or C_2H_2–O_2 mixtures diluted with Argon (Akbar 1997). The reflection of the shock foot gives rise to a Mach stem and a reflected shock, frame (a). The curved detonation front, created by the interaction with the corner expansion, corresponds to the incident shock, labeled IS in frame (b). Pressure reaches maximum value just behind the triple point (T). This area is marked by the high density of contour lines, which surround a small region above the pressure cutoff value. The reflected shock (RS) is reactive, as indicated by the steep decrease in density behind it in the schlieren image. To the left of RS, the transmitted shock (TS) is curved due to the expansion out of the channel. The contact discontinuity (CD1) between the two waves separates mixtures at different stages of reaction (a larger fraction of products at lower density is found behind the transmitted wave than the incident wave). Two more compression fronts (CW1 and CW2) appear in frame (b), at some distance from the reflected shock and almost parallel to it. These waves, more visible as they cross the contact discontinuity, propagate all the way to the leading shock. There, the rate reaction increase due to the compression is sufficient to generate a small discontinuity in density. This weak contact, labeled CD2, is parallel to the main contact discontinuity.

The wave structure described here is consistent with a mechanism of propagation and amplification of small acoustic disturbances in the reaction zone, followed by shock steepening. For sources emitting at high frequency, compared with the dynamics of the detonation front, Strehlow and Fernandes (1965) showed that any point source located in a planar ZND-CJ reaction zone will propagate a wave containing ray elements that asymptotically lie in a plane parallel to the leading shock, while

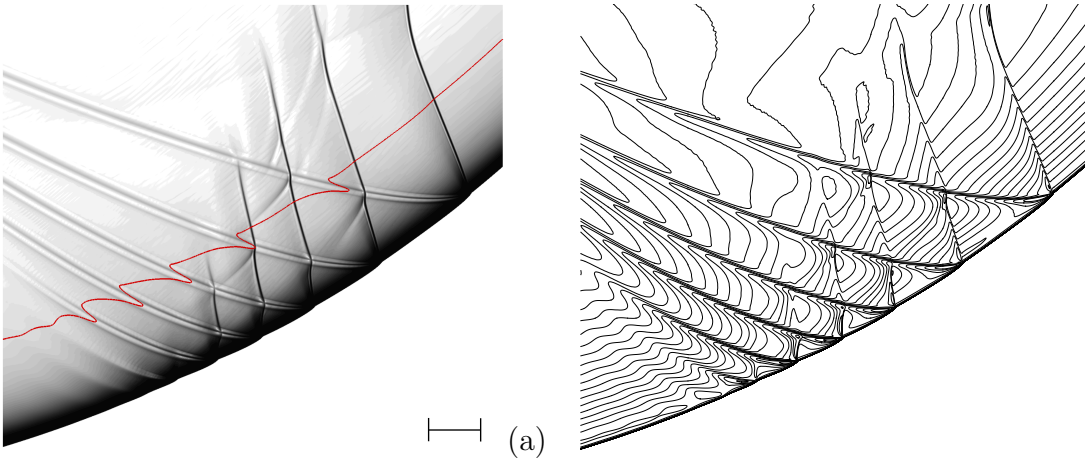

Figure 4.9: Sequence of transverse waves along the detonation front at time $t = 35.79$ for $\theta_{CJ} = 1$. Frame (a): schlieren image. The solid line is the locus of 95% reaction completion. The reference segment (bottom right corner) measures $10\,\Delta_{1/2}$. Frame (b): contours of $c^2 - (7.010 - u_x)^2 - (7.010 - u_y)^2$ from -20 to 15 with spacing equal to 1.

rays that deviate from the plane rapidly wash out of the detonation or reflect from the shock. This plane is located where the sonic parameter, $c^2 - w^2$, reaches a local maximum, and acts as a channel, embedded in the reaction zone, for acoustic disturbances. The energy release, due to chemical reaction, can amplify these disturbances. As the acoustic waves increase in amplitude, shock steepening takes place and the wave spacing increases.

In frame Fig. 4.5 (d), we observe five transverse shocks followed by a train of smaller compression waves. A close up of that same image, Fig. 4.9 (a), shows that the wave spacing is regularly decreasing from the first shock. This spacing can be compared with the reference length $10\,\Delta_{1/2}$, in the bottom corner of the plot. Once formed, each shock generates a new contact discontinuity starting from the detonation front. In turn, the discontinuity provides a local maximum of the sonic parameter, which is shown in frame (b) for the estimated detonation velocity $D_n = 7.010$. As in the planar ZND detonation, this "crest" of the sonic parameter is an acoustic channel for the disturbances, which are amplified and become transverse shocks at the detonation front. A more detailed discussion of this cyclic process of propagation and amplification is postponed to Chapter 6.

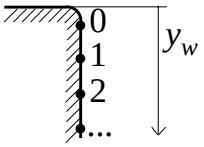

Figure 4.10: Location of injected particles.

4.2.1.1 Particle analysis

We now discuss the results obtained by monitoring the data collected by a selection of particles that were injected along the vertical corner wall, Fig. 4.10. The choice of the initial particle position is motivated by the fact that the most severe reduction of rate reaction is found along that axis, as indicated by the receding 0.95 reaction locus in the first frame of Fig. 4.5.

Particle trajectories are displayed in the space-time diagram of Fig. 4.11. From the temperature profiles, Fig. 4.12, all particles ignite, even when they are very close to the corner. Note that the first particles are accelerated down by the shock and then pulled up into the colder fluid created by the corner vortex. The corresponding temperature decrease takes place when the particles have already ignited and does not significantly affect the heat release process.

Since the shock is normal to the wall, the simplified equation (2.18) for particle analysis can be used. The decomposition of $\mathrm{D}T/\mathrm{D}t$, according to this formula, is performed for particles 1 and 7 and displayed in Fig. 4.13. For each particle, data analysis starts immediately after the passage of the leading shock. The difference between the left-hand side and the right-hand side in (2.18) is due to errors in the evaluation of the terms of the equation. This quantity, which can be larger near the passage of the shock, is plotted as a solid line. For particles 1 and 7, transverse divergence and curvature effects are negligible. In frame (a), the partial time derivatives of pressure and particle velocity are positive, i.e., the unsteady term due to shock acceleration contributes to the increase in the rate of change in particle temperature. In frame (b), the peak in thermicity occurs very quickly after the shock; the effect of unsteadiness is negligible.

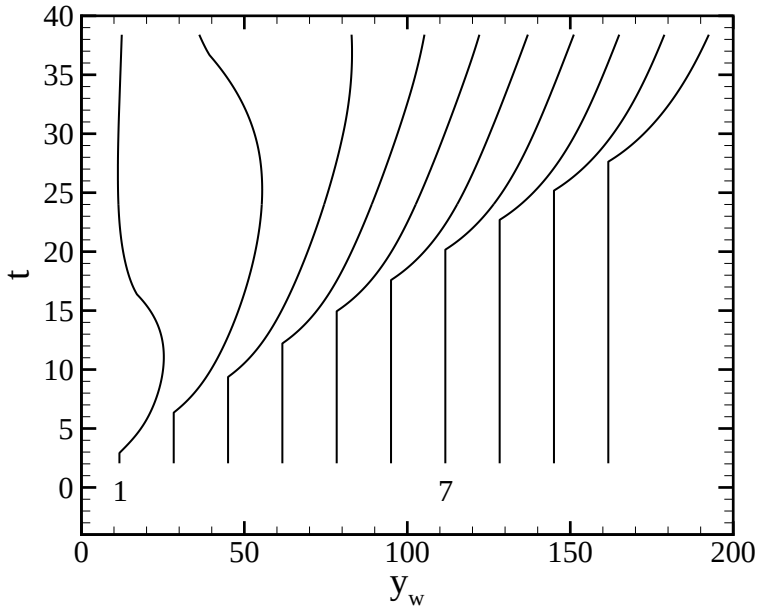

Figure 4.11: Particle paths for 10 sample particles injected along the vertical corner wall for $\theta_{CJ} = 1$. Labels 1 and 7 indicate the particles that are analyzed in terms of numerical dominant balance.

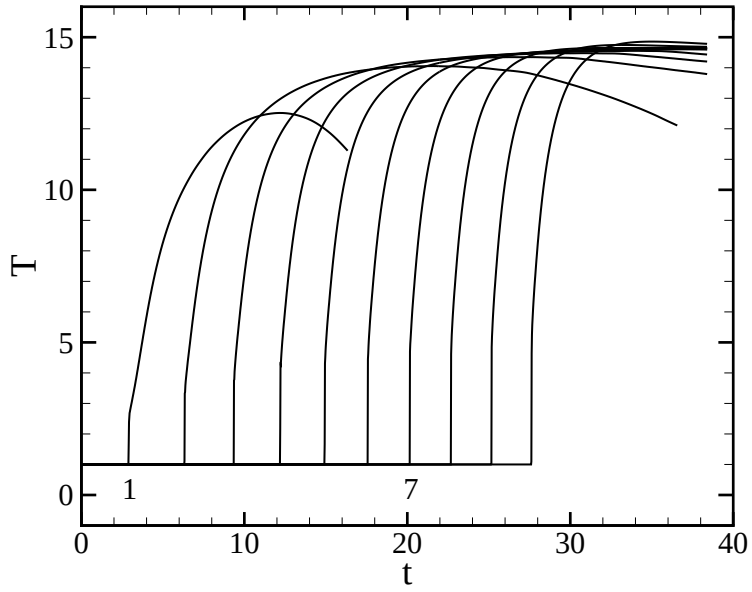

Figure 4.12: Temperature profiles along the particle paths in Fig. 4.11.

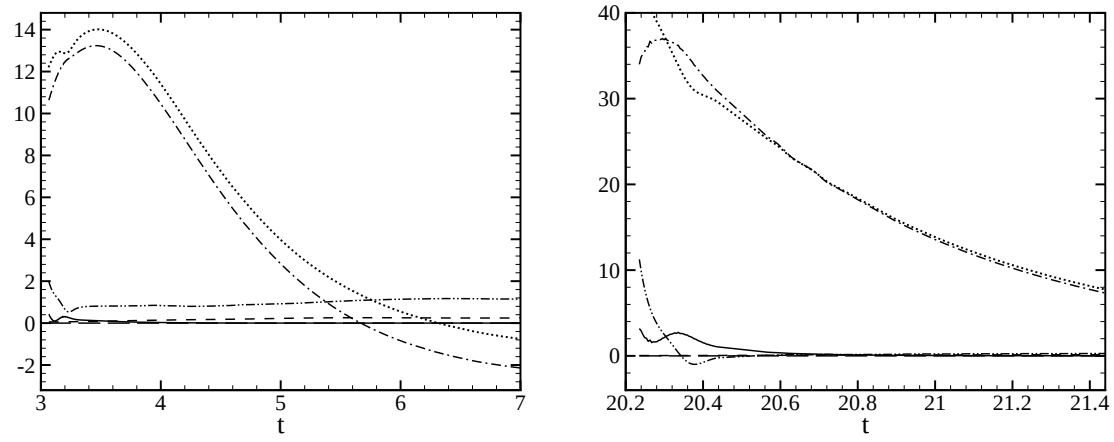

(a) (b)

Figure 4.13: Terms in the reaction zone temperature Equation (2.18) along the same particle paths as in Fig. 4.11 for the case $\theta_{CJ} = 1$. The particles are injected along the vertical wall of the corner. ····· Lagrangian temperature; –·–· heat release; – – – curvature; — — transverse divergence; –··–·· unsteadiness. The solid line is the difference between the left-hand side and the right-hand side in Equation (2.18), as computed from the above terms. (a) Particle 1; (b) Particle 7.

4.2.2 Case $\theta_{CJ} = 4.15$

A sequence of snapshots of the simulation, computed for $\theta_{CJ} = 4.15$, is displayed in Fig. 4.14. The decoupling occurs just behind the head of the corner signal that sweeps across the wave from the corner to the channel axis. The detonation completely fails and there is no local re-ignition, so that the main flow features appear to evolve in time very similar to a non-reacting shock.

Moving along the wavefront from the channel axis, we see that the wave curvature increases up to the point where the no-flow boundary condition, generated by the wall, generates a straight shock perpendicular to it. The transition from curved to straight front is smooth, since the shock is immediately followed by an unsteady expansion wave. This structure is qualitatively predicted by Whitham's geometrical shock dynamics applied to a non-reacting shock diffracting at a sharp corner (Whitham 1974, p. 297). It is also observed by Xu et al. (1997) in a direct numerical simulation computed with $\theta_{CJ} = 3.15$. At the junction of the curved front and the stem adjacent to the wall, the schlieren images in Fig. 4.14 indicate a discontinuous change of density

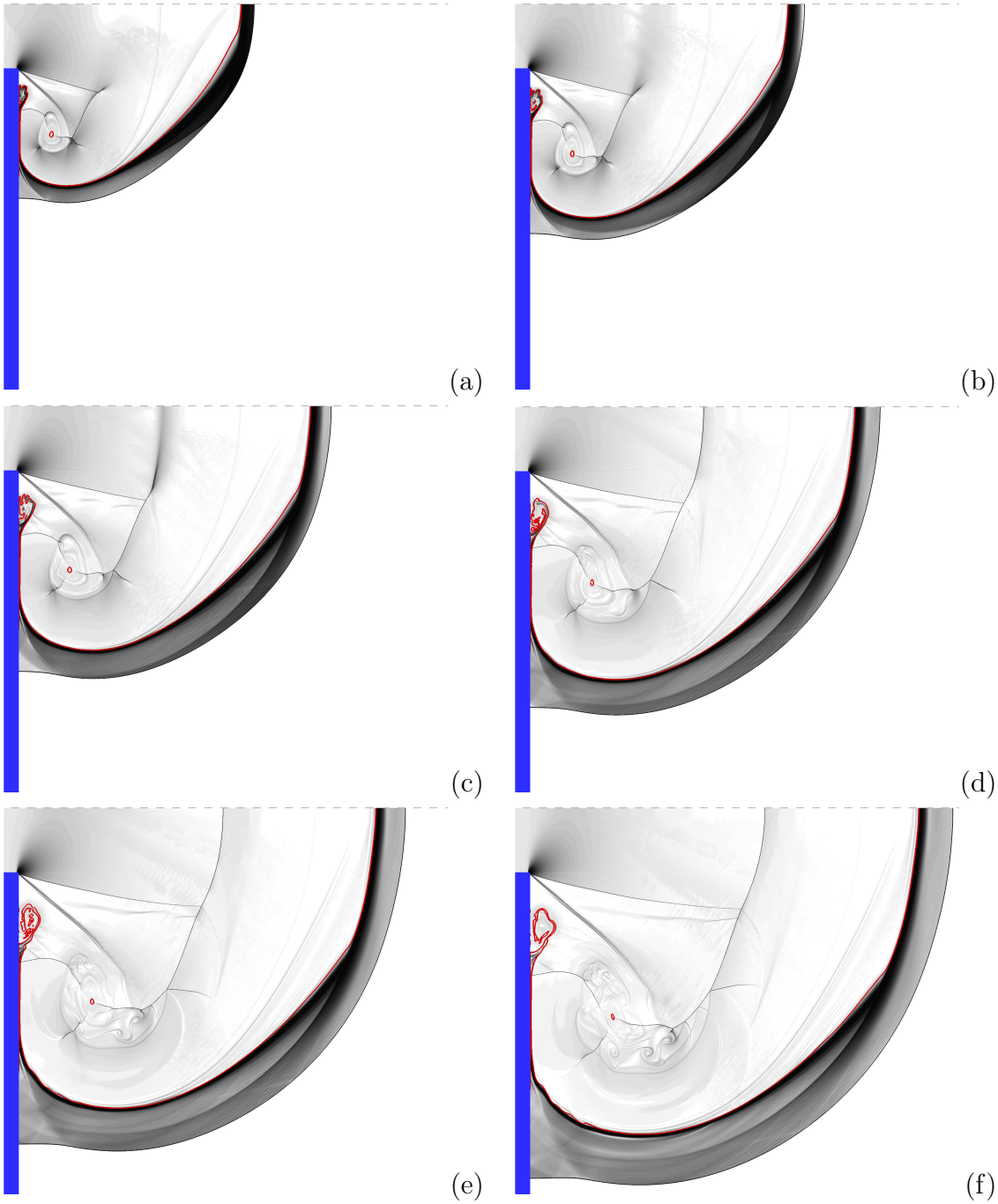

Figure 4.14: Numerical schlieren images for the case $\theta_{CJ} = 4.15$. (a) $t = 22.24$; (b) $t = 28.43$; (c) $t = 34.63$; (d) $t = 40.83$. (e) $t = 47.02$; (f) $t = 53.22$.

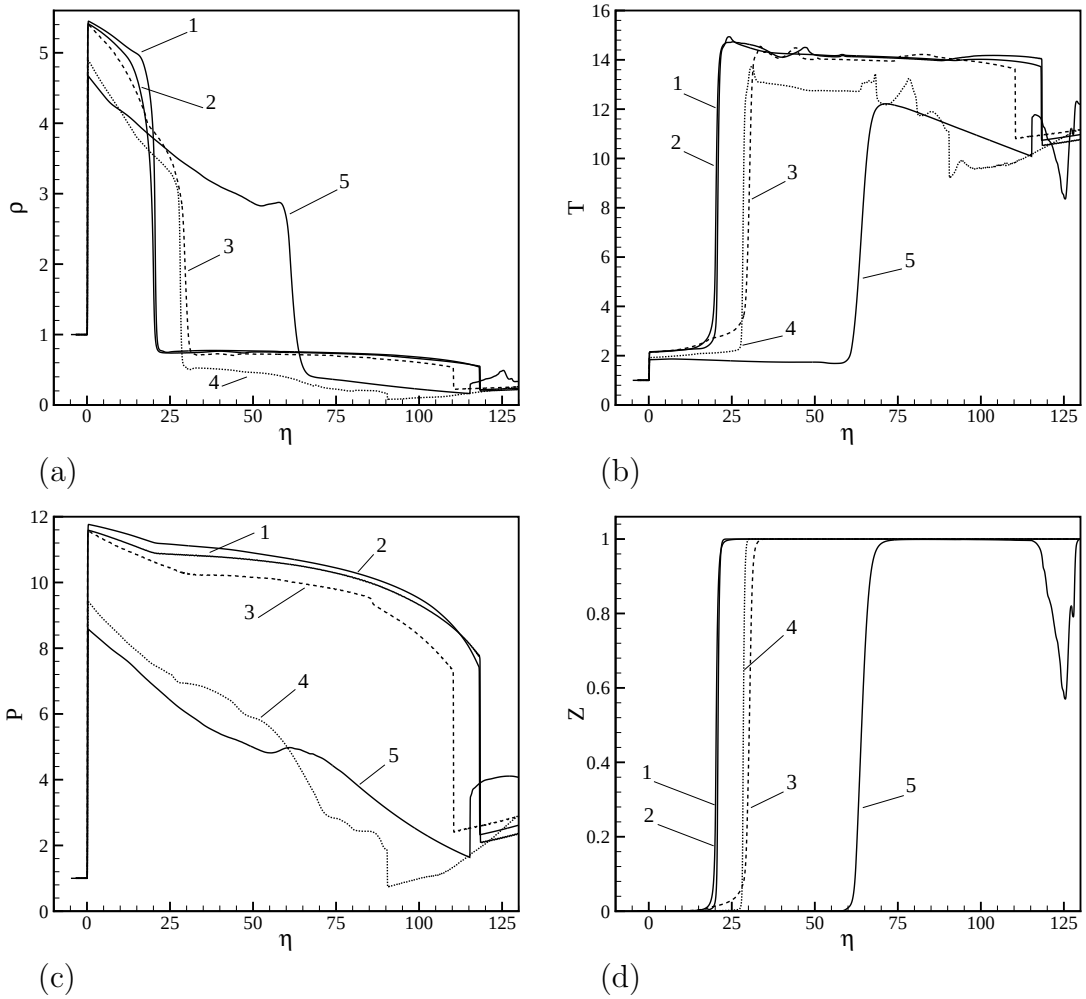

Figure 4.15: Density (a), temperature (b), pressure (c) and progress variable (d) profiles for 5 different data set extracted at $t = 53.22$.

gradient.

The 0.95 reaction locus in Fig. 4.14 marks the separation between the burnt gases, produced before reaction quenching, and the shock-compressed (but unburnt) reactants. This is shown in Fig. 4.15, where density, temperature, pressure and progress variable profiles of 5 slices of the computational domain (at time $t = 53.22$) are plotted. Slices 1 and 5 are extracted along the axis of symmetry and the corner wall, respectively. The remaining data are taken in the shock normal direction and are evenly spaced along the detonation front. Behind the leading shock, temperature and progress variable do not vary substantially from their post-shock values, whereas density and pressure decrease similarly to what would be expected in a blast decay.

Density drops abruptly at a distance of 20 to 30 $\Delta_{1/2}$ from the shock. At the same location, temperature and progress variable rise very rapidly to the corresponding values of the burnt products, while pressure registers only a change of slope. At the wall, this contact discontinuity is located at 60 $\Delta_{1/2}$ behind the Mach stem (Slice 5). A second discontinuity is observed in Fig. 4.15 at a much larger distance from the leading shock. This discontinuity is due to a triple shock system similar to the one described in the super-critical case. This structure is shown in Figure 4.16, where the flow field behind the contact discontinuity CD2 is very similar to the flow shown in Fig. 4.7 for the super-critical case. Here, a third shock (S3) appears between the vortex and the wall; the re-circulation area (C) below CD1 traps a portion of partially reacted gases.

The position of the leading shock, the $Z = 0.05$ and $Z = 0.95$ reaction loci, and the sonic line at the channel axis are plotted in Fig. 4.17. The sonic lines are defined as the loci of points where the flow is sonic in the reference frame traveling at speed D_a. Sonic conditions are reached infinitely far from the shock in the ZND-CJ profile, since the exponent in the depletion law is one. When the head of the corner expansion wave reaches the axis, a sonic point suddenly appears at a finite distance behind the shock. Figure 4.17 shows that this point occurs when the leading shock is still unaffected by the expansion, and that a supersonic region is embedded in the flow for a short time. The fastest trace almost reaches the $Z = 0.05$ line. However, as the axial detonation speed begins decreasing, the flow behind the shock becomes subsonic again in the reference of the shock, and the two sonic lines terminate.

4.2.2.1 Particle analysis

We now discuss the results obtained for a selection of particles injected along the channel axis (Fig. 4.18). This is the most convenient location to probe the flow field, since there the corner expansion is initially the weakest. Particles trajectories, labeled from 1 to 10, are displayed in Fig. 4.19. Comparison with Fig. 4.17 reveals that, at later times, these trajectories are almost parallel to the partial reaction lines. At this point the reaction is quenched, and previously burnt products are separated from

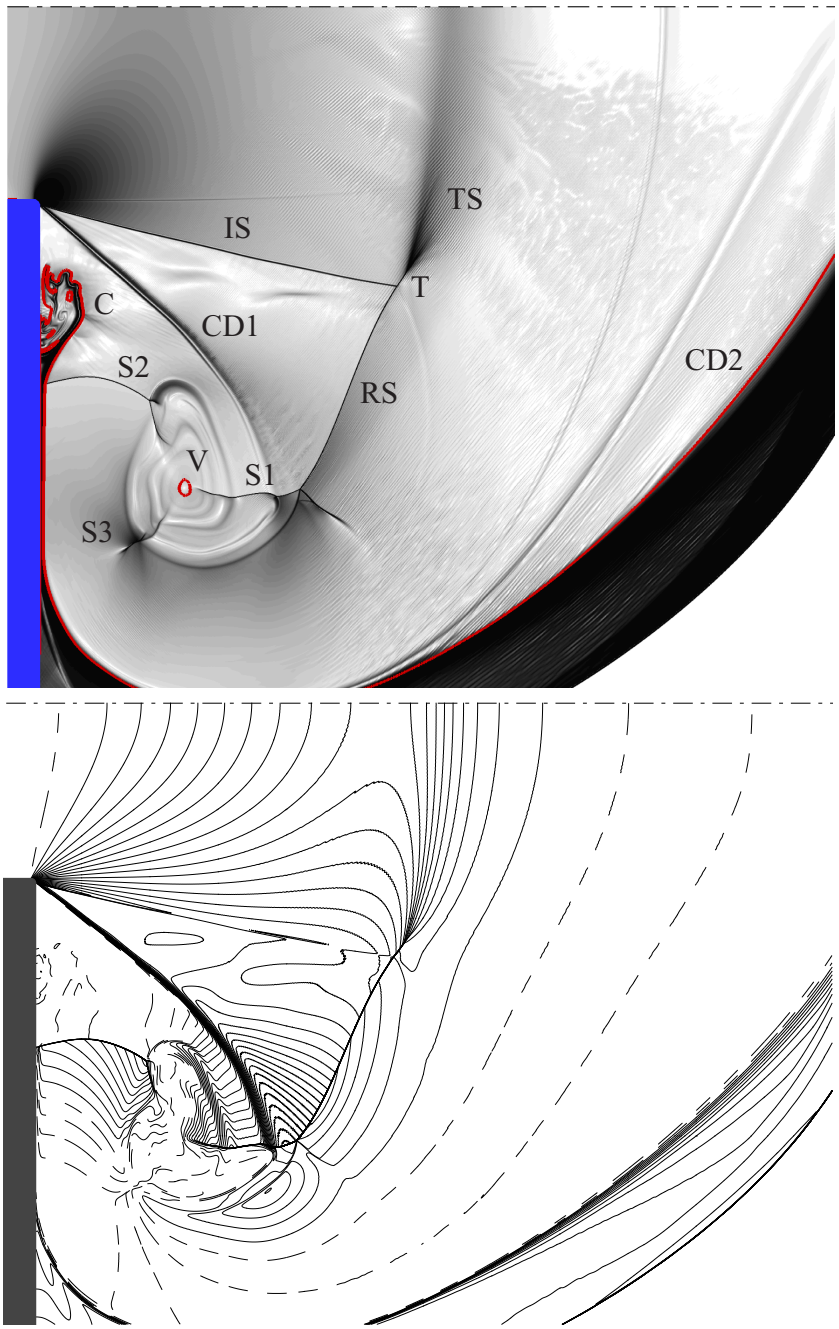

Figure 4.16: Numerical schlieren image, (a), and contours of $u^2/c^2 - 1$, (b). The red line is the 0.95 reaction locus. In (b), the contours have values ranging from -1 to 8, with spacing equal to 0.25. Dashed lines correspond to $u \leq c$ and solid lines to $u > c$. Every dashed contour that is adjacent to a solid contour is a sonic line in the laboratory frame. The plots are a close up of the frame at $t = 28.43$ in Fig. 4.14, computed for $\theta_{CJ} = 4.15$.

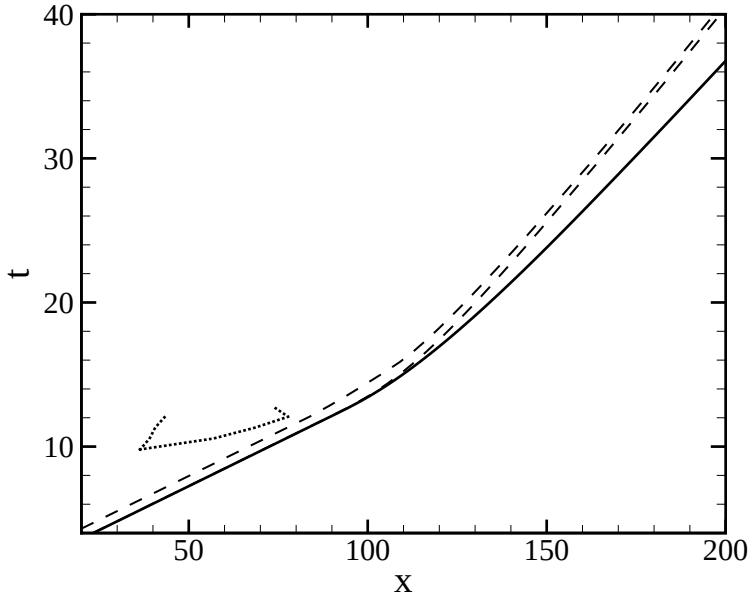

Figure 4.17: Space-time diagram for failing detonation ($\theta_{CJ} = 4.15$). Shock (solid line); sonic loci (dotted line); 0.05 and 0.95 reaction loci (broken line).

fresh mixture by the contact discontinuity observed in Fig. 4.14. The temperature history along these paths is plotted in Fig. 4.20. The increase in reaction zone length with decreasing shock strength is consistent with the reaction rate dependence on temperature.

The decomposition of DT/Dt is performed for particles 1, 3, 5 and 10 and displayed in Fig. 4.21. The plots show that the (positive) transverse divergence term is always small. This justifies treating the flow near the axis as a blast wave with cylindrical symmetry. The curvature term makes a negligible contribution to DT/Dt for particles prior to or at failure. For particles far from failure (particle 1, Fig. 4.21

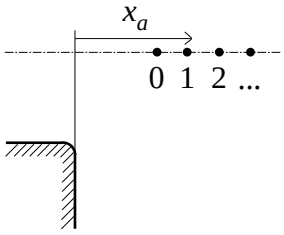

Figure 4.18: Location of injected particles.

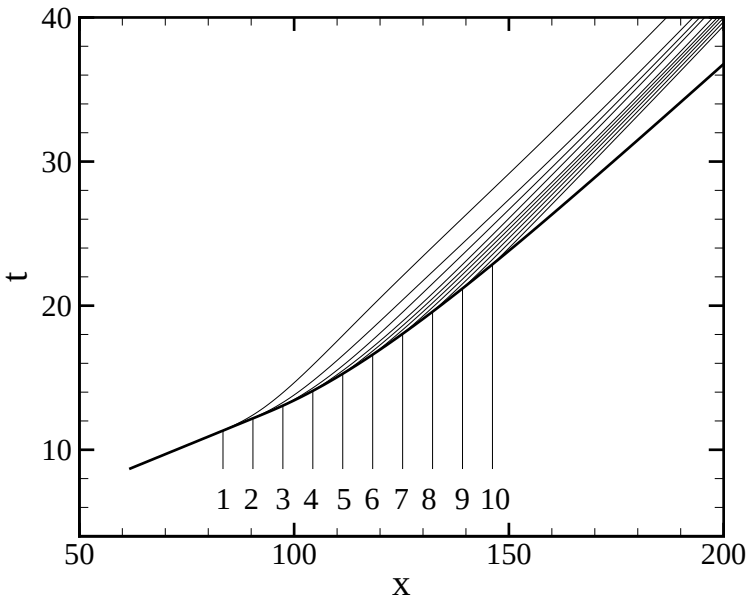

Figure 4.19: Particle paths for ten sample particles. Shock (thick solid line); particle paths (thin solid lines).

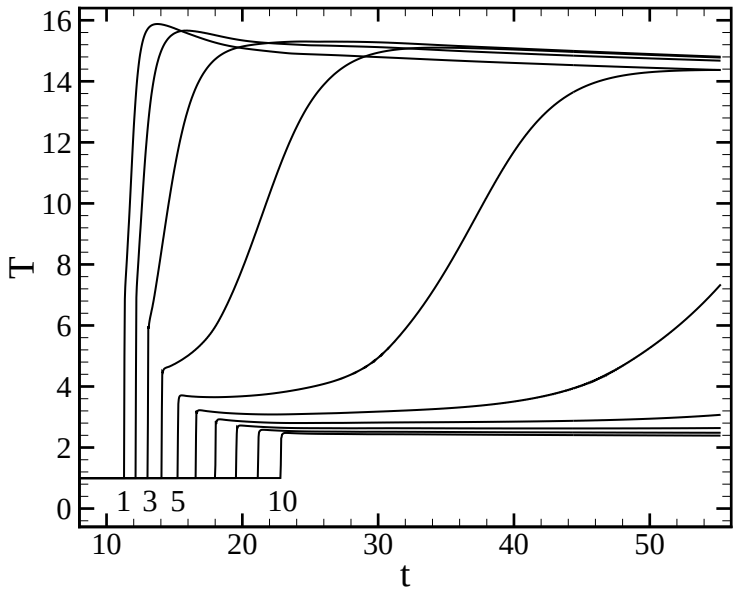

Figure 4.20: Temperature profiles along the particles paths displayed in Fig. 4.19.

(a)), unsteadiness mainly balances curvature and transverse divergence, and the temperature variation is produced by heat release alone. For particles whose rise in temperature is well separated from the initial shock (particles 3 and 5, Fig. 4.21 (b) and (c)), unsteadiness is a negative forcing that reduces $\mathrm{D}T/\mathrm{D}t$ below the value due to heat release. For particle 5, unsteadiness is initially larger than heat release, and the particle temperature decreases below the post-shock value before increasing again. By particle path 10 (Fig. 4.21 (d)), the temperature steadily decreases and unsteadiness dominates over heat release. At this point, the reaction is quenched.

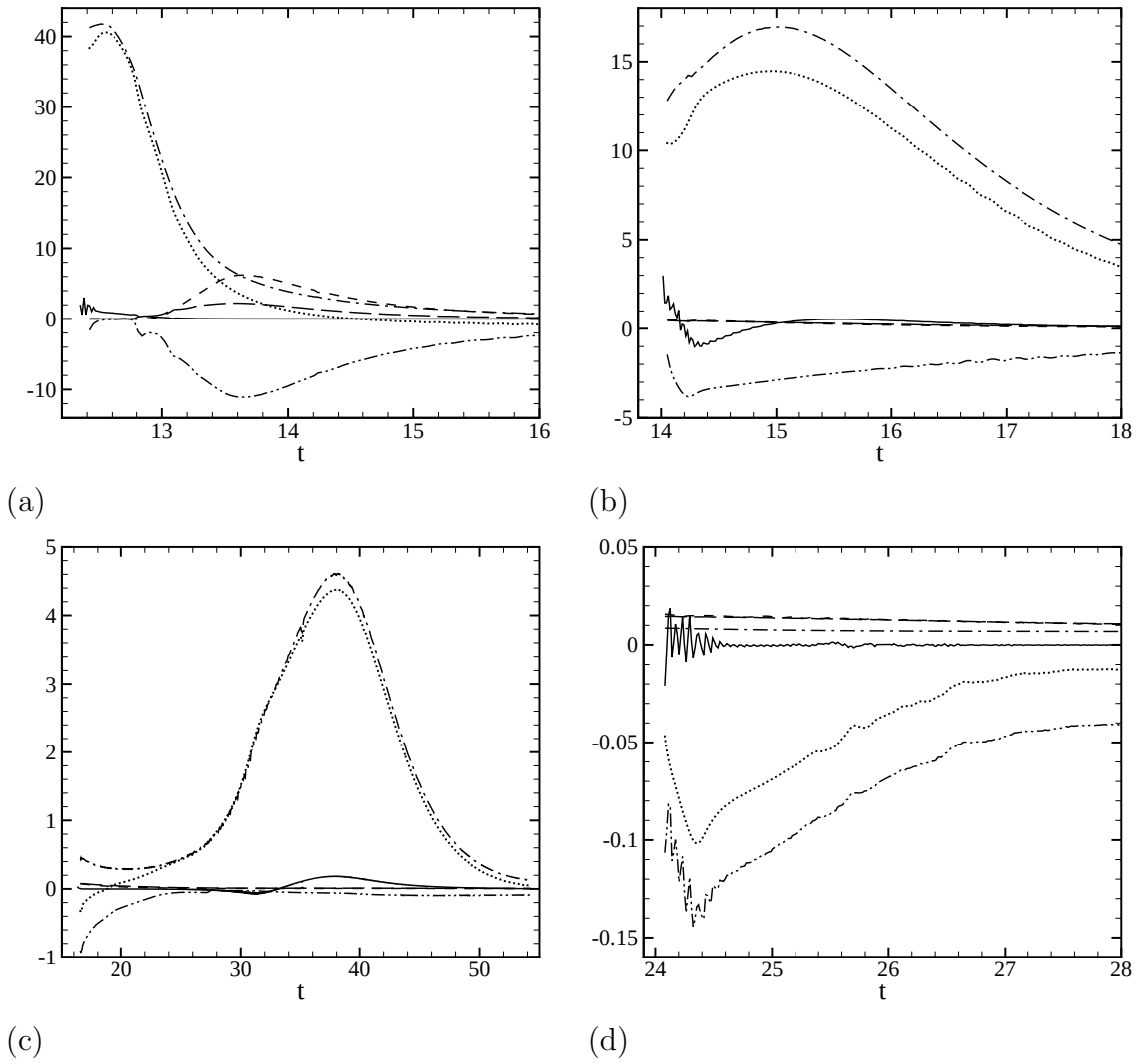

Figure 4.21: Terms in the reaction zone temperature Equation (2.18) along the same particle paths as in Fig. 4.19 for $\theta_{CJ} = 4.15$. The particles are injected on the channel axis of symmetry. $\cdots\cdots$ Lagrangian temperature; $-\cdot-\cdot$ heat release; $- - -$ curvature; $——$ transverse divergence; $-\cdot\cdot-\cdot\cdot$ unsteadiness. The solid line is the difference between the left-hand side and the right-hand side in Equation (2.18), as computed from the above terms. (a) Particle 1; (b) Particle 3; (c) Particle 5; (d) Particle 10.

4.2.3 Case $\theta_{CJ} = 3.5$

This example shows the most interesting behavior of all the cases examined in this study. The detonation begins to fail at the wall, but, at some point, a re-ignition event occurs. Numerical schlieren images (Figs 4.22 and 4.23) for the case $\theta_{CJ} = 3.5$ indicate how complex are the dynamics of the diffraction process. As shown by Figs 4.2 and 4.3, the front evolves differently along the axis of symmetry and the wall. At the channel axis, the shock appears to never completely decouple from the reaction zone. The detonation speed exhibits a plateau at a speed of about $0.6\,D_{CJ}$, but then climbs toward the CJ value. Conversely, the shock at the corner wall immediately detaches from the reaction zone and maintains a speed of about $0.4\,D_{CJ}$ until the arrival of a transverse wave. At this point, re-ignition takes place through the spontaneous creation of a transverse wave.

In the following, we closely examine the mechanism of formation of the first transverse wave, shown in the frames of Fig. 4.22. Figure 4.24 is a sequence of pressure contours and numerical schlieren images at the axis of symmetry for a small region of flow behind the main shock. In addition to the expansion fronts, the numerical schlieren images (right) show two additional features. The first is an almost vertical "blip" in density (BL) that can be explained as a residual of a transverse disturbance triggered by the passage of the leading shock by the corner. The second originates at the end of the main reaction zone and lies near the 0.95 reaction locus. It can be interpreted as a slope discontinuity in density (SD) between partially burnt and completely burnt products. These two features are too weak to register in the corresponding contours of pressure and are not considered relevant for the overall dynamics.

The rarefaction originating at the corner (IR) reflects at the axis of symmetry, and a new, semi-circular rarefaction front (RR) can be seen in Fig. 4.24 (a), still outside the main reaction zone. In that same frame, the head of the expansion has crossed the 0.95 reaction locus, but it has not reached the shock front at the axis, which is therefore still straight. By time $t = 11.08$, the reflected expansion has reached the

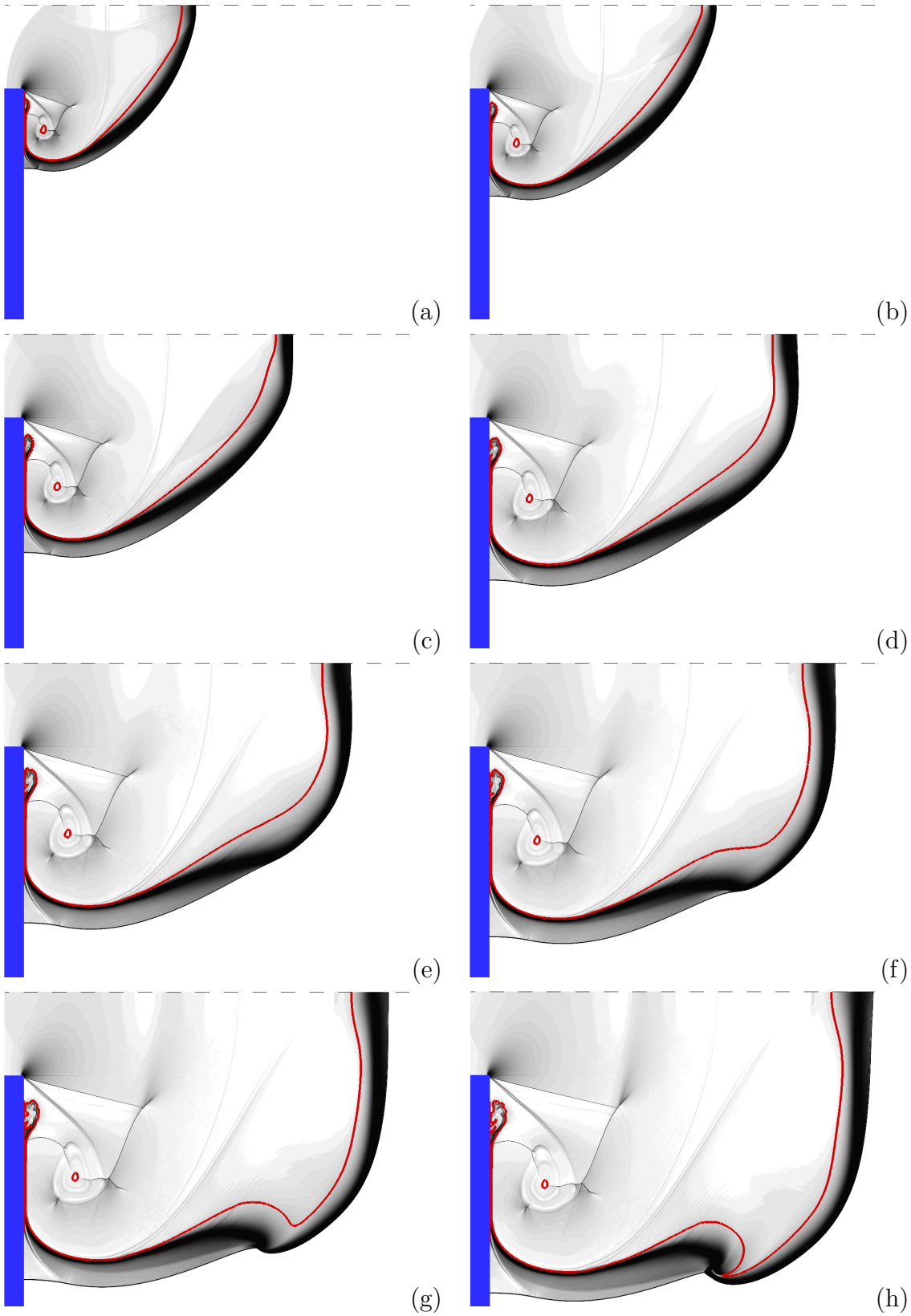

Figure 4.22: Numerical schlieren images for the case $\theta_{CJ} = 3.5$. (a) $t = 10.17$; (b) $t = 13.83$; (c) $t = 17.49$; (d) $t = 21.15$. (e) $t = 22.98$; (f) $t = 24.81$; (g) $t = 26.64$; (h) $t = 28.47$.

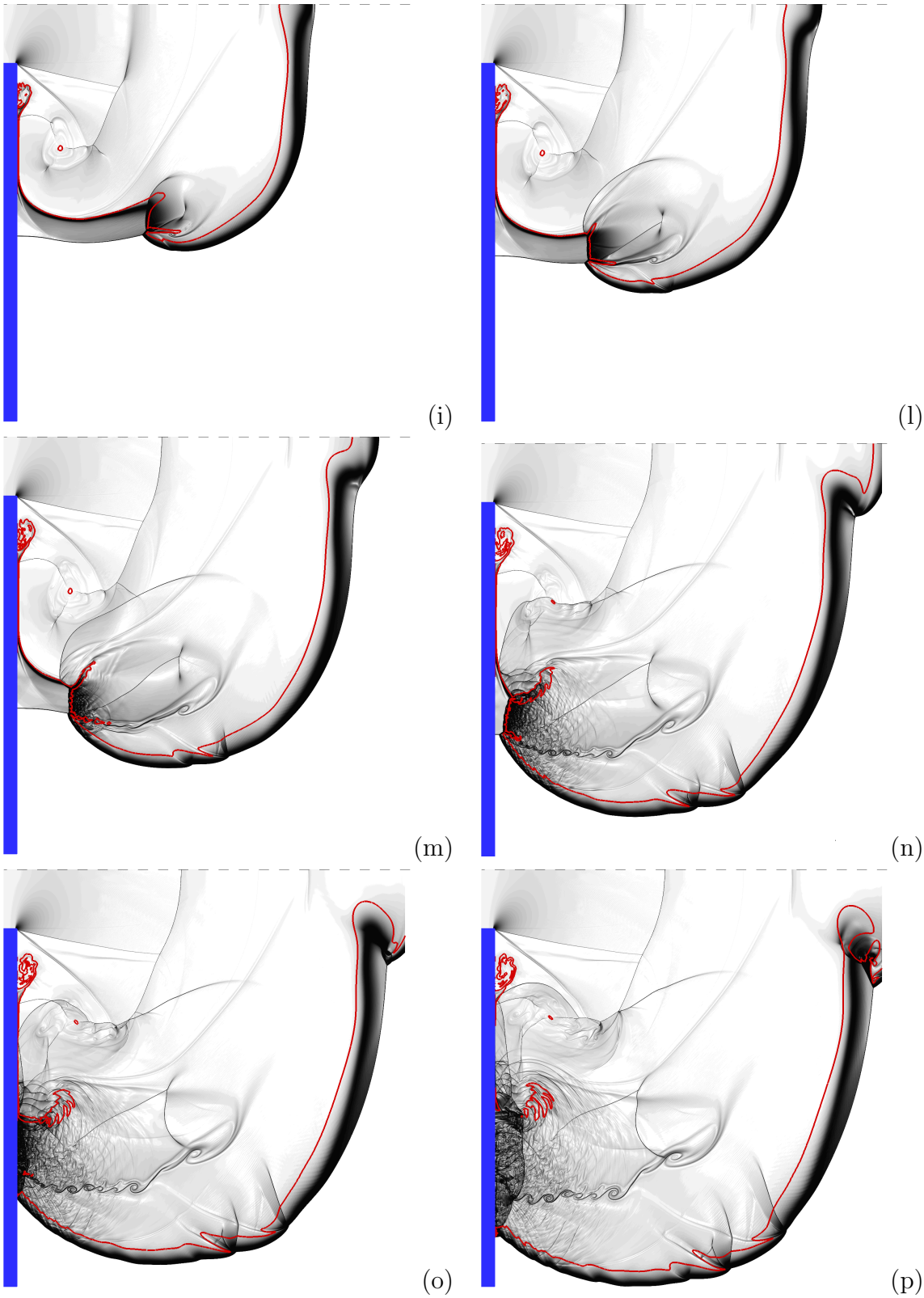

Figure 4.23: Numerical schlieren images for the case $\theta_{CJ} = 3.5$. (i) $t = 32.13$; (l) $t = 35.79$; (m) $t = 39.45$; (n) $t = 43.11$. (o) $t = 44.94$; (p) $t = 46.77$.

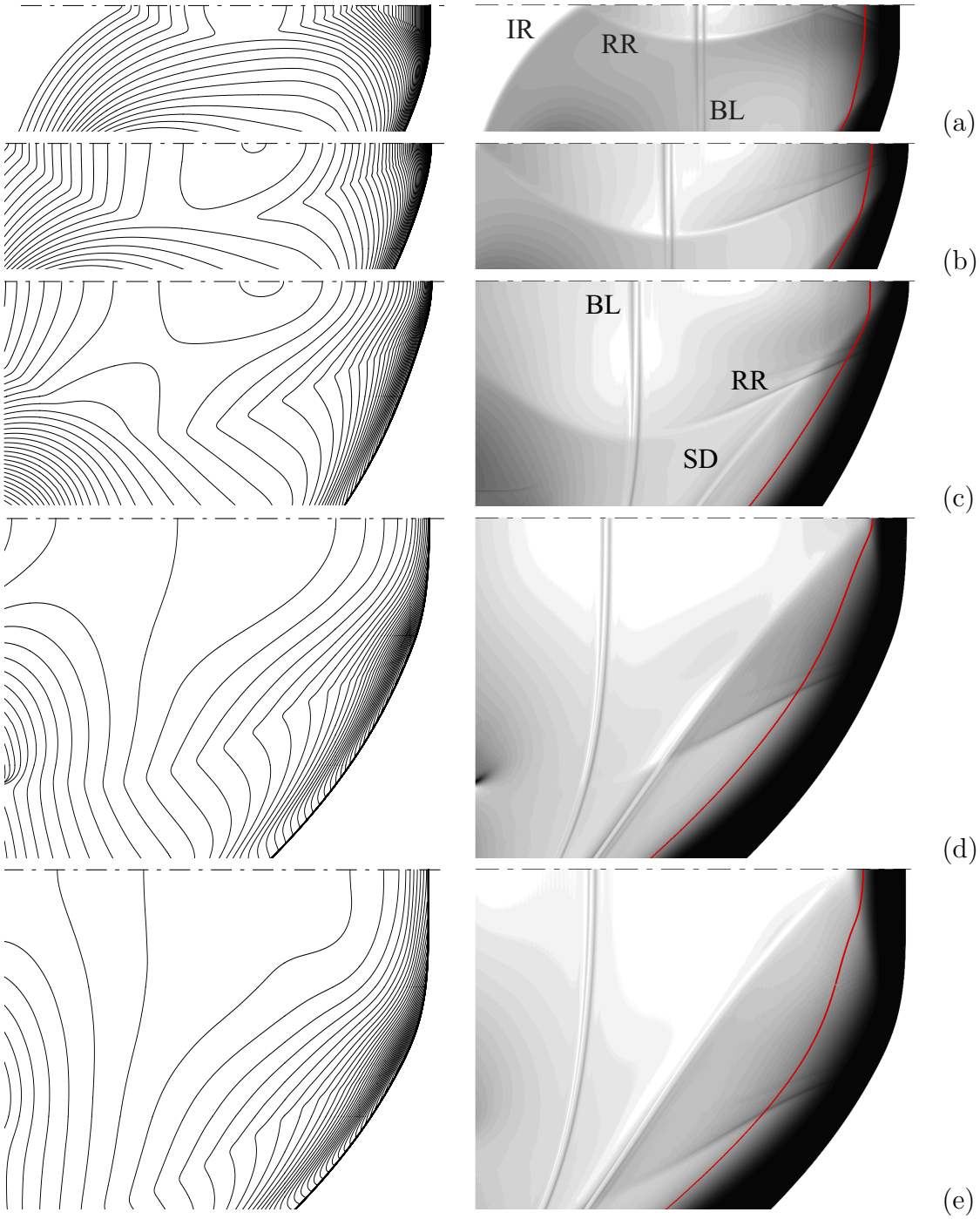

Figure 4.24: Pressure contours (left) and numerical schlieren images (right) for the case $\theta_{CJ} = 3.5$ at times $t = 9.255$ (a); 11.08 (b); 12.91 (c); 15.66 (d); 17.49 (e). Each plot measures 86.7 half-reaction lengths in width.

main reaction zone and sweeps downwards along the detonation front. This further reduces the strength of the leading shock and results in a flattening of the front near the axis. The 0.95 locus appears to get closer to the shock, since fresh, partially reacted gas is now moving along the axis of symmetry more slowly than previously processed fluid. In this situation, an observer, moving from the axis of symmetry to the corner wall along the wavefront, would find the maximum value of pressure at the leading shock immediately ahead of the reflected expansion front. This can be seen in the pressure plots of Fig. 4.24, where the highest density of iso-lines is located near the intersection of the reflected rarefaction with the shock. As the observer moves beyond that peak toward the corner wall, the pressure decreases again, this time because of the effect of the first corner expansion. Correspondingly, the contours of pressure become more sparse behind the shock. Before reaching the wall, the reaction zone gives way to a non-reactive shock followed by a contact discontinuity that separates unreacted but compressed gas from convected products, a situation already found in the previous sub-critical case. The partially coupled detonation front is the basis for the subsequent flow evolution that results in re-ignition of the detonation.

By time $t = 17.49$, the reflected expansion appears to have lost most of its strength (Fig. 4.24 (e)), and, near the wavefront pressure peak, the end reaction zone begins to approach the shock and cause it to accelerate. At time $t = 21.15$ (Fig. 4.22), the wavefront has acquired a very peculiar shape. It is almost flat at the axis of symmetry, has a relatively large curvature in the center, and is completely decoupled at the wall. A fold or kink in the shock front can be observed at time $t = 26.64$. By the next frame, a transverse shock wave has formed from this fold and is propagating toward the corner wall. The frames of Fig. 4.23 display this further evolution, up to the reflection of the transverse wave at the corner wall.

The detailed structure of the transverse wave is of interest. Similar waves have been observed in the formation of cellular structures in recent simulations (see Sharpe 2001; Inaba and Matsuo 2001). The second triple point (T2) in Fig. 4.25, in addition to the triple point on the leading front (T1), identifies this configuration as a transverse wave of *strong* type (Fickett and Davis 1979). This configuration is typically

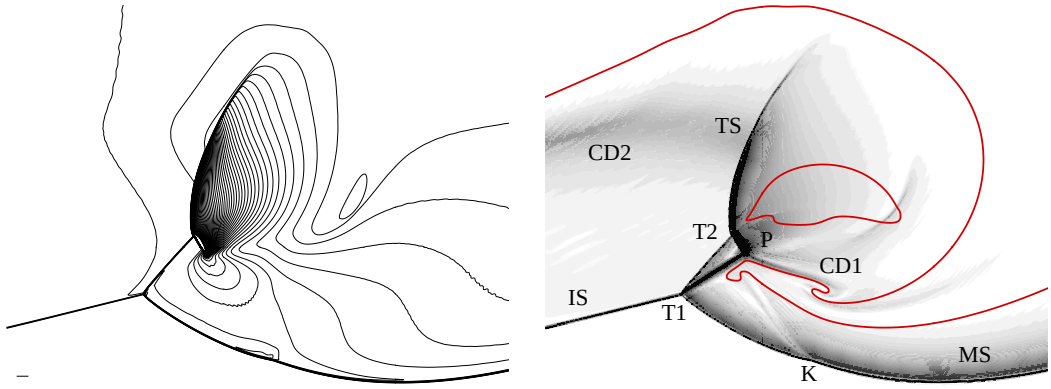

(a) (b)

Figure 4.25: Structure of transverse wave, contours of pressure, (a), and numerical schlieren images of density, (b). The solid line in (b) is the 0.95 reaction locus. In (a), contour lines are spaced by the non-dimensional value 2.083. A cutoff value of 250 is used (the local maximum value is 445), to mark the pressure peak position behind the kink. The segment at the bottom left indicates the length of $\Delta_{1/2}$ in the plot scale. The two images are a close up of a frame at $t = 30.30$ computed for $\theta_{CJ} = 3.5$.

associated with fully developed detonation cells and moderate to large heat release. It is interesting to contrast the formation of this structure in a near-critical diffraction with the appearance of a train of transverse waves of the weak type in a fully coupled detonation (Fig. 4.9).

In the wave system shown in Fig. 4.25 (b), the incident shock (IS) is essentially non-reactive, while the curved Mach stem (MS) has a much higher reaction rate. This can be seen by considering the distance of the 95% reaction locus from the shock front. A contact discontinuity (CD2) separates the partially reacted gas, processed by IS, from the completely burnt products. The transverse wave (TS) extends between the two triple points, T1 and T2, as a straight shock, and from T2 to the 95% reaction locus as a curved, strongly reactive wave. It propagates into the partially reacted region behind the incident shock and quickly brings the reaction to completion. The maximum value of reactivity is found immediately behind the short stem connecting point P with T2. In frame (a), this small area is above the cutoff value of the pressure contours, and it is surrounded by the highest density of contour lines. The contact discontinuity CD1 separates the gas that has passed through MS from the gas processed by the transverse shock. A relatively minor feature, a kink (K) in the

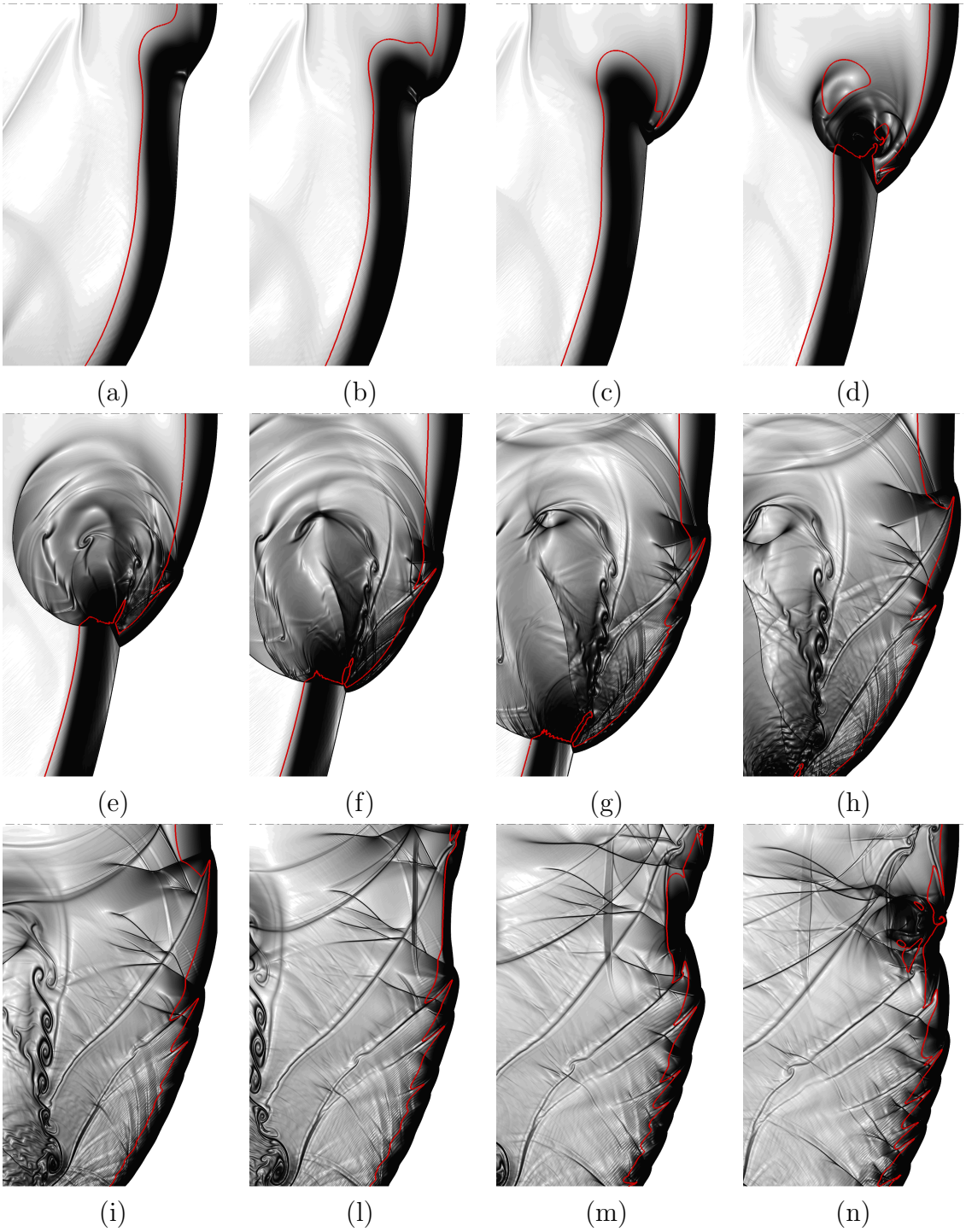

Figure 4.26: Numerical schlieren images for the case $\theta_{CJ} = 3.5$. Each frame is a close up of the computational domain, near the leading shock, at the channel axis of symmetry. The sequence goes from time $t = 39.45$ to $t = 69.65$ by increments of 2.745. Each plot measures 153.3 half-reaction zone reference lengths in height.

Mach stem, is also visible. The discontinuity associated with the kink terminates near point P. Grid resolution studies by Sharpe (2001) indicate that this feature rapidly disappears in underresolved simulations, so its presence in the result we are showing here suggests that the level of resolution could be adequate (see also the convergence study performed on this wave structure in Appendix C).

Returning to Fig. 4.23, a second shock folding can be seen to take place after time $t = 35.79$ near the channel axis. Since this evolution occurs near the end of the original computational domain, it was found convenient to stop the simulation and translate the flow solution to the left before restarting the computation. In this way, the inlet channel (most of it not shown in the previous images) moves out from the computational domain, leaving (on the right) a newly available strip of domain slightly less than 1500 cells wide. This operation has the purpose of "freeing" a few processors, at the expense of the correct inlet boundary conditions on the left-hand side of the domain. The "new" region is then populated with values of the undisturbed flow ahead of the detonation, and the computation is restarted from this point. Until the waves from the rear of the domain reach the front, the computation of the region near the wavefront will be unaffected. With some caution, this operation can be repeated a few times to study the wave evolution near the axis of symmetry.

The application of this technique allows us to follow the wavefront evolution for a longer time, and we show these results in a sequence of schlieren images in Fig. 4.26. These 12 snapshots are a close up of the solution near the leading shock at the axis of symmetry. Each image measures 153.3 half-reaction zone lengths in height.

Examining Fig. 4.26, we see that, as before, the acceleration of a portion of the front generates a shock fold and eventually a shock-shock interaction (frame (a) to (c)), followed by an increased rate of reaction, and an almost cylindrical explosion (frame (d) to (e)) at the end of the main reaction zone. By frame (f), this secondary front has reached the axis of symmetry, where it starts to reflect. At frame (i), only a small section of the original wavefront, in the upper part of our field of view, has not been covered by an overlapping system of transverse waves. The closeness of the 0.95 reaction locus to the leading shock, and its irregular shape, indicate that this

corrugated wavefront has an enhanced net reaction rate over the originally smooth front. The remaining frames of Fig. 4.26 show the reflection of the newly formed waves at the axis of symmetry. Interestingly, the lower portion of frame (n) suggests a certain regularity in the spacing of the transverse waves, reminiscent of propagating detonations with cellular instability.

We conclude this section by observing that for slightly larger activation energies ($\theta_{CJ} = 3.75$ and $\theta_{CJ} = 4$), the mechanism described above also produces a first transverse wave analogous to the one in Fig. 4.25. This wave is slower and weaker than the one we show here, but still completely formed. However, no acceleration of the front at the axis of symmetry can be observed in Fig. 4.2. In these cases we observe a monotone decay of D_a, and there are no features like those seen in Fig. 4.26. We conclude that acceleration of the shock close to the channel axis is the distinctive feature that sets apart a failing, near-critical detonation diffraction (for $\theta_{CJ} = 3.75$), from a successful one (for $\theta_{CJ} = 3.5$).

4.2.3.1 Particle analysis

From the previous description, two radically different behaviors can be identified in the two regions near the channel axis and the corner wall. At the wall, the decoupling of the shock from the reaction zone persists until an external cause, the reflection of a strong transverse shock, is able to re-ignite the mixture. At the channel axis, a complex wave-front dynamic results in shock folding, and eventually produces an explosion, followed by a system of transverse waves. In both cases, there is symmetry with respect to channel axis, and the simplified Equation (2.18) for the Lagrangian temperature derivative can be used.

We first contrast the space-time diagram for the leading shock and the 0.05 and 0.95 reaction loci along the two directions. Along the axis of symmetry (Fig. 4.27), at the arrival of the expansion, the shock speed decreases, and a small delay forms between the shock and the 0.05 locus. Accordingly, the thickness of the reaction zone increases, and the distance between the two reaction loci grows almost linearly in time. After $x_a = 200$ the shock accelerates, the ignition delay disappears and

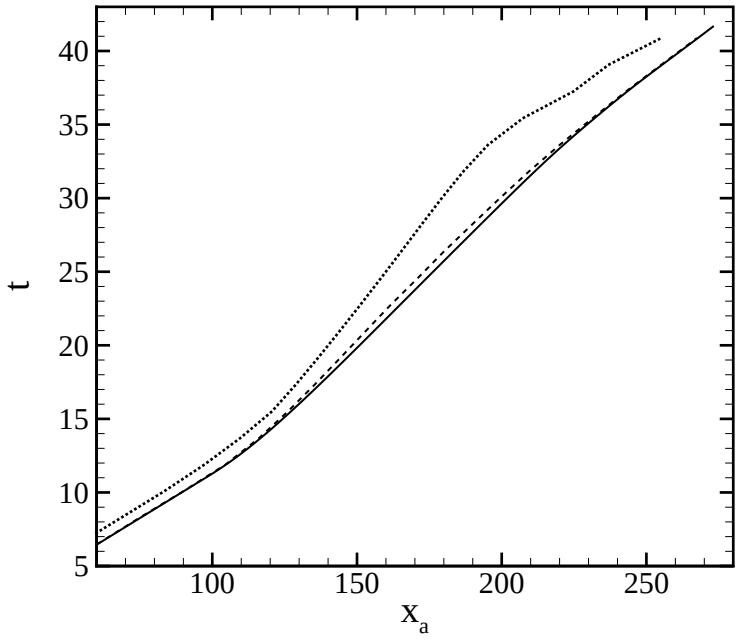

Figure 4.27: Space-time diagram for the leading shock and the 0.05 and 0.95 reaction loci along the axis of symmetry. Solid line leading shock; – – – progress variable 0.05; · · · · · · progress variable 0.95.

the reaction length starts decreasing, all indications that the detonation has locally overcome the effects of the corner expansion.

Along the corner wall (Fig. 4.28), the picture is quite different. The 0.95 reaction locus is almost stationary until $t = 10$, indicating that a portion of the flow does not completely react due to the large drop in pressure and density. Figure 4.22 shows a portion of partially unburnt material being shed from the corner and then advected downward. Likewise, the 0.05 reaction locus translates at the post-shock particle velocity. The growing gap between partially reacted material and the leading shock indicates a complete local quenching of the reaction. By $t = 43$, a transverse wave reflects from the wall, and the temperature of the unburnt gas increases due to the strength of the reflected shock. The pockets of unreacted material are rapidly consumed, as demonstrated by the disappearance of the initial 0.05 reaction locus at $t = 44$ and by the formation of two 0.95 loci at $y_w = 90$. The leading shock rapidly accelerates and it is now strongly coupled to a newly formed reaction zone.

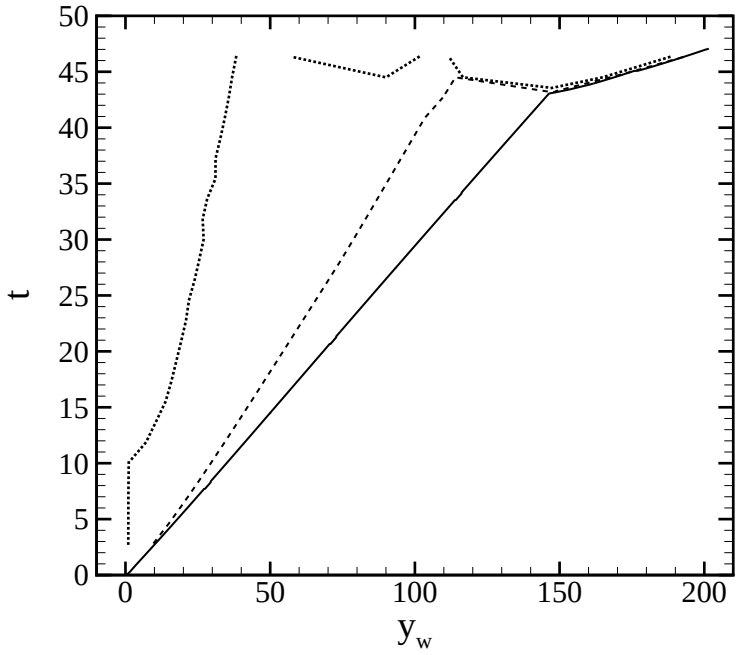

Figure 4.28: Space-time diagram for the leading shock and the 0.05 and 0.95 reaction loci along the wall. Solid line leading shock; − − − progress variable 0.05; · · · · · · progress variable 0.95.

Lagrangian trajectories are displayed in Fig. 4.29 and Fig. 4.30 for particles that are located on the axis of symmetry and on the wall. The temperature readings along these paths are displayed in Fig. 4.31 and Fig. 4.32, respectively. Labels indicate particles that will be further analyzed in this section.

In particles moving along the channel axis (Fig. 4.31), the post-shock temperature decreases, reaches a minimum, and then increases again. Likewise, the time delay between the shock passage and the peak temperature for particle 10 is larger by about an order of magnitude than the corresponding time for particle 1, indicating a growth in ignition time. From particle 10 to 21 the ignition time decreases again. This variation is consistent with the change of slope exhibited by the leading shock in the $x - t$ diagram of Fig. 4.27. These results indicate that the detonation slows down, but does not fail. Interestingly, the post-shock slopes of the temperature never become negative for any of the trajectories shown in Fig. 4.31.

In particles moving along the corner wall (Fig. 4.32), no ignition occurs until

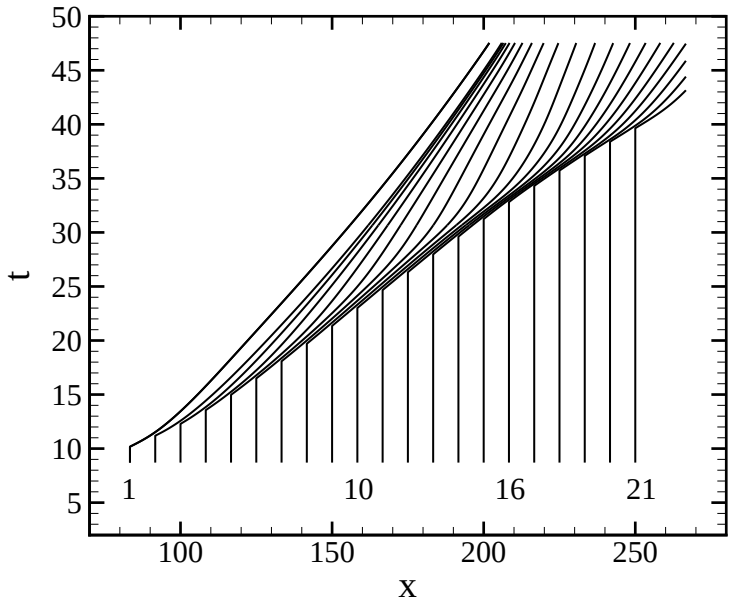

Figure 4.29: Particle paths for 21 sample particles injected along the channel axis (Fig. 4.18) for $\theta_{CJ} = 3.5$. The labels 1, 10, 16, 21 indicate particles that are analyzed in terms of numerical dominant balance.

$t = 43$, the time of arrival of the transverse wave. The post-shock temperature steadily decays from particle 1 to particle 7, has a slight increment from particle 7 to 12, and then decreases again. Overall, the flow in this time interval can be treated as non-reacting until the arrival of the transverse wave.

We now examine the terms in the reaction zone temperature Equation (2.18) along the same paths as in Fig. 4.29 (axis of symmetry) for particles 1, 10, 16, 21. The plots in Fig. 4.21 (a) and Fig. 4.33 (a), for particles initially located just downstream of the head disturbance arrival point, are virtually identical. This is expected, since the activation energies in these two cases differ by a relatively small amount and the perturbation due to the corner is the same. However, the behavior of the particles that follow is radically different. Whereas particles 10 and 16 have much longer ignition times, of the order of 5–10, particles located further downstream display again an ignition time of the order of unity. This reinforces that in the case $\theta_{CJ} = 3.5$ the detonation recouples at the axis, contrary to the case $\theta = 4.15$.

If we now examine one by one the terms appearing on the right-hand side of

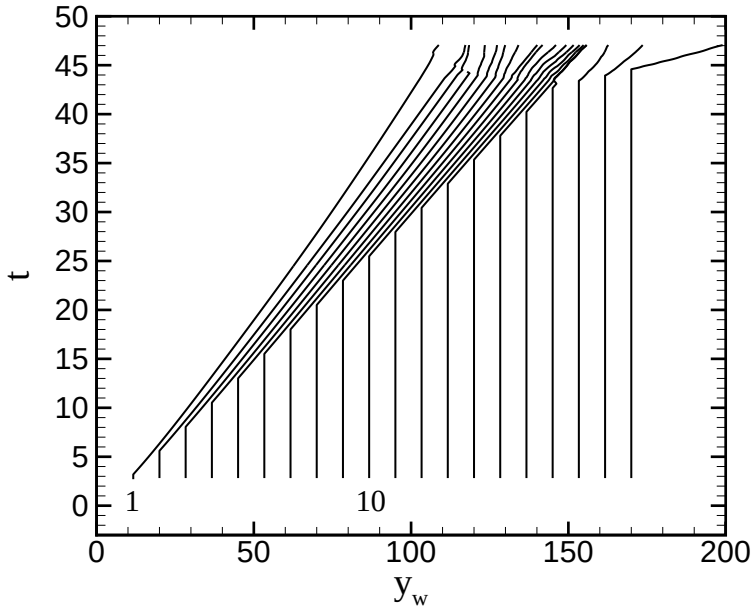

Figure 4.30: Particle paths for 20 sample particles injected along the vertical corner wall (Fig. 4.10) for $\theta_{CJ} = 3.5$. The labels 1 and 10 indicate the particles that are analyzed in terms of numerical dominant balance.

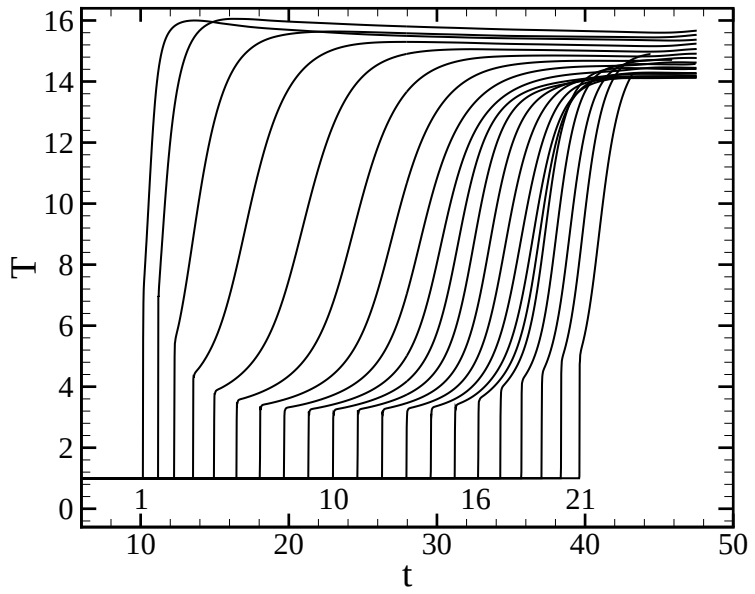

Figure 4.31: Temperature profiles along the particle paths displayed in Fig. 4.29.

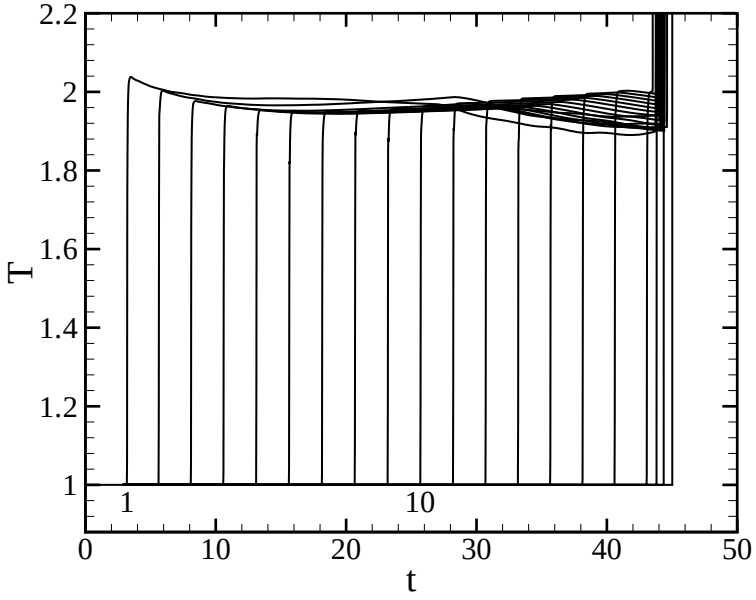

Figure 4.32: Temperature profiles along particles paths displayed in Fig. 4.30.

Equation (2.18), we notice that the unsteady term appears almost everywhere in the form of a negative forcing, as for the case $\theta_{CJ} = 4.15$. There is only one exception in Fig. 4.33 (c), where unsteadiness provides a small increment to the peak value of $\mathrm{D}T/\mathrm{D}t$. Overall, curvature and divergence effects play a relatively unimportant role in determining the Lagrangian derivative of temperature. Exception to this are the paths 10 and 16 (Fig. 4.33 (b) and (c)), where a strong peak in the curvature term can be observed at time $t \cong 40$. At this point however, the flow has already reacted, and $\mathrm{D}T/\mathrm{D}t$ is almost zero.

To conclude, we analyze two representative Lagrangian paths along the corner wall. Figure 4.34 (a) is very similar to Fig. 4.21 (d), with the evolution of temperature dictated by the unsteady term. Figure 4.34 (b) captures the small change in $\mathrm{D}T/\mathrm{D}t$ that is registered by particles 1 to 10 in Fig. 4.32. Variations in temperature are three orders of magnitude smaller than the ones observed by the particles moving along the axis of symmetry, and data analysis is affected by a large amount of noise. Even in this case however, the change in $\mathrm{D}T/\mathrm{D}t$ corresponds to a variation in the unsteady term, while transverse divergence, curvature and heat release remain almost constant.

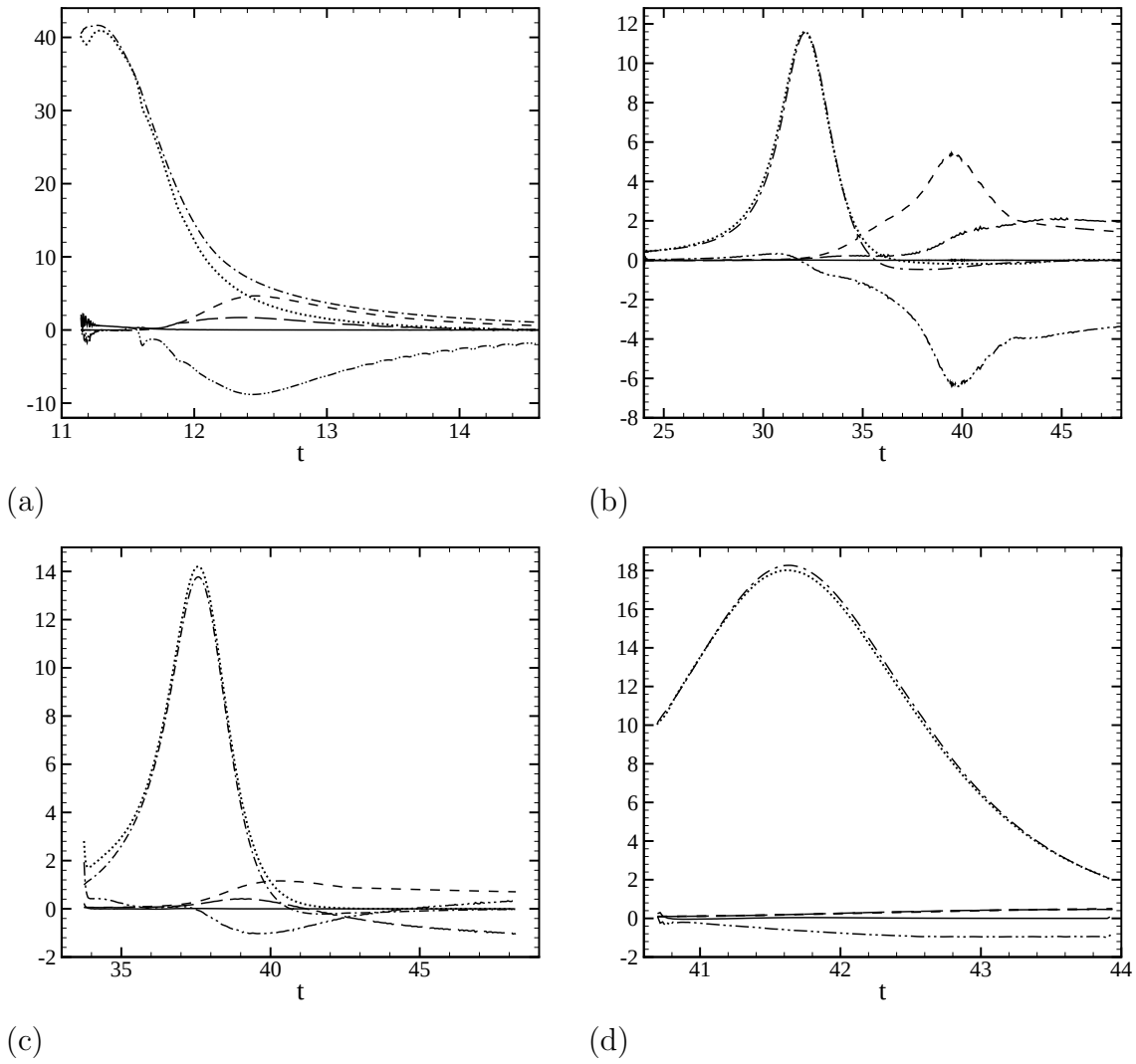

Figure 4.33: Terms in the reaction zone temperature Equation (2.18) along the same particle paths as in Fig. 4.29 for the case $\theta_{CJ} = 3.5$. The particles are injected along the axis of symmetry. $\cdots\cdots$ Lagrangian temperature; $-\cdot-\cdot$ heat release; $---$ curvature; —— transverse divergence; $-\cdot\cdot-\cdot\cdot$ unsteadiness. The solid line is the difference between the left-hand side and the right-hand side in Equation (2.18), as computed from the above terms. (a) Particle 1; (b) Particle 10.; (c) Particle 16; (d) Particle 21.

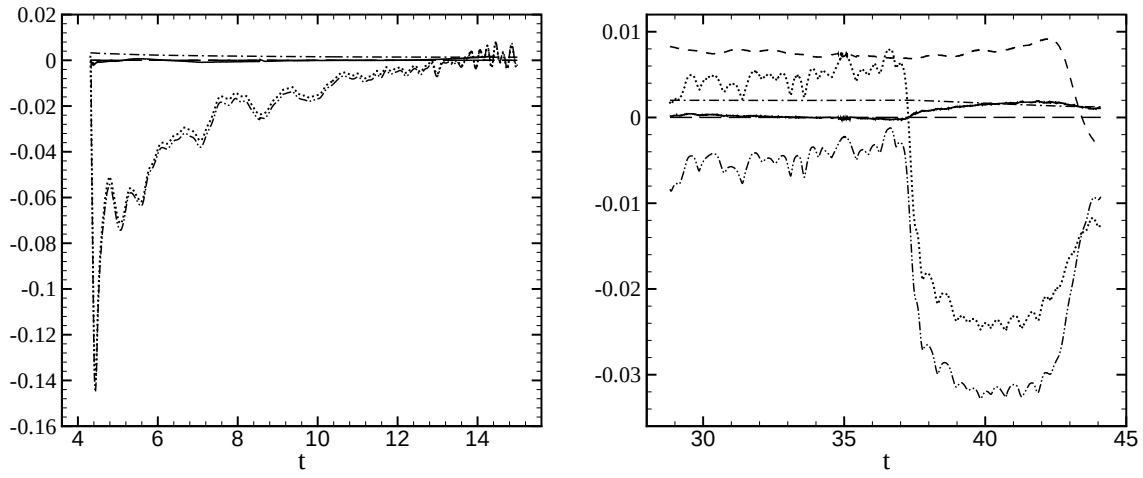

(a) (b)

Figure 4.34: Terms in the reaction zone temperature Equation (2.18) along the same particle paths as in Fig. 4.30 for the case $\theta_{CJ} = 3.5$. The particles are injected along the vertical wall of the corner. ····· Lagrangian temperature; –·–· heat release; – – – curvature; — — transverse divergence; –··–·· unsteadiness. The solid line is the difference between the left-hand side and the right-hand side in Equation (2.18), as computed from the above terms. (a) Particle 1; (b) Particle 10.

A second variation in $\mathrm{D}T/\mathrm{D}t$ is linked to the arrival of the transverse wave at $t \cong 43$. Further analysis after $t = 44$ is not possible due to the strong upward moving shock wave described earlier.

4.3 Conclusions: a failure model for diffraction

In the previous sections, the terms in the reaction zone structure equation were investigated along particle paths for sub-, near-, and super-critical cases. The study was focused on particle trajectories running along the two edges of the detonation front, the axis of symmetry of the channel, and the lower wall of the corner. These two directions are representative of two extremely different dynamics of the wavefront, as exemplified by the case $\theta_{CJ} = 3.5$. Moreover, in these two special cases, the flow field exhibits symmetry (about the channel axis and the corner wall), which noticeably simplifies the reaction zone structure equation.

In the cases presented here, we found that the contributions of the curvature

and transverse divergence terms to the Lagrangian derivative of temperature are negligible. This result is consistent with the findings of Eckett et al. (2000) for the case of direct initiation of cylindrical and spherical detonations, where the unsteady processes appear to be dominant. The reaction zone structure equation can therefore be reduced to

$$\left(1-M^2\right)\, C_p\, \frac{\mathrm{D}T}{\mathrm{D}t} = \left(1-\gamma\, M^2\right)\, Q\, k\, \rho\, (1-Z) \exp\left(\frac{-E_a}{T}\right) + w_\eta\, \left(D_a - w_\eta\right)_{,t} + \frac{P_{,t}}{\rho}\,. \tag{4.3}$$

In the next chapter, we will show that the $D_n - \kappa$ diagrams extracted from our numerical simulations show a large initial deviation with respect to the diagrams for slightly-curved, quasi-steady diverging detonation.

A second observation is that the common feature in the temperature history of particles that fail to ignite is a negative value of $\mathrm{D}T/\mathrm{D}t$ following the leading shock. In Fig. 4.31, the Lagrangian derivative of temperature is very close to zero for a few particles, but not negative. The detonation front locally recouples, and at a later time, the acceleration of the front near the axis triggers the formation of a large reactive transverse wave. When the activation energy is larger, and the detonation fails, we find particles in Fig. 4.20 where $\mathrm{D}T/\mathrm{d}t < 0$. These facts suggest that a vanishing Lagrangian derivative of temperature at post-shock conditions is the criterion for the local decoupling of the shock front from the reaction zone,

$$\mathrm{D}T/\mathrm{D}t\big|_s = 0. \tag{4.4}$$

This hypothesis was already advanced by Schultz (2000) in his experimental study of detonation diffraction. From (4.3), we obtain

$$Q\, k\, \rho_s \exp\left(\frac{-E_a}{T_s}\right) = -\frac{1}{\left(1-\gamma\, M_s^2\right)} \left[w_\eta\, \left(D_n - w_\eta\right)_{,t} + \frac{P_{,t}}{\rho}\right]_s . \tag{4.5}$$

The right-hand side of Equation (4.5) can be evaluated by using shock-jump condi-

tions, and it is ultimately a function of γ and the shock deceleration $\dot{D}_n$. It should be noted that Equation (4.5) is strictly linked to the assumption of a single-step reaction mechanism, and that the attainment of the branching temperature has been suggested instead as the criterion for failure in two-step models where a thermally neutral induction zone is followed by an exothermic main reaction layer.

A final observation is that the search for a global criterion for detonation diffraction can be restricted to a test for failure at the channel axis. From the examples above, we can argue that if the particle ignition delay is not too large along the channel axis (i.e., $\mathrm{D}T/\mathrm{D}t$ is positive), the detonation eventually recouples, triggering a re-ignition mechanism through formation of a transverse shock. By evaluating Equation (4.5) at the axis of symmetry, the problem is reduced to finding an estimate of the shock decay at the channel axis. The shock decay is linked to the geometric scale of the problem, and therefore we expect $\dot{D}_a \sim D_{CJ}^2/H$. The next chapter is devoted to modeling this term.

Chapter 5

Wave front models

Shock-tracking and flow-field diagnostics from direct numerical simulations provide information on local shock curvature, detonation velocity, shock acceleration and flow gradients.

In this chapter, we compare some of these results with predictions derived from models of reactive and non-reactive flows. In Section 5.1, we use Skews' construction for a diffracting non-reactive shock, and compare his computation of the disturbance angle with the value estimated from the present simulations. In Section 5.2, we plot D_a and D_w against the corresponding values of curvature, and compare these curves with the $D_n(\kappa)$ plots from quasi-steady, quasi-one-dimensional theory of detonations (Section 2.4). One outstanding issue from the previous chapter is the estimate of detonation decay along the channel axis. Particle data analysis indicate that this quantity has to be used to model the unsteady terms of Equation (4.5) near critical conditions. In Section 5.3, we examine the applicability of a blast decay model, while in Section 5.4 we apply Whitham's theory of Geometrical Shock Dynamics in the limit of strong shocks.

5.1 Skews' construction for diffracting detonations

One of the key features of the diffraction process is the propagation of the signal generated by the expansion waves emanating from the corner. There is a distinct point where the head of the disturbance intersects the undisturbed detonation. The

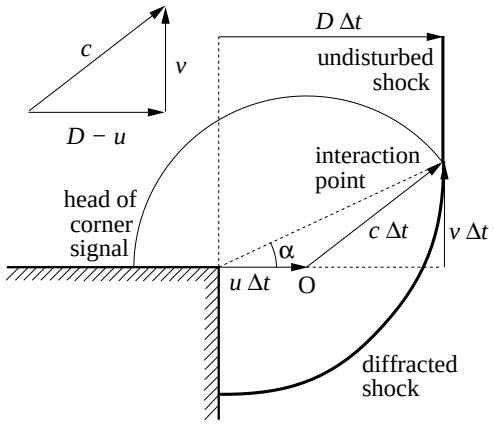

Figure 5.1: Schematic of a diffracting shock (Skews' construction).

propagation speed of this point, v, can be evaluated with the help of a suitable extension of Skews' geometric construction (Skews 1967) for non-reacting diffracting shocks, shown Fig. 5.1. The disturbance is propagating at the local acoustic speed c while being convected downstream at a speed u. The undisturbed front moves at a constant speed D. The corresponding angle between the disturbance trajectory and the normal of the undiffracted shock, α, can be found by carrying out a Huygen's construction for the wavefront of a sound wave. As discussed in Skews, the wavefront is a circle, of radius $c\,\Delta\,t$, whose origin is at point O translated downstream from the corner a distance $u\,\Delta\,t$. From the geometric construction we have

$$\tan\alpha = \frac{v}{D} = \frac{\sqrt{c^2 - (D-u)^2}}{D}. \tag{5.1}$$

In the non-reactive case, the values u and c are evaluated from the post-shock state behind the undisturbed shock. In the reactive case, we need to examine the dependence of the sonic parameter $c^2 - w^2$ from the progress variable Z, Fig. 5.2 (a). The correspondig variation of α is shown in Fig. 5.2 (b).

Recall that w is the flow velocity in the reference of the undisturbed shock, $w = D_{CJ} - u$. In a CJ detonation, $c = w$ at the end of the reaction, $Z = 1$. Since in corner-turning experiments with CJ detonations α is finite (for instance, Schultz 2000), the disturbance must propagate inside the reaction zone, between $Z = 1$ and

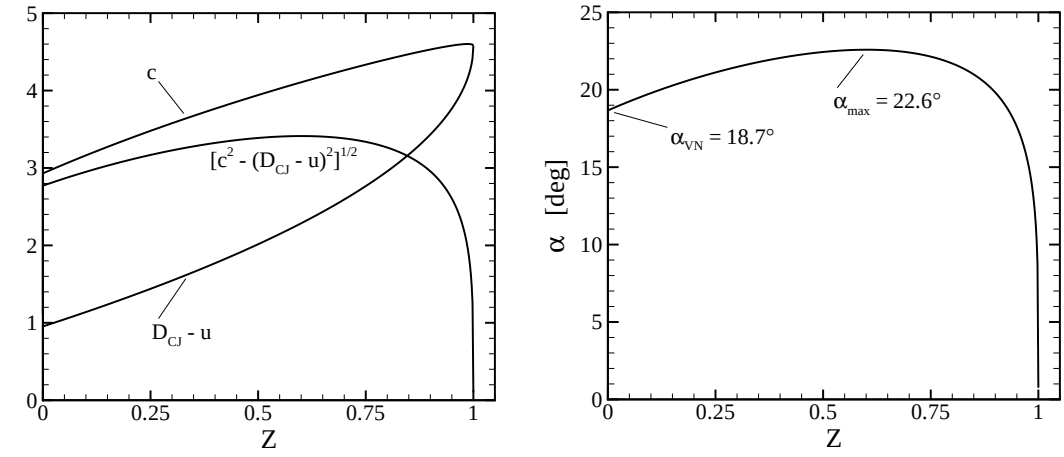

(a) (b)

Figure 5.2: Sound speed, relative particle velocity, square root of the sonic parameter, frame (a), and disturbance angle plotted vs. the progress variable Z, frame (b).

the leading shock.

To see what ZND state we need to consider, α is measured from our numerical simulations. The technique we use is described in Section 3.3. The trace of the disturbance behind the shock can be very closely approximated by a straight line in the x-y plane, at an angle $\alpha_m = 22.7°$. This value is close to the maximum deflection angle, 22.6°, displayed in Fig. 5.2. Disturbance angles have been measured by Schultz (2000) from a sequence of schlieren images in sub-critical detonation diffraction of hydrocarbon mixtures and hydrogen mixtures. The typical resolution obtained from these measurements was approximately $\pm 3°$. These results were compared with values of α computed from the corresponding ZND profiles. Also in this case, the disturbance propagation angles corresponding to the maximum disturbance velocity were found to be in good agreement with the experimental measurements.

5.2 Detonation asymptotics

In studying the problem of detonation diffraction, an important question is: When can the evolution of the leading wavefront be approximated by a steady-state, quasi-one-dimensional wave? This model was discussed in Section 2.4, where it was shown that

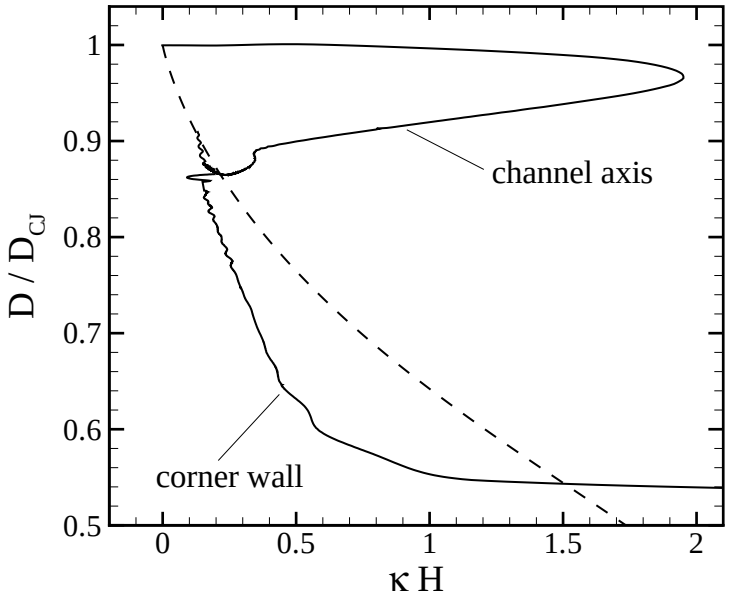

Figure 5.3: D_n–κ diagram for $\theta_{CJ} = 1$. —— evaluated along the channel axis of symmetry and the corner wall from numerical simulation; – – – computed for quasi-steady, quasi-one-dimensional reaction zone.

the wavefront curvature κ is a function of the propagation velocity D_n. The $D_n(\kappa)$ relation is uniquely a function of the chemical reaction rate model. For sufficient state-sensitivity of the chemical kinetics, the $D_n(\kappa)$ curve exhibits at least two branches of solutions, with a backward C-shaped curve and a turning point, as shown in Fig. 5.4 (dashed curve).

The quasi-steady model is based on the assumption of a dominant balance between the contributions of curvature and energy release. The unsteady terms are assumed to be small compared to the quasi-steady terms, restricting the application to slightly unsteady flow. This model has been used by He and Clavin (1994) to study the conditions for initiation of curved detonation fronts. According to this theory, a successful detonation initiation requires the formation of a sonic point in the rear of the reaction zone, so that the energy release area is effectively insulated by incoming rarefactions. If the radius of curvature and speed of the detonation front decrease below the value at the turning point, a steady-state solution cannot exist, and the

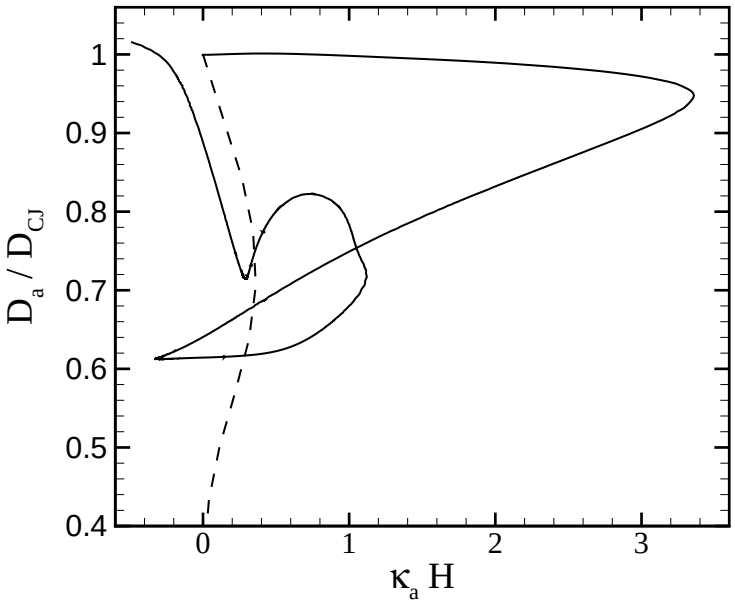

Figure 5.4: D_n–κ diagram along the channel axis of symmetry for $\theta_{CJ} = 3.5$. —— evaluated along the channel axis of symmetry from numerical simulation; – – – computed for quasi-steady, quasi-one-dimensional reaction zone.

detonation will always be weakened by the rarefaction waves behind the front.

The quasi-steady model is the basis of Detonation Shock Dynamics, developed by Stewart and Bdzil (1988). The theory of DSD defines the motion of the detonation shock in terms of curvature-dependent speed propagation. The D_n–κ relation can be extended to a $\dot{D}_n$–D_n–κ model as well as a $\ddot{D}_n$–$\dot{D}_n$–D_n–κ–$\dot{\kappa}$ (Yao and Stewart 1996). The DSD method, as applied for instance to the corner-turning problem, does not solve the reactive Euler equations, but rather the intrinsic partial differential equation associated with the front dynamics of a particular reactive system. Comparisons with direct numerical simulations for condensed-phase explosives (whose reaction rate does not depend strongly on the thermodynamic state) show that the shock motion is reproduced by DSD with high precision (Aslam and Stewart 1999; Bdzil and Aslam 2000).

In Figs. 5.3 to 5.5, steady-state, quasi-one-dimensional solutions are compared with the D_n–κ curve resulting from direct numerical simulation. The three cases ex-

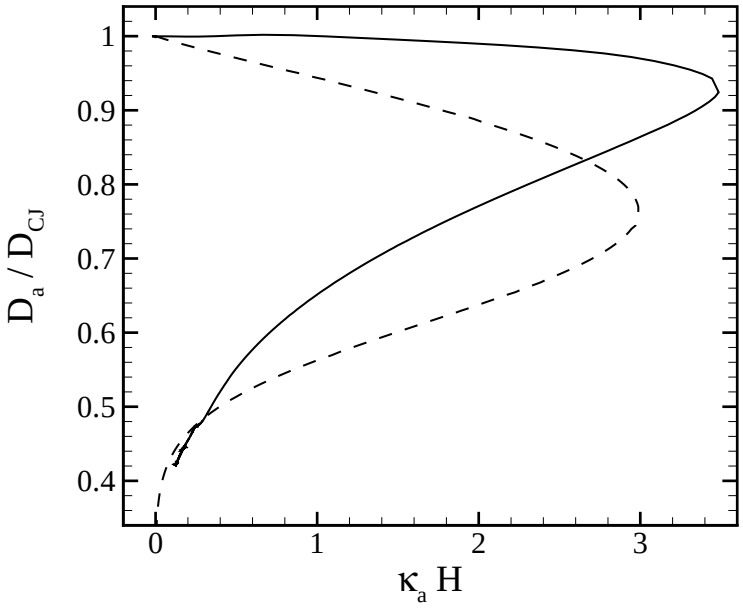

Figure 5.5: D_n–κ diagram along the channel axis of symmetry for $\theta_{CJ} = 4.15$. —— evaluated along the channel axis of symmetry from numerical simulation; – – – computed for quasi-steady, quasi-one-dimensional reaction zone.

amined are the super-critical, sub-critical and near-critical examples of the previous chapter. Detonation speed and curvature are computed in a post-processing phase by a finite-difference technique, as described in Section 3.3. The steady-state curve is computed numerically as the solution of a two-point boundary problem with a regularity condition at the generalized CJ point. This technique is described in Section 2.4.

Super-critical case. In the super-critical case ($\theta_{CJ} = 1$), the two detonation fronts, along the axis of symmetry and the corner wall, evolve differently (Fig. 5.3). Near the corner, the front curvature is initially very high and D_w is about one-half of the CJ detonation speed. On the axis of symmetry, D_a never decreases below $0.85D_{CJ}$, whereas κ_a builds up to a value of about $2/H$, and then rapidly decreases. Eventually, at a distance of about $6\,H$ from the corner, both curves converge on the quasi-steady solution.

Near-critical case. The wavefront is transient for a much longer time in the near-critical case ($\theta_{CJ} = 3.5$) than in the super-critical case. In fact, Fig. 5.4 shows that the portion of the detonation front along the axis of symmetry has not achieved a steady-state solution. Figure 4.26 provides an indication of the irregular evolution of the wavefront in the last part of the simulation. Curvature values can be displayed in the D_n–κ plot only up to the time corresponding to frame (i), when κ_a is negative. After this point, the D_n–κ diagram becomes erratic: the axial curvature is positive and very large in frame (l) and (m), and is close to zero again in frame (n). Due to the overlapping system of transverse waves, at the end of the simulation the main reaction zone along the axis of symmetry is not reducible to a quasi-one-dimensional, quasi-steady solution. At this point, the wavefront is at a distance of about $14\,H$ from the corner.

Sub-critical case. In the sub-critical case ($\theta_{CJ} = 4.15$), the wavefront evolution is smoother, as expected from a situation where the chemical reaction is undergoing quenching without any restoring mechanism. Interestingly, at a distance of about $6\,H$, the computed D_n–κ curve approaches the lower end of the quasi-steady curve displayed in Fig. 5.5. While it is clear that at this point the detonation has failed, the computational domain is not large enough to show whether the computed D_n–κ curve would find a second turning point and move on the so-called extinction branch (not shown in figure) investigated by Stewart and Yao (1998). The progressive decoupling of the shock from the reaction zone makes this problem closer to a blast decay than to a detonation. We examine this hypothesis in Section 5.3.

We conclude this section by pointing out that when the wavefront is sufficiently smooth for the evaluation of κ, the D_n–κ relation eventually converges to the diagram for quasi-steady, quasi-one-dimensional detonation propagation. However, this convergence occurs at the end of a long transient, at a distance approximately $6\,H$ from the corner. We also note that in the $\theta_{CJ} = 3.5$ case, where the detonation is transmitted successfully, the front curvature is several times larger during this transient than

at the turning point in the corresponding quasi-steady $D_n(\kappa)$ diagram. These results confirm the conclusions of Section 4.3, that in near-critical conditions the dominant balance is between chemical energy release and unsteadiness. Finally, we note that the maximum curvature criterion proposed by He and Clavin for detonation initiation cannot be extended to detonation diffraction to find critical conditions when the reaction rate is strongly dependent on the thermodynamic state.

5.3 Reduction to blast equation

Another issue is the estimate of the peak value of detonation decay along the channel axis. This is an important ingredient in the approximate model of detonation failure developed by Schultz (2000). In Fig. 5.6, the normalized time derivative of the axial speed, $\dot{D}_a$, is plotted as a function of the distance from the corner, x_a. In the interval shown here, the behavior of $\dot{D}_a$ is remarkably similar for all cases, and the minimum value scales almost linearly with θ_{CJ}. As expected, when the expansion signal arrives at the axis of symmetry, a more sensitive reaction mechanism (larger θ_{CJ}) results in a more rapid decoupling of the shock from the reaction zone and therefore in a larger shock decay rate. This decoupling is not immediate, a distance of 4 to 6 half-reaction zones is necessary to reach the peak value of deceleration. Simulations in a non-reacting gas indicate that at least part of this delay is due to the finite thickness associated with the numerical representation of the shock. The similar evolution of acceleration in Fig. 5.6 only occurs at early times, while the subsequent evolution is different. The near-critical and super-critical diffraction cases present positive accelerations that accompany the re-ignition mechanisms, whereas in the sub-critical case D_a decreases monotonically.

The three curves in Fig. 5.6 are compared with the estimate from a blast model, discussed in this section, and with the result from Whitham's theory, presented in the next section.

Very little experimental data are available from the literature; Edwards et al. (1979) report the variation of frontal velocity from a CJ value of 2400 m/s in det-

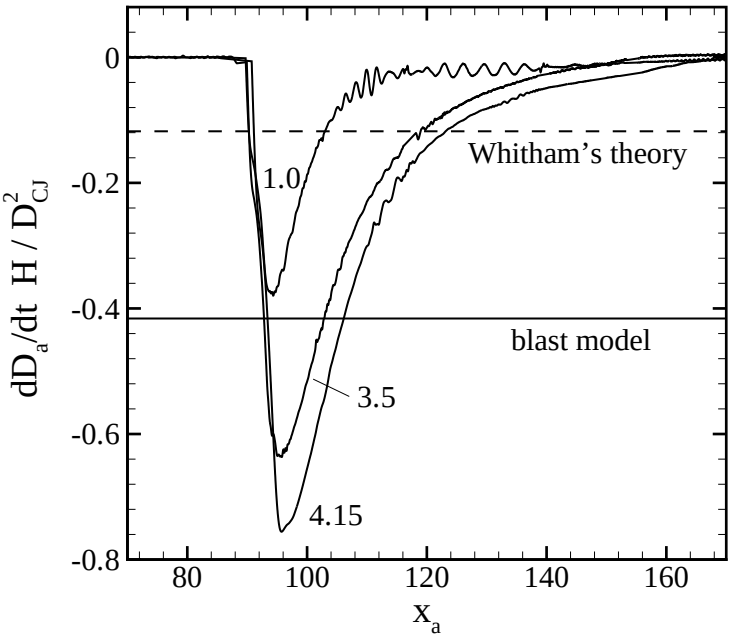

Figure 5.6: Shock deceleration as a function of the distance from the corner vertex, parametrized by θ_{CJ}.

onation diffraction of oxyacetylene from a rectangular tube. Velocities are obtained from streak photographs at near-critical and sub-critical conditions as a function of distance. An approximate estimate of the peak value $\dot{D}_a$, normalized by D_{CJ}^2/H, can be extracted from these diagrams by measuring the slope of the two curves. The two values we found, -0.213 (near-critical) and -0.246 (sub-critical), are useful in the sense that they are of the same order of magnitude of the results from the numerical simulations.

In this section, we treat the flow near the channel axis as a cylindrical blast (Korobeinikov 1991), of radius r. This approach was followed by Eckett et al. (2000) in the study on critical energy of initiation, and extended by Schultz (2000) to detonation diffraction. From the blast similarity relation, we have

$$\frac{\mathrm{d}r}{\mathrm{d}t} = \delta \frac{r}{t}, \tag{5.2}$$

where r is the shock radius. By integrating Equation (5.2) (in two dimensions, $\delta =$

1/2) we obtain

$$r = r_b \sqrt{\frac{t}{t_b}}. \tag{5.3}$$

We take r_b to be the shock distance from the (virtual) blast singularity when the expansion signal arrives at the axis of symmetry. The transition from planar wave to cylindrical blast of radius r_b is assumed to be instantaneous. Then

$$t_b = \frac{r_b}{2\, D_{CJ}}. \tag{5.4}$$

Since here $\kappa = 1/r$ by definition, Equation (5.3) allows us to derive a linear relation between detonation speed and front curvature

$$D_a = D_{CJ} \frac{\kappa}{\kappa_b}, \tag{5.5}$$

where $\kappa_b = 1/r_b$. Comparison of this result with a typical D_n–κ curve of a sub-critical diffraction, Fig. 5.5, indicates that the blast model can be applied only qualitatively; No portion of the curve from the simulation can be approximated by a straight line passing by the origin. Differentiating D_a with respect to time gives

$$\dot{D}_a = -\frac{1}{2} \frac{D_a}{t}. \tag{5.6}$$

The estimated maximum deceleration at r_b is therefore

$$\dot{D}_b = -D_{CJ}^2\ \kappa_b. \tag{5.7}$$

Up this point, the parameter κ_b is unknown. If we estimate the initial blast radius to be the x distance from the corner vertex to the point of arrival of the corner signal, then

$$r_b = \frac{1}{\kappa_b} = \frac{H}{\tan\alpha}. \tag{5.8}$$

From Equation (5.7),

$$\dot{D}_b = -\frac{D_{CJ}^2}{H}\ \tan\alpha. \tag{5.9}$$

For $\alpha = 22.6°$ (from Skews' construction) we find

$$\kappa_b H = -\frac{H}{D_{CJ}^2}\dot{D}_b = 0.416. \tag{5.10}$$

With a reasonable estimate of the initial blast radius, the cylindrical blast model provides the correct magnitude of the initial shock decay rate (Fig. 5.6). However, the derivation above ignores the reactivity of the flow, so that it is independent from the reaction mechanism. In addition, the value of κ is roughly one order of magnitude smaller than the maximum value obtained from numerical simulations. Shock curvature is difficult both to compute consistently (see Appendix A) and to model, since a small differential velocity of the wavefront can result in a large curvature. The curvature peak value in Figs. 5.3 to 5.5 is reached in a transient situation where there is a strong gradient of shock deceleration. This gradient is absent in the cylindrically symmetric blast wave. Thus, the usefulness of the blast decay model is limited to confirming the scaling of the shock deceleration with D_{CJ}^2/H and to provide a reference for an average value of the shock decay rate.

5.4 Whitham shock dynamics

In this section, we compare Whitham's solution for a plane shock diffraction at a sharp corner (Whitham 1974) with our results on detonation diffraction. To simplify the analysis, we will use the limit of strong shocks. As in the previous section, we expect the results to be applicable to a case where the reaction is quenching, i.e., the diffraction is sub-critical.

In examining the results of the theory, it should be kept in mind that, while a curved, non-steady shock involves two-dimensional waves propagating in the region behind it (see, for instance, Fig. 5.1), Whitham's approximation describes the propagation of these waves only where they intersect the shock. Based on linear geometrical optics, the theory uses the concept of orthogonal trajectories of the successive position of a shock, or "rays." The dependence between the local shock Mach number M

and the ray-tube area (or a function proportional to it, A) is expressed by the area function,

$$\frac{A}{A_0} = \frac{f(M)}{f(M_0)}. \tag{5.11}$$

In Cartesian coordinates, the governing equation of Geometrical Shock Dynamics can be written in terms of M and the ray angle θ behind the shock with respect to the x axis, as

$$\frac{\partial}{\partial x}\left(\frac{\sin\theta}{M}\right) - \frac{\partial}{\partial y}\left(\frac{\cos\theta}{M}\right) = 0 \tag{5.12a}$$

$$\frac{\partial}{\partial x}\left(\frac{\cos\theta}{M}\right) + \frac{\partial}{\partial y}\left(\frac{\sin\theta}{M}\right) = 0. \tag{5.12b}$$

In characteristic form,

$$\theta \pm \omega(M) = \text{constant} \qquad \text{on} \quad C^{\pm} : \frac{\mathrm{d}y}{\mathrm{d}x} = \tan(\theta \pm m), \tag{5.13}$$

where

$$\omega(M) = \int_1^M \frac{dM}{A\,C}, \tag{5.14}$$

$$\tan m = \frac{A\,C}{M}, \tag{5.15}$$

and

$$C(M) = \sqrt{\frac{-M}{A\,A'}}. \tag{5.16}$$

The propagation of waves along the diffracting shock becomes analogous to the propagation of rarefaction waves in one-dimensional, unsteady compressible gas dynamics, with the displacement of the wall corresponding to the piston withdrawal. The solution consists of a simple region, a "fan" centered at the corner vertex, up to the point where C^+ characteristics reflect at the channel axis (Fig. 5.7).

In the strong shock limit, the area function simplifies to

$$\frac{A}{A_0} = \left(\frac{M}{M_0}\right)^{-n}, \tag{5.17}$$

with n a constant depending only on the gas ratio of specific heat,

$$n = 1 + \frac{2}{\gamma} + \sqrt{\frac{2\,\gamma}{\gamma - 1}}. \tag{5.18}$$

Equation (5.13) becomes

$$\theta \pm \log(M) = \text{constant} \qquad \text{on} \quad C^{\pm} : \frac{\mathrm{d}y}{\mathrm{d}x} = \tan(\theta \pm m), \tag{5.19}$$

where m is the slope of the first characteristic C_0^+, $m = \arctan(1/\sqrt{n})$. For $\gamma = 1.22$, $n = 5.956$ and $m = 22.28°$, which is remarkably close to the measured value 22.7° of Section 5.1.

The Mach number at the wall, M_w, can also be derived directly by taking a C^- characteristic crossing the fan and originating from the uniform region, where $M = M_0$ and $\theta = 0$,

$$M_w = M_0 \exp\left(\frac{\theta_w}{\sqrt{n}}\right). \tag{5.20}$$

Here $\theta_w = -\pi/2$ and therefore $M_w = 0.5253\,M_0$. This result does not compare too well with Fig. 4.3, where sub-critical detonations exhibit a wall shock speed of about 40% of the initial CJ value. However, Whitham's theory predicts that M_w is constant, and indeed we see that in failing detonations D_w is approximately constant until the arrival of the reflected expansion wave from the channel axis. Also, Fig. 5.7 shows that the front has zero curvature between the wall and the C^+ characteristics at the angle $m - \pi/2$. There is a qualitative resemblance of this result with the schlieren images in Fig. 4.14.

The equation of the shock before reflection for $-\pi/2 \le \theta \le 0$ is

$$\frac{x}{M_0\,a_0\,t} = \left(\frac{n+1}{n}\right)^{1/2} e^{\theta/\sqrt{n}} \cos(m + \theta) \tag{5.21a}$$

$$\frac{y}{M_0\,a_0\,t} = \left(\frac{n+1}{n}\right)^{1/2} e^{\theta/\sqrt{n}} \sin(m + \theta). \tag{5.21b}$$

To find the curvature before reflection at the axis, we apply the formula

$$\kappa = \frac{x'\,y'' - y'\,x''}{(x'^{\,2} + y'^{\,2})^{3/2}} \tag{5.22}$$

where $'$ and $''$ denote first and second derivative with respect to θ. The result is

$$\kappa = \frac{1}{M_0\,a_0\,t}\,\frac{n}{n+1}\,e^{-\theta/\sqrt{n}}, \tag{5.23}$$

that is, the radius of the curved shock increases linearly with time along C^+ characteristics. The curvature jumps discontinuously to zero along the two limiting C^+ characteristics, at angles m and $m - \pi/2$.

As the first characteristic C_0^+ intersects the channel axis at the critical time $t_c = H\sqrt{n}/M_0\,a_0$, the curvature computed from Equation (5.23) is

$$\kappa_{a,\,0} = \frac{\sqrt{n}}{n+1}\,\frac{1}{H}. \tag{5.24}$$

When the other C^+ characteristics from the fan reflect at the channel axis, a non-simple region is formed which is difficult to compute. The first reflected characteristic, C_0^-, separating the two regions, propagates a second discontinuity in curvature, see below. C_0^- can be found by a procedure analogous to the one used in unsteady one-dimensional compressible flow. The slope is

$$\frac{\mathrm{d}y}{\mathrm{d}x} = \tan\,(\theta - m), \tag{5.25}$$

and for any point $(x,\,y)$ on C_0^- we can find a C^+ characteristic belonging to the simple region such that

$$\frac{y}{x} = \tan\,(\theta + m). \tag{5.26}$$

The system (5.25) and (5.26) can be reduced to an ordinary differential equation in $y(\theta)$ to be solved with the condition $y(0) = H$. Integration can be performed from 0 to $m - \pi/2$, where the slope of C_0^- becomes infinite. To compute the integral, we use the auxiliary variable $z = y(x)/x$ and then combine the two equations above in the

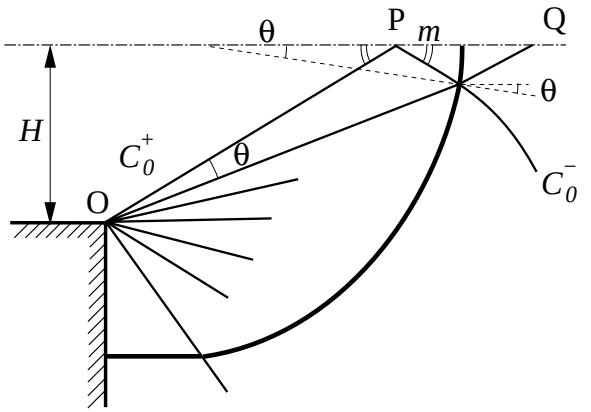

Figure 5.7: Detonation diffraction around a corner. $-\cdot-\cdot$ denotes the axis of symmetry of the channel

form

$$\frac{\tan^2 m - 1 - 2\,z\tan m}{2\tan m\,(1+z^2)}\,\mathrm{d}z = \frac{\mathrm{d}x}{x}. \tag{5.27}$$

The result,

$$y_{C_0^-} = H\,\frac{\tan(\theta+m)}{\tan m}\sqrt{\frac{1+\tan^2 m}{1+\tan^2(m+\theta)}}\,\exp\left(\frac{\tan^2 m - 1}{2\,\tan m}\,\theta\right) \tag{5.28}$$

can be used to evaluate acceleration and curvature at axis at the instant following t_c as $\theta \to 0$. The acceleration is found by using the conservation of the quantity

$$\theta + \sqrt{n}\,\log\frac{M(\theta)}{M_0} = \sqrt{n}\,\log\frac{M_a}{M_0} \tag{5.29}$$

along a C^+ characteristic. In Equation (5.29), M_a is the Mach number at the axis in the non-simple region. If $M(\theta)$ is evaluated in the fan, then

$$M_a = M_0\exp\left(\frac{2\theta}{\sqrt{n}}\right) \tag{5.30}$$

at the position given by the positive characteristic whose slope in the fan is $m+\theta$. We still need to find this position in relation to the value of θ along a C^+ characteristic in the fan. Since the angle in Q is equal to m plus corrections of order θ, $\mathrm{O\hat{Q}P} =$

$m + \mathcal{O}(\theta)$, the distance $\overline{PQ}$ is approximately

$$\overline{PQ} \cong \frac{H}{\sin^2 m}\,\delta\theta = H\,(n+1)\;\delta\theta \tag{5.31}$$

for an infinitesimal increment $\delta\theta$ (see Fig. 5.7). The deceleration of the axial shock, after the reflection of the first characteristic, is found in the limit of $\delta\theta \to 0$ by comparing the decrement in velocity from M_0 to M_a with the time to travel the distance $\overline{PQ}$,

$$\dot{D}_d = D_{CJ}^2 \lim_{\delta\theta\to 0} \frac{M_a/M_0 - 1}{\overline{PQ}} = -\frac{1}{n+1}\frac{2}{\sqrt{n}}\frac{D_{CJ}^2}{H}. \tag{5.32}$$

We assume that this quantity, $\dot{D}_d$, is the maximum value of shock decay along the channel axis.

The axial curvature immediately after reflection of C_0^+ is found by realizing that a discontinuity in κ can only be located along C_0^- and that at any point $(x_{C_0^-},\, y_{C_0^-})$ the shock normal orientation is exactly θ. Since the front is continuously expanding, we expect this curvature to take the maximum value at P,

$$\kappa_d = \lim_{\theta\to 0} \frac{-\sin\theta}{H - y_{C_0^-}} = \frac{2\sqrt{n}}{n+1}\frac{1}{H}. \tag{5.33}$$

Since κ_d is exactly twice the curvature at the axis at the instant preceding the reflection of the first characteristic, we see that indeed a second discontinuity in curvature propagates along C_0^-. As a consistency check, we take the derivative of Equation (5.17) along a ray-tube (say, parallel to the x axis),

$$\frac{1}{A}\frac{\mathrm{d}A}{\mathrm{d}x} + \frac{n}{M}\frac{\mathrm{d}M}{\mathrm{d}x} = 0, \tag{5.34}$$

and substitute $\kappa_a\, A = \mathrm{d}A/\mathrm{d}x$, and $D_a\, \mathrm{d}M_a/\mathrm{d}x = \dot{M}_a$. We find

$$\kappa_a\, D_a^2 + \frac{1}{n}\dot{D}_a = 0, \tag{5.35}$$

so that, immediately past the reflection of C_0^+,

$$\frac{\kappa_d}{\dot{D}_d} = -\frac{1}{n}\,\frac{1}{D_{CJ}^2}. \tag{5.36}$$

This result can be obtained directly from Equations (5.32) and (5.33).

Equation (5.33) is used in Appendix A to provide a reference for a convergence study of curvature in the non-reactive case. When applied to the reactive cases examined in the previous chapter,

$$\dot{D}_d\,\frac{H}{D_{CJ}^2} = -0.1178 \qquad \text{and} \qquad \kappa_d\,H = 0.7017. \tag{5.37}$$

It is evident that κ_d and $\dot{D}_d$ underpredict the peak curvature and the maximum shock decay. Extensions of Whitham's theory to include detonations have been recently attempted by Li and Ben-Dor (1998) in the case of highly overdriven detonations, and by Bartlmä (1990) for converging and diverging channels. The latter study is the one of interest for the corner-turning problem, since a detonation propagating at a speed below the CJ point, as in an expanding channel, can no longer exist in steady form. Once the functional dependence (5.11) that is relevant to detonation propagation is found, then Equation (5.12), whose derivation is purely geometric, can be used to compute the diffracting flow. However, in that respect, Bartlmä seems to be concerned only with the increase in induction length caused by a detonation expanding in cylindrical (or spherical) geometry, and no feedback from the reaction zone to the shock is considered. A dependence from chemical kinetics cannot appear in this approach. The problem of finding a closed-form expression to approximate a weakly coupled detonation front in an area-shock relation is still without solution.

5.5 Closure of the failure model

To conclude this chapter, we consider again the criterion of diffraction failure that was introduced in Section 4.3. For simplicity, we take the limit of strong shocks ($M^2 \gg 1$)

to compute the post-shock state,

$$P_s = \frac{2}{\gamma+1}\, D_n^2 \qquad \rho_s = \frac{\gamma+1}{\gamma-1} \qquad w_s = \frac{\gamma-1}{\gamma+1}\, D_n \qquad M_s^2 = \frac{\gamma-1}{2\gamma}. \tag{5.38}$$

In this limit, the ratio of post-shock temperature T_s to CJ post-shock temperature T_{vN} is

$$\frac{T_s}{T_{vN}} = \frac{D_n^2}{D_{CJ}^2}. \tag{5.39}$$

By substituting the expressions above, and recalling the definition of θ_{CJ}, the critical condition for diffraction failure, Equation (4.5), becomes

$$Q\, k\, \exp\left(-\frac{D_{CJ}^2}{D_a^2}\, \theta_{CJ}\right) = -\frac{12}{3-\gamma}\, \frac{(\gamma-1)^2}{(\gamma+1)^3}\, D_a\, \dot{D}_a. \tag{5.40}$$

This expression stresses more clearly the balance between the energy release rate, proportional to $Q\,k$, and a term similar to kinetic energy decay, $D_a\,\dot{D}_a$. Since $Q \sim D_{CJ}^2$, Equation (5.40) is also a comparison of the chemical timescale of the order of $1/k$, with the gasdynamic timescale of the order $D_a/\dot{D}_a$.

From our data particle analysis (Chapter 4), we see that, as the signal expansion arrives at the axis, $\mathrm{D}T/\mathrm{D}t$ does not drop immediately to zero (see Fig. 4.20). The two terms in Equation (5.40) may be comparable only at a critical distance downstream, when the corner expansion has somewhat reduced the reaction rate, since any decrease of D_a below the CJ value is amplified by the exponential term. Since D_a/D_{CJ} approximately varies between 1 and 0.5 (Fig. 4.2), we take the critical point to be such that $D_a = 0.75\, D_{CJ}$. We state that if Equation (5.40) is verified downstream of this point, the shock-reaction decoupling will continue until reaction quenching.

To obtain a relation for θ_{CJ} and H, we still need to model the shock deceleration. By referring to Fig. 5.6, we see that an average value of $\dot{D}_a$ is provided (very crudely) by the blast decay model, Equation (5.9). Equation 5.40 is then reduced to

$$\frac{H\,k}{D_{CJ}}\, \frac{Q}{D_{CJ}^2} = \exp\left(1.78\,\theta_{CJ}\right) \frac{9\,\tan\alpha}{3-\gamma}\, \frac{(\gamma-1)^2}{(\gamma+1)^3}, \tag{5.41}$$

where α is the maximum disturbance angle computed from Skews' construction. By substituting the values of α, Q, k, H, D_{CJ}, and γ, we find the critical normalized activation energy $\theta_{CJ_c} = 4.0$, above which re-ignition does not occur. This value is in good agreement with our results shown in Fig. 4.2. At $\theta_{CJ} = 3.75$, a large transverse wave is still observed in our simulation, but it proves insufficient for re-initiation. At $\theta_{CJ} = 4.0$ (not displayed in Fig. 4.2), no transverse waves are formed. In both cases, the axial shock decay is monotonic.

Chapter 6

Transverse wave formation

In this chapter, we study the mechanism of formation of transverse waves as they appear in our simulation of super-critical detonation diffraction, see Fig. 4.9. Such waves are completely absent in sub-critical diffractions, where chemical reaction is quenched, and are difficult to recognize in near-critical diffractions because of the complexity of the re-ignition structure, see Fig. 4.26.

The trigger for the formation of these waves is shock reflection in the early phases of detonation corner turning, as explained in Section 4.2.1: the foot of the shock lags behind the undisturbed detonation front and reflects from the wall at an angle. To reproduce this situation in a simpler setting, we study a planar CJ detonation moving in a channel over a small "bump," see Fig. 6.1 The obstacle generates a first shock that propagates upward along the main detonation front, followed by an expansion wave when the front moves beyond the obstacle tip. A second shock forms when the front passes the obstacle. In the following, we examine the possibility that acoustic disturbances can form in the wake of this second shock, and later amplify to become transverse detonations. In Section 6.3, an amplification mechanism is discussed based

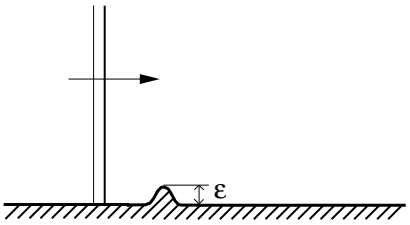

Figure 6.1: Detonation running over an obstacle.

on acoustic waves propagation in the reaction zone of a ZND detonation. The concept of acoustic channel for disturbances that are traveling in the transverse direction of the main shock is also introduced. A comparison with numerical simulations is performed in Section 6.4. We find that waves are amplified in the reaction zone depending on the reaction order and activation energy, and that amplification takes place preferably along contact discontinuities where the sonic parameter reaches a local maximum. These results are consistent with the acoustic theory. In Section 6.5, the amplitude of a transverse wave is tracked in time, and its exponential growth is related to the amplification coefficient found in Section 6.3.

6.1 Computational setting

The planar detonation wave is primed by interpolating onto the grid a pre-computed steady ZND profile, see Section 3.5.2. As in the rest of this work, the wave parameters are set so that the reference half-reaction length $\Delta_{1/2}$ is the same in all cases.

The obstacle is initially located ahead of the leading shock, at the position x_b. The "bump" is described by

$$y = \frac{\epsilon}{2}\left(1 + \cos 2\pi \frac{x - x_b}{\epsilon}\right) \qquad |x - x_b| < \frac{\epsilon}{2}. \tag{6.1}$$

with the total height ϵ equal to a fraction of the half-reaction length, $\epsilon = 0.2$. Implementation of this boundary is based on the ghost fluid technique, Section 3.5. The computational grid measures 100 x 50 in $\Delta_{1/2}$ units, with $N_{1/2} = 45$.

6.2 Non-reactive reference case

We first consider a non-reactive case. Figure 6.2 is a schlieren image showing the main features of this problem; the leading shock (S); the obstacle (O); two weak reflected shocks (SW1 and SW2); the corresponding contact discontinuities (CD1 and CD2). The rarefaction is between SW1 and SW2. A close up of this picture,

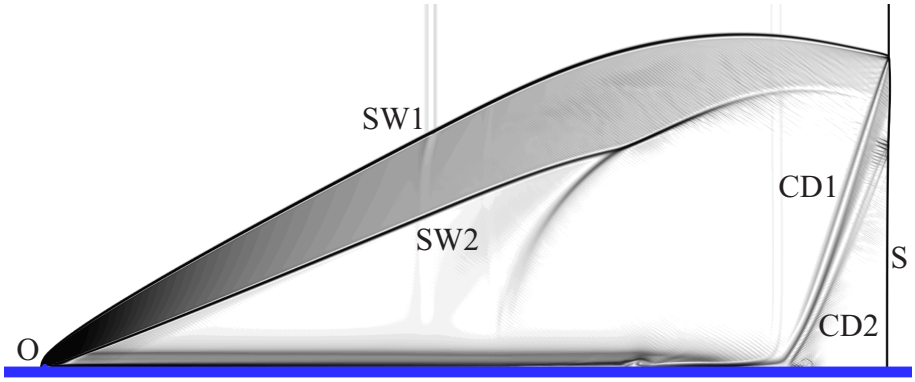

Figure 6.2: Non-reactive shock over an obstacle.

showing wave interactions at the leading front, is displayed in Fig. 6.3 (a). This image measures 35 ϵ (or 7 $\Delta_{1/2}$) in width. Close to the leading front, the second transverse shock SW2 becomes a weak compression wave followed by several wavelets. Since schlieren imaging amplifies every wrinkle in a numerical simulation, we take 4 horizontal slices of the computational domain at the locations indicated in frame (a) and show quantitative profiles in frame (b). The slices are numbered from 1 (top) to 4 (bottom) in the pressure plot of Fig. 6.3 (b). In the scale of the plot, pressure oscillations are very small and their wavelength is approximately ϵ, the only length scale in this non-reactive problem.

We want to find if an exothermic reaction can amplify these small-wavelength disturbances. The results obtained by Strehlow and Fernandes (1965) and Barthel and Strehlow (1966) for infinitesimal, high-frequency, transverse disturbances in a planar ZND detonation are presented in the next section.

6.3 Linear acoustic theory

In acoustic theory, the wavefront moves along rays with speed c with respect to the surrounding medium. For a ZND detonation, we specialize the ray-tracing equations

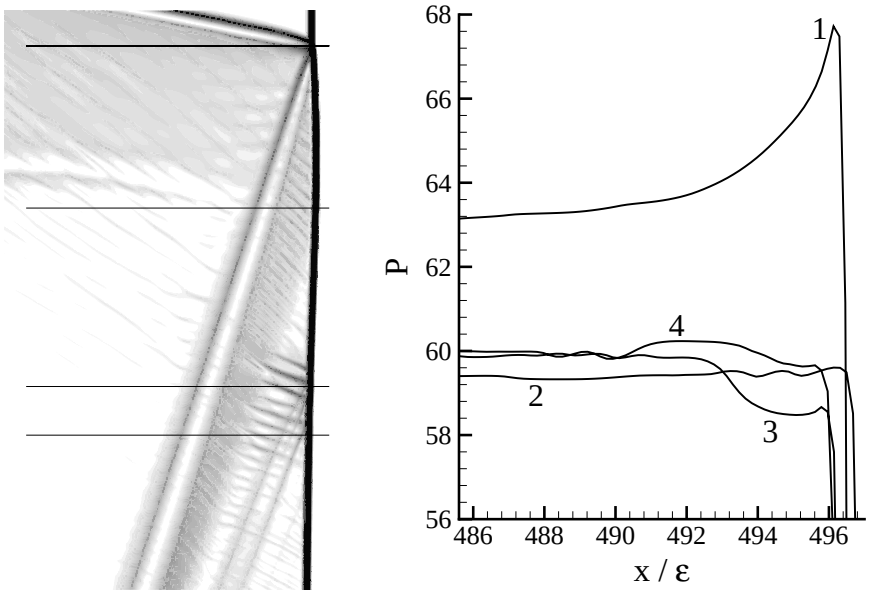

(a) (b)

Figure 6.3: Detail of shock interaction for the non-reactive case. (a) schlieren image; (b) pressure diagrams The four horizontal lines (numbered 1, top, to 4, bottom) in (a) mark where data have been extracted to draw the pressure plots.

(Pierce 1981) as

$$\frac{\mathrm{d}\eta}{\mathrm{d}t} = l\,c + w \tag{6.2a}$$

$$\frac{\mathrm{d}\xi}{\mathrm{d}t} = m\,c \tag{6.2b}$$

and

$$\frac{1}{l}\left(\frac{\mathrm{d}l}{\mathrm{d}t} + \frac{\partial c}{\partial \eta} + l\,\frac{\partial w}{\partial \eta}\right) = \frac{1}{m}\frac{\mathrm{d}m}{\mathrm{d}t}. \tag{6.3}$$

The flow velocity w is evaluated in the reference frame moving with the shock. The coefficient l and $m = (1 - l^2)^{1/2}$ are the direction cosines with respect to the axis η, in the direction of detonation propagation, and ξ, in the transverse direction. If

$$\frac{\mathrm{d}}{\mathrm{d}Z}\left(c^2 - w^2\right) = 0 \tag{6.4}$$

for a value of the progress variable $Z_{\|}$, then any point source inside the reaction zone propagates a wave containing a ray element that asymptotically remains parallel to

the leading shock in the plane $Z_{\|}$. The corresponding direction cosine (Fig. 6.4) is constant

$$l_{\|} = -\frac{1}{\sqrt{2+\gamma}}, \tag{6.5}$$

and $Z_{\|}$ is only a function of γ and the detonation Mach number

$$Z_{\|} = 1 - \left[\frac{1+\gamma M^2}{2\left(M^2-1\right)}\right]^2. \tag{6.6}$$

Since $Z_{\|}$ is found by solving Equation (6.4), the result above does not depend on the specific energy release function $\mathrm{D}Z/\mathrm{D}t$, and it is also valid when the detonation is overdriven.

Acoustic rays that deviate from the plane $Z_{\|}$ rapidly wash out of the detonation or intersect the shock front, where they are reflected. Shock polar analysis for an infinitesimal compression wave shows that for most orientations the wave will reflect at the shock as another compression wave, but always with decreased amplitude (Barthel and Strehlow 1966). Wave amplification is therefore provided only by the energy release due to chemical reaction. Since the point $\left(l_{\|}, Z_{\|}\right)$ is a saddle point in the l–Z phase plane, rays that pass close to it remain in its neighborhood for a relatively long time and are subject to a net amplification. The plane $Z_{\|}$ then acts as an acoustic channel for high-frequency (with respect to the detonation timescale) acoustic disturbances. This result is consistent with the condition on the existence of a maximum in the $c^2 - w^2$ profile for instability of planar detonations to transverse disturbances (Erpenbeck 1966).

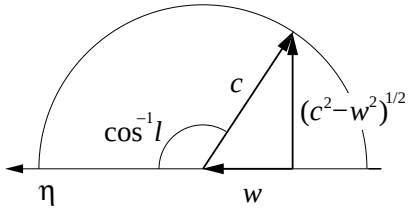

Figure 6.4: Geometry of the wavefront.

The kinetic model for a reaction of order n_r is

$$\frac{\mathrm{D}Z}{\mathrm{D}t} = k\,(1-Z)\;\rho^{n_r-1}\mathrm{e}^{-E_a/T}. \tag{6.7}$$

By assuming that the gradients in the ZND profile are small with respect to the gradients of the disturbance, we write the equations for quasi-one-dimensional flow in the $c_\parallel$ direction, at the angle $\cos^{-1} l_\parallel$ with respect to the η coordinate (Fig. 6.4). This direction of propagation is labeled ν. Thus, we replace a high-frequency ray bundle, traveling in the transverse direction with velocity $(c_\parallel^2 - w_\parallel^2)^{1/2}$, by a high-frequency ray bundle traveling in the ν direction with velocity $c_\parallel$ and wavefront normal to the ν axis. By linearizing the reactive Euler equations at the constant state $(\;)_\parallel$, the problem is reduced to the one-dimensional wave equation in an expanding stream tube with energy addition due to chemical reaction,

$$\frac{\partial^2 s}{\partial t^2} - c_\parallel^2\,\frac{\partial^2 s}{\partial \nu^2} - K\,\frac{\partial s}{\partial t} = 0, \tag{6.8}$$

where $s = \Delta P/P_\parallel = \gamma\Delta\rho/\rho_\parallel$ and

$$K = \frac{\gamma-1}{c_\parallel^2}\,Q\frac{\mathrm{D}Z_\parallel}{\mathrm{D}t}\left[\zeta\,(\gamma-1) + n - (2+\gamma)^{1/2}\right]. \tag{6.9}$$

$\zeta = E_a/T_\parallel$ is the reduced activation energy at $Z_\parallel$. Equation (6.8) admits a solution in the form $s = \exp\left(\Omega\,t + 2\nu\pi/\Lambda\right)$. For a high-frequency wave, such that

$$\frac{K}{2} < 2\pi\,\frac{c_\parallel}{\Lambda}, \tag{6.10}$$

the amplitude of s varies as $\exp\left(Kt/2\right)$.

The last term in the square brackets of Equation (6.9) represents the negative contribution due to wave spreading, i.e., the separation of acoustic rays that are infinitesimally close to the ray $\left(l_\parallel, Z_\parallel\right)$. The neutral curve for amplification is obtained for $K = 0$,

$$\zeta_T = \frac{1}{\gamma-1}\left(\sqrt{2+\gamma} - n\right). \tag{6.11}$$

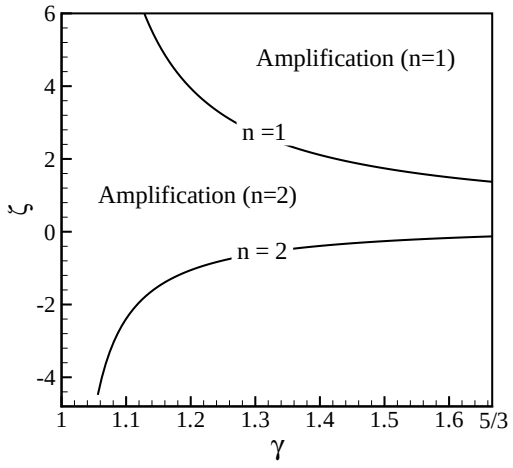

Figure 6.5: Threshold value of normalized activation energy for amplification plotted as a function of the heat capacity ratio γ and the order of reaction n_r. Amplification occurs above the labeled curves.

The threshold ζ_T is plotted in Fig. 6.11 as a function of γ for $n_r = 1$ and $n_r = 2$. From the diagram, we see that an order $n_r = 1$ reaction model corresponds to a wave damping mechanism when E_a is sufficiently small. Conversely, an order $n_r = 2$ reaction model leads to instability for any value of γ, as long as the activation energy is positive.

6.4 Comparison of different reaction models

We compare four simulations computed with different reaction rate models. These cases are labeled from A to D and are listed in Table 6.1, where we use the relation between θ_{CJ} and ζ_T,

$$\zeta_T = \theta_{CJ} \, \frac{T_{vN}}{T_{\|}}. \tag{6.12}$$

The remaining input data are the same used in Chapter 4. From these values, $\cos^{-1} l_{\|} = 56^{\circ}$ and $Z_{\|} = 0.60$. Of the four cases, amplification is predicted when the reaction order model is two (case B and D).

Figure 6.6 shows snapshots of the four simulations, in the same order as in Table 6.1. The effect of the small obstacle is evident in the computations with high-

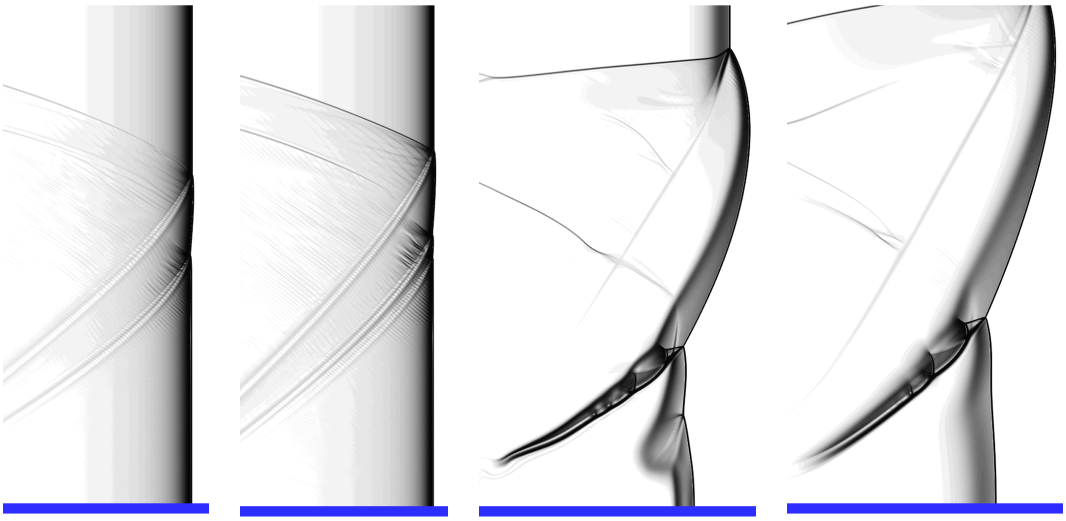

Figure 6.6: Schlieren images for cases A, B, C, D.

sensitivity reaction models, figures 6.6 (c) and (d). The obstacle-induced expansion produces a strongly curved detonation, and several shocks can be observed along the reflected wave. This configuration is quite different from a planar ZND solution, and we expect the amplification mechanism described in Section 6.3 to be of limited use for quantitative predictions.

The modifications induced in the flow by the obstacle are much smaller in the zero-activation energy computations, figures 6.6 (a) and (b). There, the detonation configuration is almost planar, with two weak reflected shocks. The only readily apparent difference between the two computations is that a third contact discontinuity appears only in the second-order reaction simulation. This difference is studied in more detail in the close ups of Fig. 6.7. As in Fig. 6.3, the horizontal lines indicate

case	order	θ_{CJ}	k	ζ_T	Amplification
A	1	0.0	0.3078	0.	No
B	2	0.0	0.2013	0.	Yes
C	1	6.0	24.44	3.051	No
D	2	6.0	13.64	3.051	Yes

Table 6.1: Reaction order and normalized activation energy.

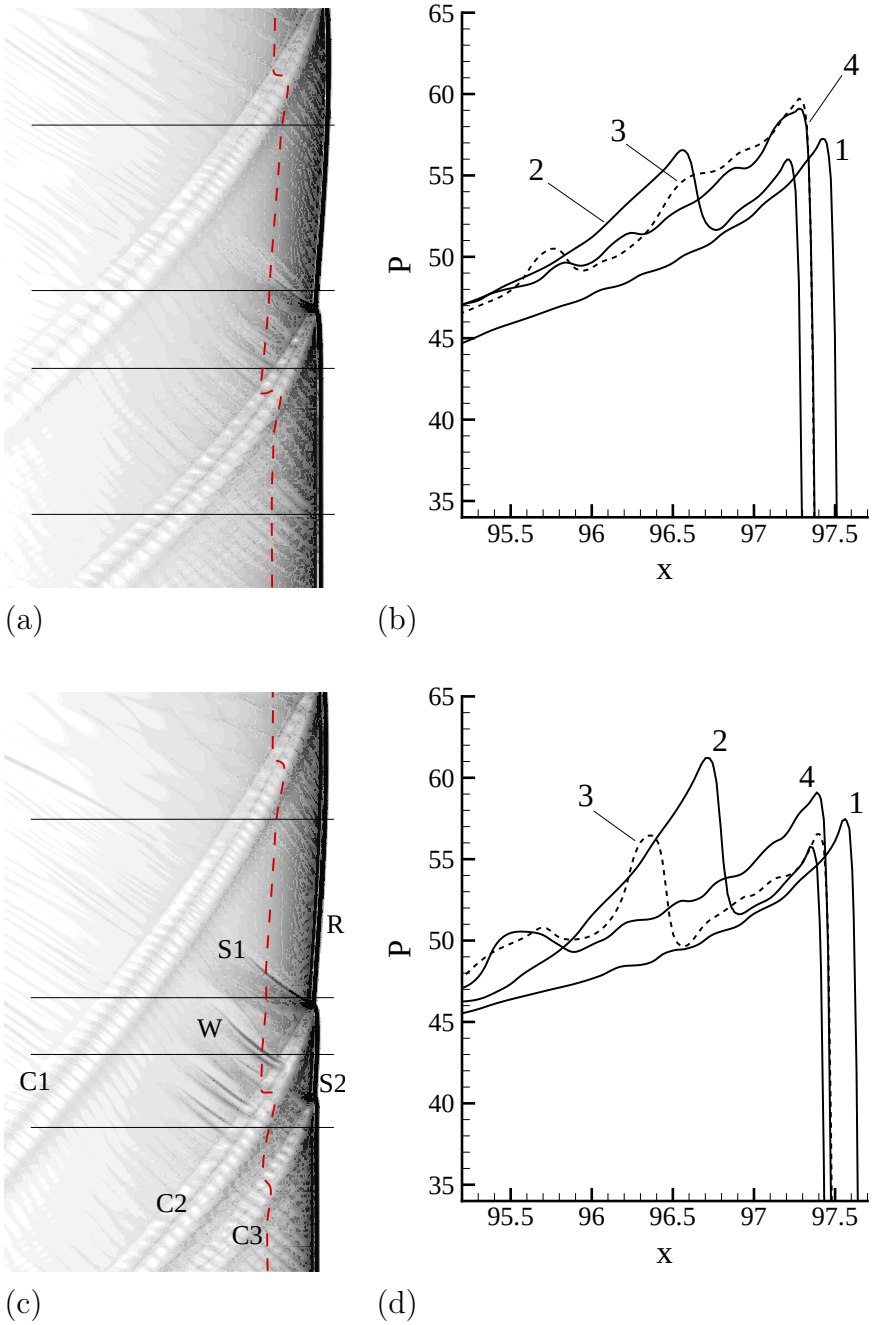

Figure 6.7: Computational cases A and B, detail of the solution (schlieren image), left, and pressure diagram, right. The four horizontal lines (numbered 1, top, to 4, bottom) mark where data have been extracted to draw the pressure plots. The dashed line on the left is the locus of 50% reaction completion locus. Frames (a) and (b); order 1 reaction. Frames (c) and (d); order 2 reaction.

where the pressure field has been sampled. The schlieren images are on the same scale and measure $7\,\Delta_{1/2}$ in width. The dashed lines, corresponding to the 50% reaction completion locus, provide a visual indication of the actual extent of the reaction zone in the schlieren images.

Two distinct waves, S1 and W, are observed in case B, at an interval of about one half-reaction length between each other, whereas in case A there is only one wave. The shock S1 appears in slice 2 of both frames and is part of the triple shock structure at the front. The pressure decrease behind it in frames (b) and (d) corresponds to an expansion due to energy release associated with the chemical reaction. The shock W is the most relevant to our discussion since it appears only in case B. At the detonation wavefront, the effect of W is to generate a second transverse wave (S2), with a corresponding contact discontinuity (C3). We believe that this situation is analogous to the one seen in super-critical diffraction simulations, see Fig. 4.8. At later times, S2 steepens to form a shock and new disturbances are amplified behind it. The growth of S2 is studied in Section 6.5. The value of this comparison between cases A and B is to show that the amplification predicted by the theory and shown in the diagram in Fig. 6.5 is actually verified in our numerical simulations.

In the second group of simulations, Fig. 6.8, the detonation configuration is more complex. The number and strength of the transverse shocks is roughly the same for cases C and D, and the only qualitative difference between the two computations is the appearance of an isolated kink (k) at the Mach stem in frame (a). Note that, for the order-one reaction and $\gamma = 1.22$, the neutral limit is $\zeta_T = 3.583$, and therefore case C, slightly below the neutral curve, should not show wave amplification according to the model for a planar ZND wave in Section 6.3.

In Fig. 6.9 we plot the contours of the sonic parameter ω,

$$\omega \cong c^2 - (D_{CJ} - u_x)^2 \,, \tag{6.13}$$

for the cases A, B, and C. The scales of the corresponding frames (a) to (c) are the same as in figures 6.7 and 6.8. $D_{CJ} - u_x$ approximates the flow velocity in the

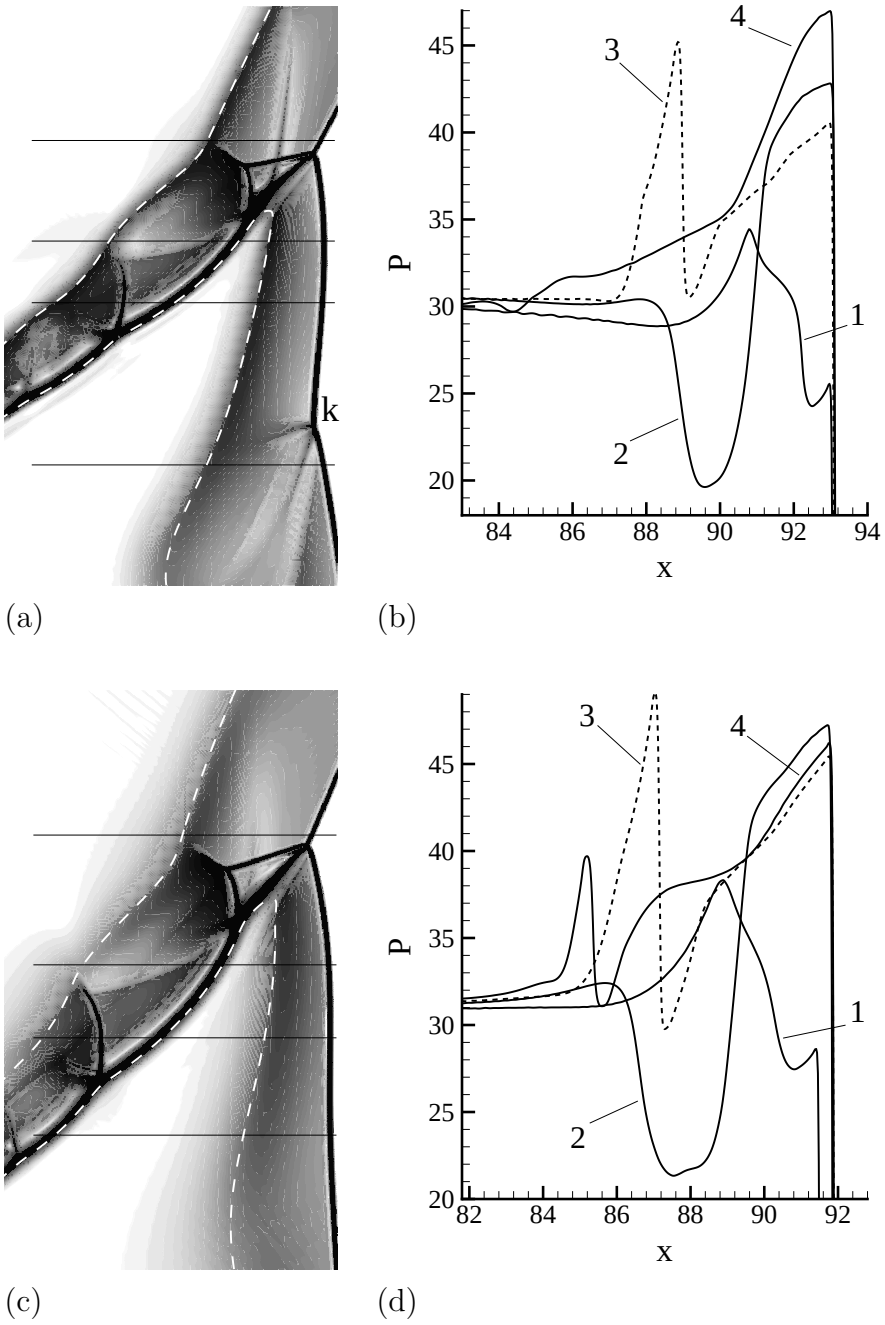

Figure 6.8: Computational cases C and D, detail of the solution (schlieren image), left, and pressure diagram, right. The four horizontal lines (numbered 1, top, to 4, bottom) mark where data have been extracted to draw the pressure plots. The dashed line on the left is the locus of 50% reaction completion locus. Frames (a) and (b); order 1 reaction. Frames (c) and (d); order 2 reaction.

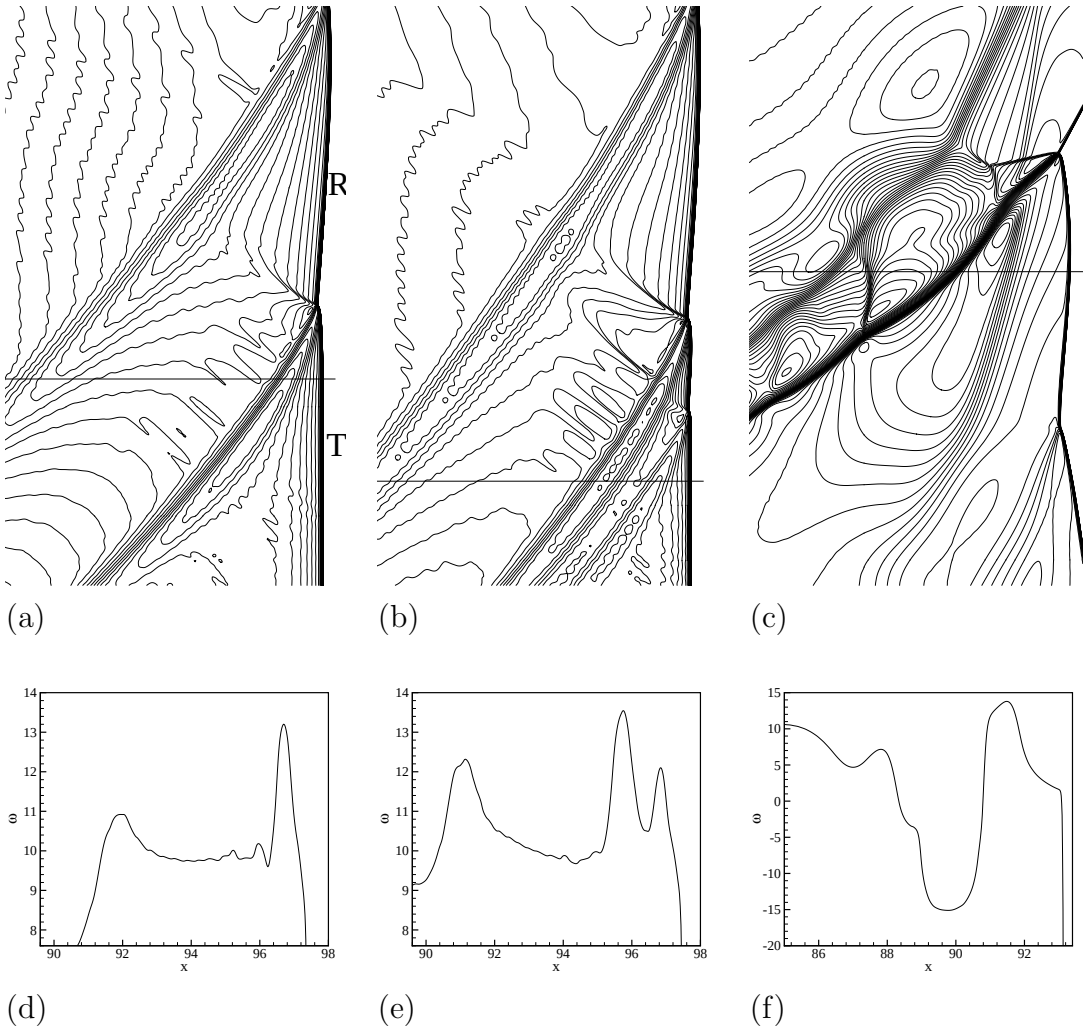

Figure 6.9: Frames (a) to (c): contours of ω, Equation (6.13), for cases A, B, C. The contours start at the value -20 and are spaced by 0.50. The plot scale is the same used for the schlieren images in Fig. 6.7 and Fig. 6.8. Frames (d) to (f): plot of s for cases A, B, C along slices taken at the locations shown in the upper diagrams.

shock reference frame. For case A (frames (a) and (d)), the velocity components do not change much across the contact discontinuity. However, the flow processed by the shock R has a slightly less degree of reaction than the flow processed by T. This corresponds to a larger density and, since the pressure is the same on both sides of the contact discontinuity, to a smaller sound speed c. This results in a local maximum of ω occurring at the contact discontinuity. The discontinuity is smoothed by the solver, and Equation (6.4) still holds, at least in an approximate sense, but for $Z \neq Z_{\|}$. In case B, comparison of Fig. 6.7 (c) and Fig. 6.9 (b) shows that the contacts C2 and C3 correspond to acoustic channels for the propagation of disturbances. A similar result is found for case C. The connection with the super-critical diffraction in Fig. 4.9 is therefore the following. Once the first reflected shock is formed, the corresponding contact discontinuity separates flows with a slight difference in the degree of reaction. This difference is sufficient to generate a local peak in the sonic parameter, which acts as a channel for disturbances traveling transversely to the main front. For an order $n_r = 2$ reaction, even a small activation energy produces a sufficient wave amplification to overcome wave spreading. Once the first compressive wave has steepened to a shock and reached the main front, a new contact discontinuity appears, which in turn acts as an acoustic channel. In Fig. 4.9, this cyclic process has already taken place several times and we count five distinct transverse shocks.

6.5 Growth of transverse waves

We conclude this chapter by examining the growth of transverse waves at the leading detonation front. These waves result from the amplification of small acoustic disturbances described in the previous section. One of such transverse waves is labeled S2 in Fig. 6.7 (c) for case B. To study its growth in time, we take a slice of the computational domain in the y direction at ten different times. Each slice is extracted at an arbitrary fixed location ($\bar{Z} = 0.28$) close to the undisturbed shock. These slices are arranged in a space-time diagram in Fig. 6.10. The plot shows the leading transverse shock LS (not shown in Fig. 6.7 (c)), the rarefaction wave R, the transverse shock

S1 and the compression wave S2. To show the growth of S2, only the last part of each data set in frame (a) is plotted in Figure 6.10 (b). In this diagram, at $y = 10$ the wave has just formed in the wake of S1. By the last slice at $y = 27$, S2 has grown by an order of magnitude and a new disturbance is forming in its wake. The schlieren image in Fig. 6.7 (c) corresponds to this later time. Overall, the pressure plot shows a more than linear increase in peak amplitude, P_M, between each two consecutive data sets. When plotted in a log-linear diagram, P_M is found to grow almost linearly in time with respect to an appropriate reference pressure. If the first data point (corresponding to the formation of S2) is excluded, least-squares fitting of P_M to the exponential function gives

$$P_M = 57.24 + 0.1826\ \mathrm{e}^{\,0.47\,t}. \tag{6.14}$$

This curve is plotted in Fig. 6.11 together with the data points.

Even if exponentially growing in Fig. 6.10 (b), the pressure increment ΔP due to S2 is rather small compared to the ZND pressure at $\bar{Z}$. Thus, we can still use the results of acoustics for the amplification of a ray bundle under the assumption that S2 is sufficiently small to be treated as an isentropic perturbation. In this problem however, we need to consider a strip at $Z \neq Z_{\parallel}$, and so we cannot properly evaluate the wave spread in Equation (6.9). The inequality (6.10), evaluated for $c(\bar{Z})$, is still satisfied since Λ and $c(\bar{Z})$ are of order unity. However, $K(\bar{Z})/2 = 0.094$, much smaller than the exponential coefficient in Equation (6.14). A larger coefficient $\bar{K}/2$ is found by assuming that the wave does not spread at all,

$$\bar{K} = 2\,\frac{\gamma - 1}{c_p^2}\,Q\,\left.\frac{\mathrm{D}Z}{\mathrm{D}t}\right|_{\bar{Z}}\,[\zeta\,(\gamma - 1) + n]\,. \tag{6.15}$$

For $n_r = 2$ and $\zeta = 0$, we find $\bar{K}/2 = 0.92$, indicating that a certain amount of wave spreading should be taken into account.

This example shows that acoustic theory provides a qualitative account of the amplification of high-frequency disturbances and their consequent growth to trans-

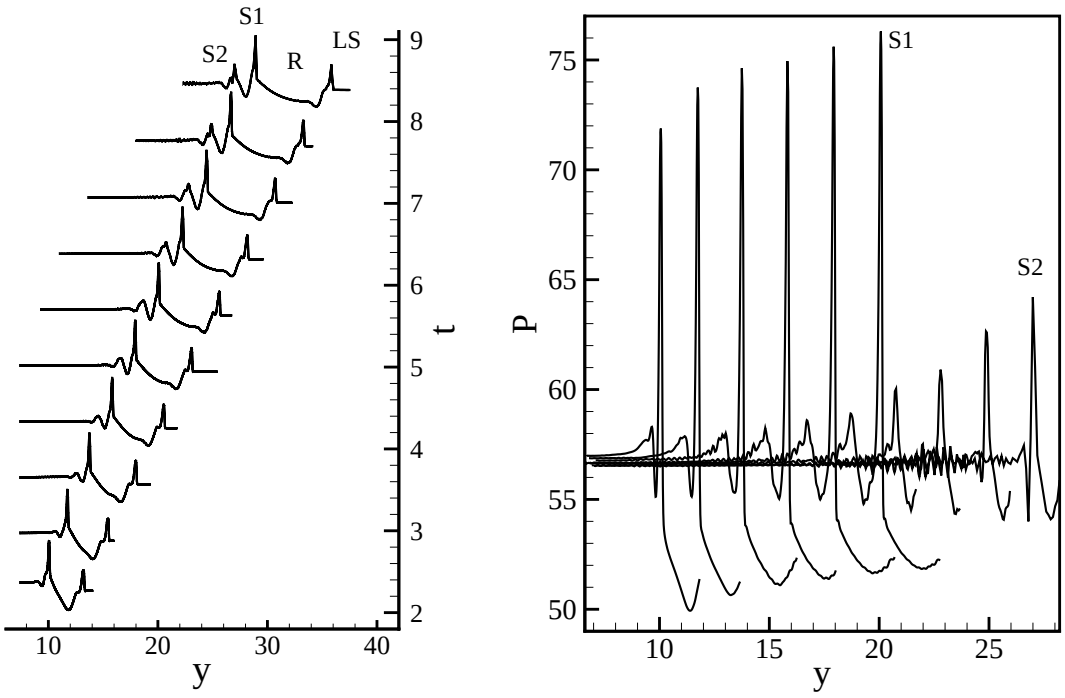

(a) (b)

Figure 6.10: Space-time diagram of the transverse wave system for pressure (a), and superposition of the same data showing the growth of wave S2 (b).

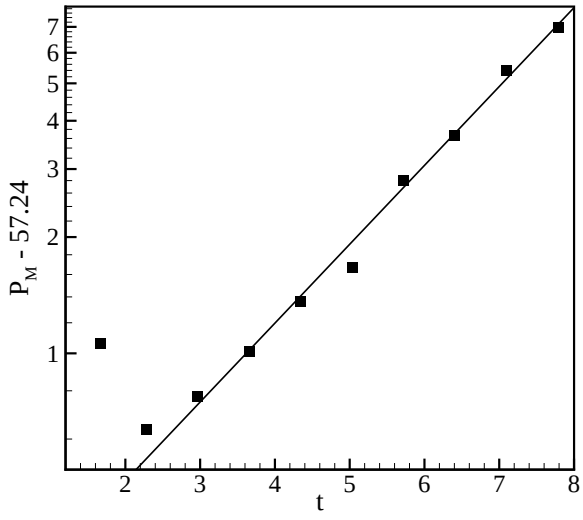

Figure 6.11: Pressure peak vs. time for S2 wave. Symbols: peak value of S2 in the pressure diagrams of Fig. 6.10 (b). Solid line: least-squares fitting, Equation (6.14).

verse shocks. Large-amplitude nonlinear effects soon dominate the further growth of the wave, but the basic propagation mechanism along contact discontinuities can be related to the sonic parameter ω. The determination of the final wave spacing in this channel problem is beyond the scope of this study. The work by Majda (1987) starts from the same concept of acoustic wave trapping, and develops a high-frequency nonlinear acoustic theory to predict the regular spacing of the Mach stems embedded in the front of a detonation cellular structure.

Chapter 7

Summary

In this work we have identified modes of detonation diffraction that depend on the activation energy of a single-step, irreversible, Arrhenius reaction model. The initial solution is a planar ZND detonation wave propagating in a channel with an abrupt area increase. To examine the three different outcomes of detonation diffraction (sub-critical, near-critical and super-critical diffraction), we carried out direct numerical simulations with a fixed channel half-width H (normalized by the CJ half-reaction zone length), while varying the activation energy in the Arrhenius reaction model. The reactive Euler equations, formulated for a perfect gas mixture, were integrated by operator splitting, using a Roe's approximate Riemann solver for the convective flux and a predictor–corrector scheme for the chemical source term. Computations were executed in parallel on a uniform grid by a cluster of 48 processors. We performed a set of coarse resolution simulations for 8 values of reduced activation energy, followed by a set of high resolution simulations for three selected cases with reduced activation energies of 1, 3.5, and 4.15.

We found three regimes of diffraction that resemble the cases observed in experiments. With zero or small normalized activation energy ($0 < \theta_{CJ} \leq 1$), the reaction rate is essentially independent from the thermodynamic state, so that the reaction zone length is unaffected by the shock velocity. Since the reaction rate is nearly constant, the shock front will always accelerate after diffraction. We find that the transient wavefront dynamics, due to the propagation and reflection of unsteady rarefaction waves generated by the area change, dies out after a distance of about $6\,H$

from the corner, and that the detonation can be treated as quasi-steady, quasi-one-dimensional after that point. This successful detonation transmission is similar to the super-critical case that is observed in diffraction experiments (see Figures 1.6 and 4.5).

As the detonation front is diffracting, a train of weak transverse waves develops near the corner and moves toward the axis of symmetry of the channel (Fig. 4.9). The first wave is the reflected shock that forms at the corner as a result of the adjustment to the wall boundary conditions. This shock is followed by a train of acoustic disturbances that propagate in an acoustic channel embedded in the reaction zone. Compression waves are amplified by the energy release due to the chemical reaction and become transverse shocks at the detonation front. The newly formed contact discontinuity provides in turn a channel for the propagation of more acoustic disturbances. In this process, transverse wave spacing increases by an order of magnitude from the initial half-reaction length. This mechanism of transverse wave propagation and amplification is studied in a simpler problem where a ZND-CJ planar detonation moves in a channel over a small obstacle. Simulations of this problem show a qualitative similarity with the results obtained for the diffracting detonation (Fig. 6.7). The initial amplification of acoustic disturbances agrees favorably with the mechanism proposed by Strehlow and Fernandes (1965) and Barthel and Strehlow (1966).

When the activation energy is larger, $3.75 \geq \theta_{CJ}$, the reaction rate is strongly dependent on the thermodynamic state so that the reaction zone length increases rapidly when the shock speed decreases. This causes the reaction zone to decouple from the shock wave, and the reaction rate to essentially drop to zero, after a short distance from the corner vertex. The detonation fails completely and the resulting flow is essentially a non-reactive shock wave (Fig. 4.14). This is similar to the case of sub-critical diffraction that is observed in diffraction experiments where the tube is smaller than the critical size needed for successful detonation transmission (Fig. 1.7). The shock decay rate of this case is found to be only qualitatively similar to the decay rate of a cylindrical blast.

For $2.5 \leq \theta_{CJ} \leq 3.5$, the reaction rate is moderately dependent on the thermody-

namic state. The reaction zone length increases as the shock decays but the accelerating effects of energy release are sufficient to cause the reaction zone length to decrease in an abrupt fashion. This ultimately causes the appearance of a re-initiation event near the wall that propagates back to the axis (see Figures 4.22 and 4.23). This is similar to the case of critical diffraction that is observed in diffraction experiments where the tube is comparable to the critical size needed for successful detonation transmission (Fig. 1.8). Re-initiation occurs through the interplay of transverse rarefaction waves with the accelerating detonation front near the channel axis. This results in shock folding and in the formation of a transverse shock that is kinked at a second triple point interior to the detonation (Fig. 4.25). Similar waves have been observed in recent simulations of cellular structures in reactive mixtures (Sharpe 2001; Inaba and Matsuo 2001). The kink is due to the high-pressure region that forms when the transverse shock processes pockets of compressed and unburnt fuel behind the partially decoupled detonation front. Multiple systems of transverse waves eventually overlap, thus enhancing the reactivity behind the leading wavefront. Where the front is completely recoupled, weak transverse waves appear with the spacing observed in the super-critical diffraction case (Fig. 4.26).

We extended the technique used by Eckett et al. (2000) to record the time derivative of temperature along the path of particles that are close to ignition failure. This approach consists in injecting massless particles as probes in the flow field. When particles experience long ignition delays, the temperature decreases immediately after the passage of the shock. The delayed ignition reduces the energy release behind the shock, so the shock further decelerates. Thus, ignition failure and ultimately local decoupling of the shock front from the reaction zone occur if the Lagrangian derivative of temperature $\mathrm{D}T/\mathrm{D}t$ vanishes at post-shock conditions. This hypothesis, first advanced by Eckett et al. (2000), is applied at the axis of symmetry of the diffracting detonation, where the re-initiation first starts in the near-critical case. This provides a global criterion for detonation diffraction failure (Schultz 2000).

Further analysis of a fluid element history is performed by decomposing $\mathrm{D}T/\mathrm{D}t$ in terms depending from local front curvature, transverse flow divergence, chemical

energy release, and flow field partial time derivatives (in the shock based reference system). This latter term is related to the flow field unsteadiness, as seen by a particle element. It always appears as a negative forcing term for a decelerating flow. This term becomes dominant for particles with long ignition delays, while curvature and transverse divergence contributions are very small. The role of unsteadiness is consistent with the observation of very long transients in near-critical and super-critical diffractions. Thus, for particles that are close to ignition failure, the increase in temperature due to energy release Q at a rate of order k is balanced by the decrease due to flow unsteadiness behind the shock. With shock decay rate provided (very crudely) by the blast decay model, this critical balance can be written as

$$\frac{H\,k}{D_{CJ}}\,\frac{Q}{D_{CJ}^2} = \exp\left(1.78\,\theta_{CJ}\right)\,\frac{9\,\tan\alpha}{3-\gamma}\,\frac{(\gamma-1)^2}{(\gamma+1)^3}\,,$$

where α is the disturbance angle of the head of the rarefaction. By substituting the values of α, Q, k, H, D_{CJ}, and specific heat ratio γ, we find the critical normalized activation energy $\theta_{CJ_c} = 4.0$, above which re-initiation does not occur. This value is in good agreement with our parametric study. At $\theta_{CJ} = 3.75$, a large transverse wave is still observed in our simulation, but it proves insufficient for re-initiation. At $\theta_{CJ} = 4.0$, no transverse waves are formed. In both cases, the axial shock decay is monotonic. Clearly, this result addresses the purely gasdynamic quenching mechanisms, since our simulations do not include a detonation cellular structure in the initial conditions. Further work in this direction would be to simulate a cellular structure in the channel to verify if our current results provide at least a lower bound for critical diffraction. Our parametric study should also be completed by a comparison with simulations implementing a detailed reaction mechanism, to see how the formation of strong and weak transverse waves is affected. Finally, even if the present computations involved week-long simulations and stretched to a limit the capability of analyzing large volumes of data, future extensions of this work should also include the effects of three-dimensionality in the re-initiation mechanism we presented.

Bibliography

Akbar, R. (1997). *Mach Reflection of Gaseous Detonations*. Ph.D. thesis, Rensselaer Polytechnic Institute.

Arienti, M., P. Hung, E. O. Morano, and J. E. Shepherd (2002). A level set approach to Eulerian-Lagrangian coupling. In print, J. Comput. Phys.

Aslam, T. D., J. B. Bdzil, and L. Hill (1998). Extension to DSD theory: analysis of pbx 9502 rate stick data. In *11th Symp. (Intl) on Detonation*, pp. 21–29. Office of Naval Research.

Aslam, T. D. and D. S. Stewart (1999). Detonation shock dynamics and comparisons with direct numerical simulations. *Combust. Theor. Model. 3*, 77–101.

Barthel, H. O. and R. A. Strehlow (1966). Wave propagation in one-dimensional reactive flows. *Phys. Fluids A 9*, 1896–1907.

Bartlmä, F. (1990). The propagation of detonation waves in channels of varying cross-section. *J. Fluid Mech. 218*, 225–238.

Bdzil, J. B. and T. D. Aslam (2000). Detonation front models: theories and methods. LA-UR- 00-942, Los Alamos National Laboratory.

Bdzil, J. B. and D. Stewart (1989). Modeling two-dimensional detonations with detonation shock dynamics. *Phys. Fluids A 1*, 1261–1267.

Desbordes, D. (1988). Transmission of overdriven plane detonations: Critical diameter as a function of cell regularity and size. *Prog. Astronaut. Aeronaut. 114*, 170–185.

Eckett, C. A. (2001). *Numerical and analytical studies of the dynamics of gaseous detonations*. Ph.D. thesis, California Institute of Technology.

Eckett, C. A., J. J. Quirk, and J. E. Shepherd (2000). The role of unsteadiness in direct initiation of gaseous detonations. *J. Fluid Mech. 421*, 147–183.

Edwards, D. H., G. O. Thomas, and M. A. Nettleton (1979). The diffraction of a planar detonation wave at an abrupt area change. *J. Fluid Mech. 95*, 79–96.

Erpenbeck, J. J. (1966). Detonation stability for disturbances of small transverse wavelength. *Phys. Fluids A 9*, 1293–1306.

Fickett, W. and W. C. Davis (1979). *Detonation*. University of California Press.

Glaister, P. (1988). An approximate linearised Riemann solver for the Euler equations for real gases. *J. Comput. Phys. 74*, 382–408.

Guirao, C. M., R. Knystautas, and J. H. Lee (1987). A summary of hydrogen-air detonation experiments. Technical Report SAND87-7128, Sandia National Laboratories.

Harten, A. (1983). High resolution schemes for hyperbolic conservation laws. *J. Comput. Phys. 49*, 357–393.

He, L. and P. Clavin (1994). On the direct initiation of gaseous detonations by an energy source. *J. Fluid Mech. 277*, 227–248.

Hoffmann, C. M. (1989). *Geometric and solid modeling, an introduction*. Morgan Kaufmann Publishers, Inc.

Inaba, K. and A. Matsuo (2001). Cellular structure of planar detonations with a detailed chemical reaction model. *AIAA Journal 0480*, 1–11.

Jones, D. A., G. Kemister, E. S. Oran, and M. Sichel (1996). The influence of cellular structure on detonation transmission. *Shock Waves 6*, 119–129.

Jones, D. A., G. Kemister, N. A. Tonello, E. S. Oran, and M. Sichel (2000). Numerical simulation of detonation reignition in H_2–O_2 mixtures in area expansions. *Shock Waves 10*, 33–41.

Jones, D. A., M. Sichel, R. Guirguis, and E. S. Oran (1991). Numerical simulation of layered detonations. In *Prog. Astronaut. Aeronaut.*, pp. 202–219.

Jones, D. A., M. Sichel, and E. S. Oran (1995). Reignition of detonation by reflected shocks. *Shock Waves 5*, 47–57.

Jones, D. A., M. Sichel, E. S. Oran, and R. Guirguis (1990). Detonation transmission in layered explosives. In *23rd Symp. (Intl) on Combustion*, pp. 1805–1811. The Combustion Institute.

Kaneshige, M. J. (1999). *Gaseous Detonation Initiation and Stabilization by Hypervelocity Projectiles*. Ph.D. thesis, California Institute of Technology.

Kee, R. J., F. M. Rupley, and J. A. Miller (1989). CHEMKIN-II: A Fortran chemical kinetics package for the analysis of gas-phase chemical kinetics. Technical Report SAND89-8009, Sandia National Laboratories.

Klein, R., J. C. Krok, and J. E. Shepherd (1995). Curved quasi-steady detonations: Asymptotic analysis and detailed chemical kinetics. Technical Report FM95-04, GALCIT.

Knystautas, R., J. Lee, and C. Guirao (1982). The critical tube diameter for detonation failure in hydrocarbon-air mixtures. *Combust. Flame 48*(1), 63–83.

Konnov, A. A. (1998). Detailed reaction mechanism for small hydrocarbon combustion. http://homepages.vub.ac.be/ akonnov/.

Korobeinikov, V. P. (1991). *Problems of Point-Blast Theory*. American Institute of Physics.

Lee, H. I. and D. S. Stewart (1990). Calculation of linear detonation instability: One-dimensional instability of plane detonation. *J. Fluid Mech. 216*, 103–132.

Lee, J. H. S. (1996). On the critical diameter problem. In J. R. Bowen (Ed.), *Dynamics of Exothermicity*, pp. 321–336. Netherlands: Gordon and Breech Science Publishers.

Li, C. and K. Kailasanath (2000). Detonation transmission and transition in channels of different sizes. In *28th Symp. (Intl) on Combustion*, pp. 603–609. The Combustion Institute.

Li, H. and B. Ben-Dor (1998). A modified CCW theory for detonations waves. *Combust. Flame 113*, 1–12.

Liu, J. C., J. Liou, M. Sichel, and C. W. K. J. A. Nichols (1987). Diffraction and transmission of a detonation into a bounding explosive layer. In *21st Symp. (Intl) on Combustion*, pp. 1639–1647. The Combustion Institute.

Liu, J. C., M. Sichel, and C. W. Kauffmann (1988). The lateral interaction of detonating and detonable gas mixtures. *Prog. Astronaut. Aeronaut. 114*, 264–283.

Majda, A. J. (1987). Criteria for regular spacing of reacting Mach stems. In *Proc. Natl. Acad. Sci. USA*, pp. 6011–6014. Applied Mathematical Sciences.

Menikoff, R., K. S. Lackner, and B. G. Bukiet (1996). Modeling flows with curved detonation waves. *Combust. Flame 104*, 219–240.

Mitrofanov, V. and R. Soloukhin (1965). The diffraction of multifront detonation waves. *Soviet Physics-Doklady 9(12)*, 1055–1058.

Moen, I., S. Murray, D. Bjerketvedt, A. Rinnan, R. Knystautas, and J. Lee (1982). Diffraction of detonation from tubes into a large fuel-air explosive cloud. In *19th Symp. Int. Combust. Proc.*, pp. 635–644.

Murray, S. B. and J. H. S. Lee (1983). On the transformation of planar detonation to cylindrical detonation. *Combust. Flame 52*, 269–298.

Oran, E. S., J. Boris, D. A. Jones, and M. Sichel (1993). Ignition in a complex mach structure. In *Prog. Astronaut. Aeronaut.*, Volume 153, pp. 241–252.

Oran, E. S., D. A. Jones, and M. Sichel (1992). Numerical simulations of detonation transmission. *Proc. R. Soc. Lond.* A *436*, 267–297.

Pantow, E., M. Fisher, and T. Kratzel (1996). Decoupling and recoupling of detonation waves associated with sudden expansion. *Shock Waves 6*, 131–137.

Parashar, M., J. Browne, and et al. (1997). A common data management infrastructure for adaptive algorithms for PDE solutions. In *Supercomputing 1997*.

Parashar, M. and J. C. Browne (2000, January). *System engineering for high performance computing software: The HDDA/DAGH Infrastructure for implementation of parallel structured adaptive mesh refinement*, Volume 117 of *IMA: Structured Adaptive Mesh Refinement (SAMR) Grid Methods*, pp. 1–18. Springer-Verlag.

Pierce, A. (1981). *Acoustics: An Introduction to Its Physical Principles and Applications*. New York: McGraw-Hill.

Press, W. H., S. A. Teukolsky, W. T. Vetterling, and B. P. Flannery (1992). *Numerical recipes: the art of scientific computing*, pp. 747–752. Cambridge University Press.

Reynolds, W. C. (1986). The element potential method for chemical equilibrium analysis: Implementation in the interactive program STANJAN. Technical report, Stanford University, Dept of Mech. Engng.

Roe, P. L. (1986). Characteristic-based schemes for the Euler equations. *Ann. Rev. Fluid Mech. 18*, 337–365.

Schultz, E. (2000). *Detonation diffraction trough an abrupt area expansion*. Ph.D. thesis, California Institute of Technology.

Sharpe, G. J. (2001). Transverse waves in numerical simulations of cellular detonations. *J. Fluid Mech. 447*, 31–51.

Shepherd, J. E. (1986). Chemical kinetics of hydrogen–air–diluent detonations. *Prog. Astronaut. Aeronaut. 106*, 263–293.

Shepherd, J. E., I. O. Moen, S. B. Murray, and P. A. Thibault (1986). Analyses of the cellular structure of detonation. In *21st Symp. (Intl) on Combustion*, pp. 1649–1658. The Combustion Institute.

Skews, B. W. (1967). The shape of a diffracting shock wave. *J. Fluid Mech. 29*, 297–304.

Snir, M., S. W. Otto, S. Huss-Lederman, D. W. Walker, and J. Dongarra (1996).

MPI: The Complete Reference. Scientific and engineering computation. Cambridge, Mass.: MIT Press.

Stewart, D. S. and J. B. Bdzil (1988). The shock dynamics of stable multi-dimensional detonation. *Combust. Flame 72*, 311–323.

Stewart, D. S. and J. Yao (1998). The normal detonation shock velocity-curvature relationship for materials with nonideal equation of state and Multiple turning points. *Combust. Flame 113*, 224–235.

Strehlow, R. A. and F. D. Fernandes (1965). Transverse waves in detonations. *Combust. Flame 9*, 109–119.

Thompson, P. A. (1988). *Compressible–fluid dynamics*. Rensselaer Polytechnic Institute.

Van Dyke, M. (1982). *An album of fluid motion* (1st ed.). Parabolic Press, Stanford, Calif.

Whitham, G. B. (1974). *Linear and nonlinear waves*. New York Wiley.

Wilkinson, B. and M. Allen (1999). *Parallel programming, techniques and applications using networked workstations and parallel computers*. Upper Saddle River, New Jersey 07458: Prentice Hall.

Williams, D. N., L. Bauwens, and E. S. Oran (1996). Detailed structure and propagation of three-dimensional detonations. In *26th Symp. (Intl) on Combustion*, pp. 2991–2998. The Combustion Institute.

Xu, S., T. Aslam, and D. S. Stewart (1997). High resolution numerical simulation of ideal and non-ideal compressible reacting flows with embedded internal boundaries. *Combust. Theor. Model. 1*, 113–142.

Yao, J. and D. S. Stewart (1995). On the normal shock velocity–curvature relationship for materials with large activation energy. *Combust. Flame 100*, 519–528.

Yao, J. and D. S. Stewart (1996). On the dynamics of multi-dimensional detonation. *J. Fluid Mech. 309*, 225–275.

Zel'dovich, I. B., S. M. Kogarko, and N. N. Simonov (1956). An experimental investigation of spherical detonation of gases. *Sov. Phys. Tech. Phys. 1*(8), 1689–1713.

Appendix A

Convergent evaluation of curvature

The wavefront curvature is computed from a discrete set of shock positions obtained at time t by the shock-tracking technique described in Section 3.3. If the shock is described in a parametric form, $\bar{x}\,(q)$, $\bar{y}(q)$, then

$$\kappa = \frac{\bar{x}'\,\bar{y}'' - \bar{y}'\,\bar{x}''}{(\bar{x}'^{\,2} + \bar{y}'^{\,2})^{3/2}}, \tag{A.1}$$

where $'$ and $''$ denote first- and second-order derivatives with respect to the parameter q. At the channel axis of symmetry, we take $q = y$ so that

$$\kappa_a = -\frac{\mathrm{d}^2\bar{x}}{\mathrm{d}y^2}. \tag{A.2}$$

Likewise, at the wall, $q = x$, and

$$\kappa_w = \frac{\mathrm{d}^2\bar{y}}{\mathrm{d}x^2}. \tag{A.3}$$

When the expressions above are discretized, derivatives of order higher than one may not converge under grid refinement, since the estimated shock position is affected by error. As an example, we discretize the second-order derivative in Equation (A.2) as a centered-difference scheme at the grid node j. For generality, let us skip h grid points from j in both directions (Fig. A.1), then,

$$\frac{\mathrm{d}^2\bar{x}}{\mathrm{d}y^2} = \frac{\bar{x}_{j+h} - 2\bar{x}_j + \bar{x}_{j-h}}{h^2\Delta y^2} + c\,h^2\Delta y^2. \tag{A.4}$$

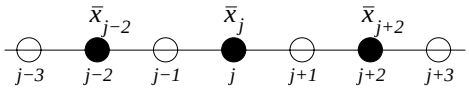

Figure A.1: Point selection for computing a second-order derivative. Here $h = 2$.

In Equation (A.4), $\bar{x}_j$ is the tracked shock position along a slice passing by grid point y_j; Δy is the grid spacing between two consecutive points; and $c\,h^2\Delta y^2$ is the truncation error. Note that, in this specific example, $\bar{x}_{j+h} = \bar{x}_{j-h}$ because of symmetry.

By varying h, we want to verify whether Equation (A.4) provides a convergent result as the grid is refined. The case we consider is a corner-turning problem without chemical reaction, at an initial Mach number $M_0 = 7$ in a perfect gas at $\gamma = 1.2$. We compute the curvature at the axis of symmetry of the problem. Whitham's shock dynamics provides a peak curvature value $\kappa_a\, H = 0.6945$ for the strong shock limit case (dashed line in Fig. A.2). We start with a coarse mesh with 40 grid points in the channel half-width and we solve the same problem over finer meshes, with a refinement ratio R. We compute the curvature at the channel axis by using Equation (A.4). By keeping h constant while R increases, κ is evaluated with points that are progressively closer to the axis of symmetry. In Fig. A.2, we take $h = 4$ and mark the resulting data points with the ▲ symbol (fixed spacing). The sequence of values appears to diverge for decreasing Δy, whereas we expect a finite value of curvature at the axis. The divergence is due to errors in the tracked shock position.

We now make h dependent on the grid refinement. One choice is to set h/R equal to a constant, so that the curvature is evaluated with points at fixed distance from y_j as the grid is refined (this curve is marked by the ♦ symbol). A better approach consists in modeling the error associated with $\bar{x}_j$. Aslam et al. (1998) assume that the tracked shock position is affected by $\mathcal{O}(\Delta y)$ errors, so that Equation (A.4) takes an additional term,

$$\frac{d^2\bar{x}}{dy^2} = \frac{\bar{x}_{j+h} - 2\bar{x}_j + \bar{x}_{j-h} + \bar{c}\,\Delta y}{h^2\Delta y^2} + c\,h^2\Delta y^2. \tag{A.5}$$

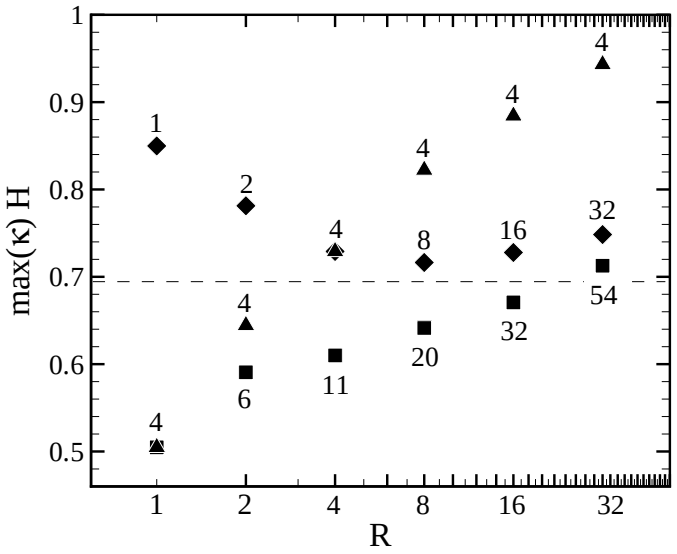

Figure A.2: Convergence study for the computed maximum value of curvature as a function of grid refinement. ■ grid-adaptive spacing; ♦ fixed point; ▲ fixed spacing.

In general, the constant of proportionality $\bar{c}$ is unknown, since it depends on the details of the tracking algorithm and, possibly, on the flow solver. With this model, we recover the result that a second-order centered finite difference scheme with fixed h would diverge as Δy goes to zero. To minimize the term

$$\bar{c}/\left(h^2\Delta y\right) + c\left(h\,\Delta y\right)^2 \tag{A.6}$$

in Equation (A.5), we differentiate it with respect to Δy and find that $h^4\Delta y^3$ must be a constant. Thus, for two grids with spacings Δy_l and Δy_{l-1}, the integer numbers h_l and h_{l-1} should scale as

$$\frac{h_l}{h_{l-1}} = \mathrm{Int}\left(\frac{\Delta y_{l-1}}{\Delta y_l}\right)^{3/4} = \mathrm{Int}\left(R^{3/4}\right), \tag{A.7}$$

The Int( ) operator indicates that the closest integer to the argument must be taken. Thus, as the points in the stencil are getting closer when the mesh is refined, an increasing number of points can be skipped to average the error associated with shock tracking. This procedure assures a convergence, albeit less than linear (the term

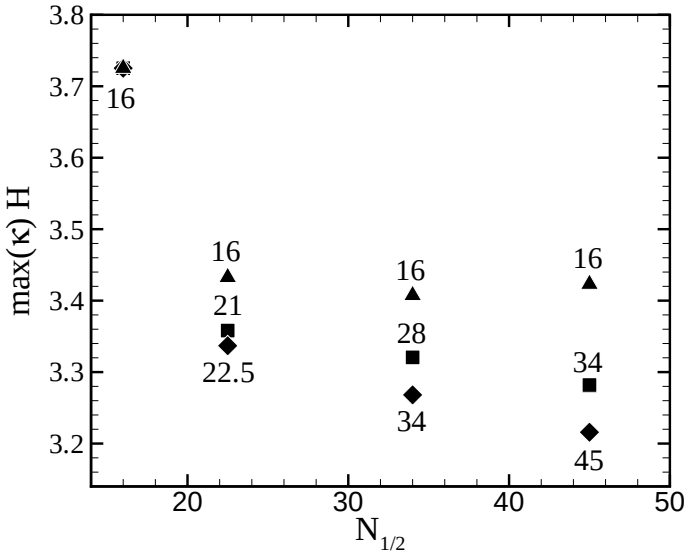

Figure A.3: Convergence study for the computed maximum value of curvature as a function of grid resolution $N_{1/2}$ (number of cells in reference half-reaction zone). ■ grid-adaptive spacing; ♦ fixed point; ▲ fixed spacing.

(A.6) vanishes as $\Delta y^{\,0.5}$). Equation (A.7) can be generalized to a finite difference with truncation error of order $\mathcal{O}\left(\Delta y^m\right)$,

$$\frac{h_l}{h_{l-1}} = \mathrm{Int}\left(\mathrm{R}^{-\frac{1+\mathrm{m}}{2+\mathrm{m}}}\right). \tag{A.8}$$

Points computed with grid-adaptive spacing are displayed in Fig. A.2 as square symbols. The number above each symbol is the stencil spacing h from Equation (A.7). The starting point on the coarsest grid has $h = 4$. This set of values approaches the reference curvature very slowly, and the last data point overshoots it, indicating that the sequence is far from converging. The fixed-point spacing reaches the reference value more quickly, but after $R = 8$ the estimate of κ is worse. The same qualitative result can be observed in Fig. A.3, where the computational setting corresponds to a reactive case (case $\theta_{CJ} = 3.5$), and no reference solution is available. Values $h = 16$ and $h = 21$ were used in analyzing the results from the low- and high-resolution simulations in Chapters 4 and 5.

Appendix B

Effect of corner radius of curvature

To avoid the singularity associated with the presence of a sharp turning corner, the corner vertex is rounded with radius of curvature r_c. In this section, we investigate the effect of a finite r_c on the wall detonation velocity, D_w. The result of this study is displayed in Fig. B.1, with r_c decreasing from the reference value 1 (radius of curvature equal to $\Delta_{1/2}$) to 0.2. In the four cases, the same number of grid cells in the reference half-reaction zone length was used ($N_{1/2} = 64$). As r_c decreases, the initial drop in D_w grows larger, but it is immediately followed by a larger partial recovery near the corner. Overall, the detonation velocity assumes essentially the same value for the tested range of radii at a distance $10\,\Delta_{1/2}$. As the simulation advances beyond this point, no other significant differences can be observed in the plot of D_w versus distance. The same result was found for other parameters of interest, such as the maximum axial curvature, and in conclusion we can reasonably assume that the effect of a small (order $\Delta_{1/2}$) rounded corner is important only in the vicinity of the corner.

To investigate the behavior of D_w near the corner, we performed a set of simulations where r_c is kept constant and $N_{1/2}$ is decreased from 64 to 16 (Fig. B.2). As the grid resolution is decreased, oscillations in D_w are visible again, with an effect that is similar to the decrease in r_c in Fig. B.1. These results seem to indicate that a relatively large grid refinement ($N_{1/2} = 64$) is required to resolve the transient of detonation velocity in the vicinity of the corner when the curvature is of the order of $\Delta_{1/2}$. An even larger number of grid points is needed if r_c is further reduced.

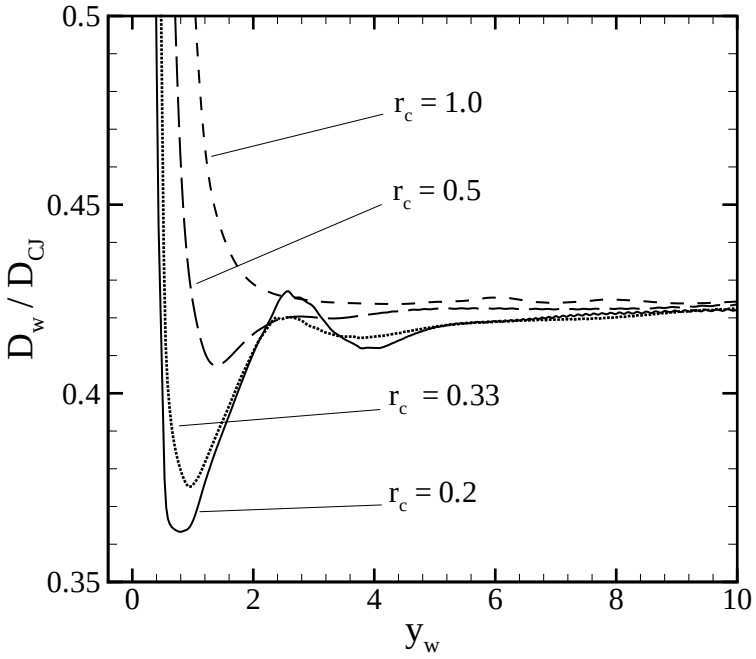

Figure B.1: Effect of a finite radius of curvature r_c on the wall detonation velocity in the vicinity of the corner.

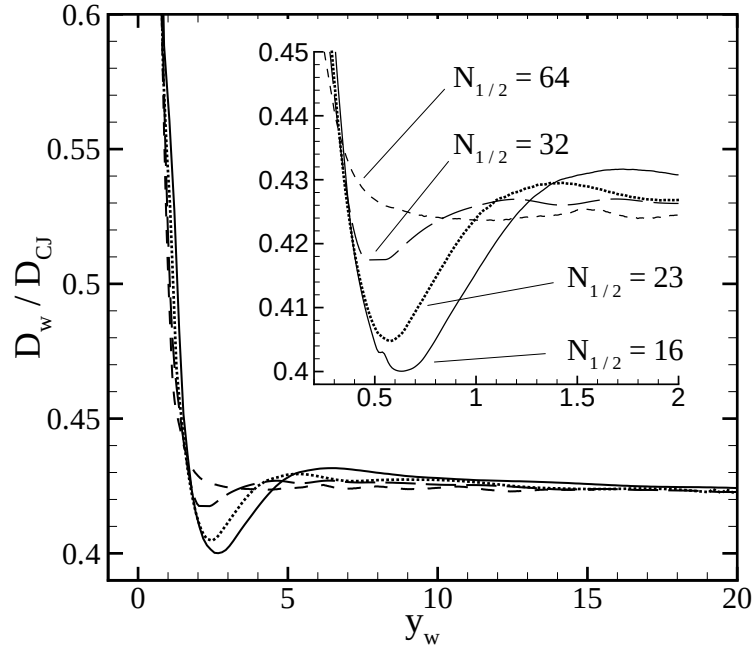

Figure B.2: Effect of grid refinement at a constant radius of curvature, $r_c = 1$. The internal box is a close up of the plot, showing the oscillations in the detonation velocity at the wall.

Appendix C

Convergence study

We perform a convergence study on the structure of the triple point observed in the case $\theta_{CJ} = 3.5$ (Fig. 4.25). The plots on the left are contours of pressure, the plots on the right are numerical schlieren images. Of the three results in Fig. C.1, the plots in (a) correspond to the higher grid resolution that was used in the current work. The number of cells in the reference half-reaction zone (the segment displayed on the left bottom of the pressure plot) is 22.5. The contours in (b) and (c) are obtained from simulations that are two and four times coarser ($N_{1/2} = 11.5$ and $N_{1/2} = 5.6$). A simulation with $N_{1/2}$ significantly greater than 22.5 has not been performed because too expensive.

As the grid resolution decreases, some details of the 0.95 reaction locus are lost, and we register lower peak values of pressure. In the schlieren image in (c), the island of partially unreacted material has disappeared, and the region behind the transmitted shock has a much simpler structure. Likewise, the small area that is above the cutoff value in the pressure contour (behind the stem connecting the first with the second triple point) is missing in (c). Also, since the time and the window of observation are the same in all the plots, the propagation of the triple-point structure appears to be slower on coarser grids than on finer grids.

One encouraging result is that only the coarsest resolution gives an answer that is qualitatively very different from the most refined (and 64 times more expensive) result. In case (b) we are even able to observe the contact discontinuity formed on the leading front, a detail that is lost in (c). Also, the distance in the triple

point positions between (a) and (b) is roughly half the distance between (b) and (c). While larger computations, possibly using Adaptive Mesh Refinement techniques, are required to draw any conclusion concerning the correct representation of this transverse wave structure, the current results seem to indicate that only minor variations in the transverse wave should be expected from simulations with resolution higher than $N_{1/2} = 22.5$.

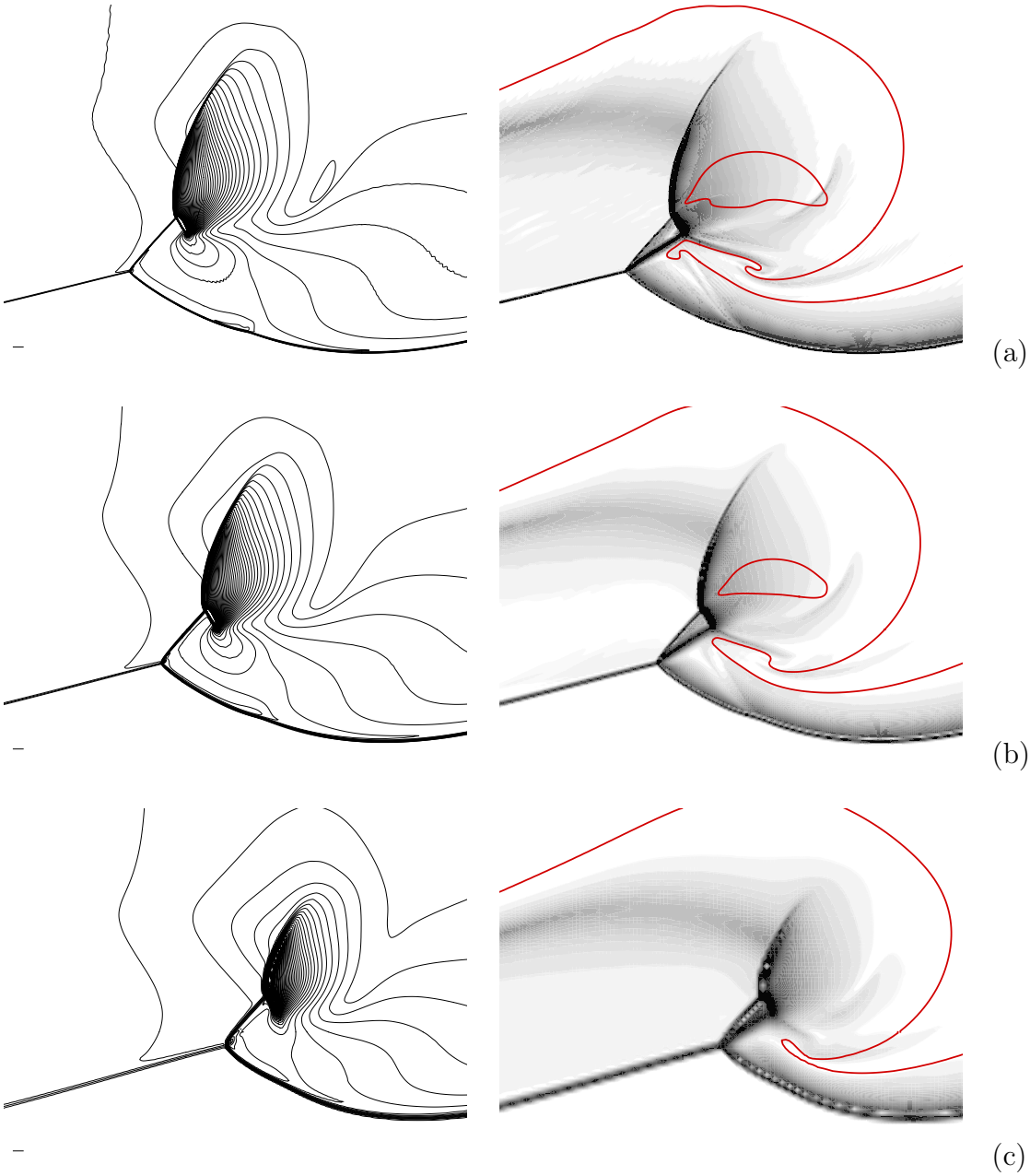

Figure C.1: Iso-contours of pressure (left), and numerical schlieren images (right) for three different grid resolutions. (a) $N_{1/2} = 22.5$; (b) $N_{1/2} = 11.2$; (c) $N_{1/2} = 5.6$.